Master's thesis

NTNU
Norwegian University of Science and Technology
Faculty of Engineering
Department of Geoscience and Petroleum

Gjermund Blauenfeldt Næss

Seismically guided CO2 storage resource estimation

A case example from the Smeaheia site in the Norwegian North Sea

Master's thesis in Petroleum Geosciences and Engineering
Supervisor: Kenneth Duffaut
April 2022

NTNU
Norwegian University of
Science and Technology

Gjermund Blauenfeldt Næss

Seismically guided CO2 storage resource estimation

A case example from the Smeaheia site in the Norwegian North Sea

Master's thesis in Petroleum Geosciences and Engineering
Supervisor: Kenneth Duffaut
April 2022

Norwegian University of Science and Technology
Faculty of Engineering
Department of Geoscience and Petroleum

Abstract

As CO_2 in the atmosphere reaches greater records, the international community calls for an urgent curbing of emissions, and carbon capture and storage (CCS) is an important contributor to this herculean effort. In order to meet the CO_2 emissions targets that are modelled in a 1.5°C or 2°C pathway, we must drastically scale up CCS technologies today. However, it is still an emerging industry, lacking in standards and well established operating procedures.

In this thesis we demonstrate our contribution of seismically derived petrophysical properties to improve CO_2 storage capacity and injection estimates of geological CO_2 storage formations and prospects. Our contribution is a traffic-light visualization, and ranking system for suitable CO_2 storage and injectivity locations. We employ a post-stack model-based seismic inversion process, generating reservoir property subresults, such as porosity and permeability volume maps. These are further processed into a CO_2 injectivity map, and CO_2 injectivity estimates, where green is best, and red is worst potential, according to our traffic-light model. In addition CO_2 storage capacity is estimated.

We employ our model on the Smeaheia CO_2 storage, focusing on the alpha and beta prospects, as well as the Sognefjord, Fensfjord, and Krossfjord formations. Of the mid-case prospects evaluated, the beta prospect scores the best results with CO_2 storage resource estimations of 37%, 4246.46mD and 247.93Dm, for the porosity, permeability and kh-estimate, respectively. The CO_2 storage capacity was estimated to be 58.11Mt. For the studied mid-case formations, Sognefjord Fm results showed a CO_2 storage resource estimations of 24%, 658.37mD and 37.90Dm, for the porosity, permeability and kh-estimate, respectively. We demonstrate the utility of the traffic-light injectivity map in determining the optimal injectivity site. Based on the results, our method demonstrates the ability to accurately align with previously established results, in addition to adhering to our outlined traffic-light model.

Sammendrag

Ettersom CO_2 i atmosfæren når nye rekorder, krever det internasjonale samfunnet en betydelig reduksjon av utslippsgasser. Karbonfangst og -lagring (CCS) er en viktig bidragsyter i denne innsatsen. For å oppfylle målet om en maksimal temperaturstigning på mellom 1,5°C og 2°C, er vi avhengig av å oppskalere CCS og CO_2 lagring drastisk. CCS er imidlertid en næring i vekst som mangler standarder og veletablerte driftsprosedyrer.

Denne oppgaven viser et bidrag av seismisk avledede petrofysiske egenskaper som benyttes til å forbedre CO_2-lagringskapasitet og injeksjonsestimater for geologiske CO_2-lagringsformasjoner og prospekter. Kjernen i bidraget er en trafikklysvisualisering og et rangeringssystem for egnede CO_2-lagrings- og injeksjonslokasjoner. Vi benytter en post-stack seismisk inversjonsprosess til å generere reservoaregenskaper og delresultater, som porøsitet- og permeabilitetsvolumkart. Disse ble bearbeidet til et CO_2-injeksjonskart og CO_2-injeksjonsestimater, hvor grønt er best, og rødt har dårligst potensial, ifølge vår trafikklysmodell. I tillegg er CO_2-lagringskapasiteten beregnet.

Vi bruker modellen vår på Smeaheiaområdet, med fokus på alpha- og beta-prospektene, samt Sognefjord-, Fensfjord- og Krossfjordformasjonene. Av de evaluerte mid-case-prospektene scorer beta-prospektet de beste resultatene med CO_2-lagringsegenskaper på 37%, 4246.46mD og 247.93Dm, for henholdsvis porøsitet, permeabilitet og kh-estimat. CO_2-lagringskapasiteten ble estimert til å være 58.11Mt. For mid-case formasjonene viste Sognefjord Fm en CO_2-lagringsressursestimat på 24%, 658.37mD og 37.90Dm, for henholdsvis porøsitet, permeabilitet og kh-estimat. Vi demonstrerer nytten av trafikklysinjeksjonskartet for å kunne bestemme optimale injeksjonslokasjoner. Basert på resultatene viser metoden evnen til å kunne justere tidligere etablerte resultater, i tillegg til å følge vår skisserte trafikklysmodell til å bedre bestemme CO_2-lagringsegenskaper.

Preface

This Master's Thesis concludes the studies for the MSc degree in Petroleum Geoscience at the Department of Geoscience and Petroleum at the Norwegian University of Science and Technology (NTNU) in Trondheim. The thesis has been developed in fall/spring 2021/2022, while working as an CCS-intern in Maersk Drilling in Copenhagen. Through my thesis and CCS-internship in Maersk Drilling, my passion for CCS and its potential has increased even more.

Acknowledgements

I would first of all acknowledge my supervisor, Kenneth Duffaut, for guiding me through this Master's Thesis, always being available and wanting only the best for me, throughout this process. Kenneth has stood up for me, even in the most hectic weeks, and I feel extremely lucky to have had the opportunity to learn and work with Kenneth. NTNU is extremely lucky, having Kenneth Duffaut, as being so passionate about his work, but also the people around him.

Furthermore, completion of this master thesis would not have been possible without my brother in law, Jama. Thank you for all the genius logistical solutions for making this Master's Thesis possible, the support in the ending hours, and being my closest "classmate" the last months.

An enormous gratitude goes out to my girlfriend, Elise, for always supporting me with the love I needed in the ups and down of this thesis work and for being patient with me to finish this thesis. I have to thank my family, my sister Kjersti, for always being there and helping me throughout when I needed it the most.

Lastly an acknowledgement to the team at *CO2 DataShare* is important, for the possibility of using the SMEAHEIA dataset, publicly sharing important CO_2 storage datasets that help scale-up the CO_2 storage industry. I would like to thank NTNU for accepting to let me write my thesis from Copenhagen while having a student job and giving me access to the software products Petrel, and Hampson-Russell's Geoview.

Contents

Figures

Tables

Nomenclature

Abbreviations

CCS Carbon capture and storage

$CCUS$ Carbon capture, utilization and storage

$CO2-EOR$ Carbon Dioxide Enhanced Oil Recovery

$CO2$ Carbon Dioxide

Fm Formation

Gp Group

$impedance-porosity$ Acoustic impedance - porosity

MD Total Measured Depth

$mid-case$ Middle case

mid Middle

NCS Norwegian Continental Shelf

NE North-East

$no.$ Number

OWT One-way Time

pdf Probability density function

$poro-perm$ Porosity-permeability

QC Quality control

RKB Rotary Kelly Bushing

SDL Suggested Drilling Location

SE South-East

SW South-West

TRL Technology readiness level

TVD Total Vertical Depth

TWT Two-way time

VSP Vertical Seismic Profile

Symbols

ϕ_e Effective porosity

ϕ_t Total porosity

A_r Displacement amplitude

c Speed of light in a vacuum

Dm Darcy-meter

GR Gamma ray

Gt Gigatonne

h Reservoir thickness [m]

I Acoustic Impedance

k Permeability [mD]

k_{Hor} Horizontal permeability [mD]

k_{Ver} Vertical permeability [mD]

kh kh-estimate [Dm]

m/s meter per secoond

mD Milli Darcy

Mt Megatonne

$Mtpa$ Milliontonne per annum

N/G	Net to gross ratio
P	Pressure
R	Reflection coefficient
T	Temperature

Chapter 1

Introduction

The IPCC Sixth Assessment Report, Working Group 2, *Climate Change 2022: Impacts, Adaptation and Vulnerability* (IPCC 2022a, pp. SPM-35) states:

"The cumulative scientific evidence is unequivocal: Climate change is a threat to human well-being and planetary health. Any further delay in concerted anticipatory global action on adaptation and mitigation will miss a brief and rapidly closing window of opportunity to secure a liveable and sustainable future for all. (very high confidence) "

There is an urgent need to scale up technologies to fight climate change. Carbon Capture and Storage (CCS) is pointed out as one of the main pillar technologies to help cut the emissions of CO_2 in the atmosphere and reach net-zero emissions by 2050 — thus reaching the Paris Agreement goals (UN 2015) to remain a sustainable future on our Earth (IPCC 2005; IEA 2021; IPCC 2022b). Estimates and analysis suggest a need for capturing and storing 7-15 Gt CO_2 per year in 2050 (IPCC 2018; IEA 2021). Today, the rate is at around 40 Mtpa. CCS is an emerging industry, and if all projects in planning reach an operative state by 2030, the number can reach 267 Mtpa in 2030 (GCCSI 2022). This number is, however, still far behind the estimates for the need of CCS (IPCC 2018; IEA 2021). This tells how urgent it is to scale-up CCS technologies today, tomorrow, and further towards 2050.

Geoscientists are central in the CCS industry, as CO_2 storage (Holt et al. 1995) is the end stage of the CCS value-chain (IPCC 2005). There is a high need for compatible CO_2 storage projects that can inject sufficient volumes of CO_2, and store the CO_2 in the most efficient way with regards to cost and implementation. Now, as more and more CO_2 storage projects are being planned, it will be important to have common workflows from the point where one sits with the data, f.ex seismic, to the injection of the CO_2.

Even though CCS is currently regarded as a mature technology (GCCSI 2021b), the CCS value-chain is still in its infancy — it is prohibitively expensive, struggling with lack of public acceptance, and there are still no clear standards in the value-chain. All of these reasons make it difficult for stakeholders, relevant for CO_2 storage and the CCS value-chain, to utilize CCS as a climate and commercial tool. Putting this into a geoscience perspective, how do we use all the experience and scientific knowledge in the oil and gas and CO_2 storage community to make clear guidelines and workflows to make CO_2 storage "easy" to use and cost-effective?

To scale up CCS it is important to develop methods and workflows for the industry that can be quickly applicable, based on robust approaches. Geoscientists are first of all central in most of the stages in planning and operating a CO_2 storage project. First, crucial work from geoscientists in choosing the right reservoir and prospect for storage is needed. Secondly, while operating and after closure of a storage project, accurate monitoring of the injected CO_2 is needed (Lumley 2019; Ringrose 2020).

A contribution from geoscientists to help accelerate the commercialization of the CO_2 storage industry — and to meet the sufficient CO_2 injection rates needed to help reach the climate goals — can be to use well-known geophysical workflows and scientific established methods to evaluate and plan CO_2 storage prospects.

Two key elements in characterizing a CO_2 storage site are by understanding CO_2 storage capacity and injectivity. Porosity and permeability are central reservoir properties in these calculations (Halland et al. 2014). By evaluating these elements accurately, a stakeholder interested in using CCS as a CO_2-reduction tool is many steps closer towards realizing a CO_2 storage project.

1.1 Scope of the master thesis

This master thesis uses the Smeaheia aquifer CO_2 storage area as a case study to perform a seismic quantitative process to estimate CO_2 storage capacity and injectivity and tries to implement a "traffic-light" cut-off approach to evaluate the studied prospects and formations. This is done through a post-stack seismic inversion process in combination with seismic mapping and well data handling.

The scope of this master thesis is first to calculate the CO_2 storage capacity and CO_2 injectivity — in terms of the kh-estimate — of the Smeaheia CO_2 storage reservoir formations and prospects, based on porosity and permeability volumes and calculations generated from a model-based post-stack seismic inversion. The traffic-light approach is further implemented, based on reasonable cut-off criterias for porosity, permeability and injectivity, as a way of evaluating CO_2 storage formations.

1.2 Previous published knowledge and methods

Methods to characterize CO_2 storage site resources are first of all building on vast experience and applicable methods from the oil and gas industry (Holt et al. 1995; Ringrose 2020). However, most of the state-of-the-art utilization of seismic and geological data for CO_2 projects are based on data from completed and operating CO_2 storage projects (Lumley 2010; Eiken et al. 2011).

Engelenburg and Blok (1991) and Van der Meer (1992) investigated early CO_2 storage capacity potential in aquifers. Holt et al. (1995) did further reservoir simulations and investigated how CO_2 storage capacity depends on injection rate.

The Sleipner CO_2 storage project came in operation in 1996 (Baklid et al. 1996) and has since then been a corner stone project for studying and understanding the behaviour of injected CO_2 in saline aquifers based on geophysical data (Eiken et al. 2011). Lindeberg (1997) studied the distribution of injected CO_2 in saline aquifers, using Utsira as a close model. Further studying the permeability and vertical flow of CO_2 injection gave more understanding how these physical factors are decisive for CO_2 storage capacity. Zweigel et al. (2000), Arts et al. (2000), Eiken et al. (2000), and Lindeberg et al. (2001) further proved the ability of utilizing time-lapse seismic data for monitoring the injected and stored CO_2 in the Sleipner project. Chadwick et al. (2010) executed a quantitative method of using the seismic 4D data and Dupuy et al. (2017) tried to characterize the injected CO_2 in the Utsira formation in a seismic quantitatively way.

Methods to derive accurate estimations of CO_2 storage resources, the CO_2 storage capacity and injectivity, have been understood more accurately through the years, building upon the CO_2 storage projects in operation. Bachu et al. (2007), GHG (2009), Vangkilde-Pedersen et al. (2009), Brennan et al. (2010), Gammer et al. (2011), Goodman et al. (2011), Halland et al. (2011) and Halland et al. (2014), Goodman et al. (2016), Ringrose (2020) and Hjelm et al. (2020) are some of the suggested strategies for estimating CO_2 storage capacity. Ways of understanding CO_2 injectivity has further been studied by Mishra et al. (2013), Miri and Hellevang (2018), Statoil (2016), Ringrose (2020), Valle et al. (2020) and Valluri et al. (2021).

To help accelerate the commercialization of CO_2 resources, several countries have developed CO_2 storage atlases and suggest workflows to characterize CO_2 storage sites. US (Goodman et al. 2011; Goodman et al. 2016) Norway (Halland et al. 2011; Halland et al. 2014) and UK (Bentham et al. 2014) have been front-runners here. Also countries like Australia, Mexico and Brazil have published CO_2 storage atlases (Ciotta et al. 2020).

Workflows to characterize and rank CO_2 storage sites have further emerged, as this is highly needed to scale up CCS and thus CO_2 storage. Bachu (2003) suggested

a way of screening and ranking sedimentary basins. Since then Chadwick et al. (2008), Goodman et al. (2011), Halland et al. (2014), K. Anthonsen et al. (2014), Bentham et al. (2014) and Halland and Riis (2018) have suggested strategies to characterize CO_2 storage sites.

As of today, utilizing seismic data quantitative to monitor the injected CO_2 in saline aquifers have been thoroughly studied. However, following on the characterization and ranking approach, seismic quantitative methods can be effective tools. Lloyd et al. (2021) suggests an elegant workflow for mapping and ranking CO_2 storage prospects within regional saline aquifers based on seismic data and full waveform inverted data. Fawad et al. (2021) characterizes the Smeaheia CO_2 storage area based on seismic inversion, defining porosity, permeability and shale volume. This master thesis will demonstrate the exploitation and strength of seismic through post-stack inversion to derive quantitative estimates for the calculations of CO_2 storage and injectivity, and thus characterize the Smeaheia CO_2 storage site.

The Smeaheia CO_2 storage area has been thoroughly studied, being one of the main candidate CO_2 storage areas for large-scale CO_2 storage on the Norwegian continental shelf. In addition to the already mentioned Fawad et al. (2021) paper, Bøe et al. (2002), Christensen and Holloway (2003), the Norwegian CO_2 storage atlas (Halland et al. 2011);(Halland et al. 2014), Gassnova in 2012 (Ross et al. 2013), Sundal et al. (2014) and by Statoil in 2016 (Statoil 2016) are some of the resources investigating the Smeaheia CO_2 storage area.

1.3 Structure of the master thesis

This study entails of the following chapters:

Chapter 1 introduces the background, scope of the master thesis and elaborates on the state-of-the-art of previous published knowledge on how seismic can contribute in CO_2 storage resource estimations.

Chapter 2 presents the background for CCS and CO_2 storage.

Chapter 3 presents the equations and theoretical framework applied in this study. The CO_2 storage capacity and injectivity equations are central, and the theory behind the seismic inversion to establish the porosity and permeability volumes is described.

Chapter 4 further elaborates on the methodology applied and explains the steps from the seismic and well data, through the process of executing the seismic inversion to derive an acoustic impedance volume and further porosity and permeability volumes. This builds the basis for evaluating the Smeaheia CO_2 storage site quantitative, based on CO_2 storage capacity and injectivity. In addition a traffic-

light approach is explained to characterize the evaluated CO_2 storage formations further.

Chapter 5 establishes the main results of this study, generated from the methodology and theory applied. Additionally, sub-results are being presented, thus these are in different ways decisive for for the main results.

Chapter 6 elaborates and discusses the results of the thesis. In addition, the biggest uncertainties of the findings and how the seismic-guided approach in this study can be applied in the CO_2 storage industry are discussed.

Chapter 7 concludes the findings and the explorations done in the master thesis. This is followed by implications and recommendations for further research and work to strengthen the seismic quantitative approach for estimating CO_2 storage resources.

Chapter 8 suggest further steps and work to be done to improve this study's workflow and approach.

Chapter 2

Background

2.1 Carbon Capture and Storage - CCS

Carbon capture and storage, CCS, is the technology of capturing carbon dioxide (CO_2) from industry and power sectors, transporting it in pipelines, trucks or ships and storing it permanently deep underground in the subsurface (IPCC 2005). The phrase CCUS is often also use to include the utilization step of the value-chain. Figure 2.1 illustrates the value-chain well. CCS captures and stores CO_2 from point sources and directly from the air, preventing it from releasing into the atmosphere. The four main ways CCS can contribute in the transition to net-zero CO_2 emissions (IEA 2021; GCCSI 2020; GCCSI 2021a) are:

1. Cut emissions from existing assets and provide low carbon power.
2. Achieve deep decarbonisation in hard-to-abate industries like cement, steel, chemicals and waste-to-energy.
3. Enable the production of low-carbon hydrogen at scale.
4. Provide technology-based CO_2 removal and negative emissions through BECCS (bio-energy with CCS) and DACCS (direct air capture with CCS)

CO_2 can further be stored in underground reservoirs in saline aquifers and depleted oil and gas fields. More unconventional CO_2 storage options are storage in basalt and ultramafic rocks like peridotite and in coal seams GCCSI (2021b). CO_2 can also be stored through CO_2-EOR and Enhanced Coal Bed Methane (ECBM) production, but additional monitoring and life-cycle analysis have to be done if these methods are to be used as dedicated CO_2 storage GCCSI (2021b). The 50 years experience from CO_2 injection and monitoring from the CO_2-EOR industry and from the Sleipner project Eiken et al. (2011) have been crucial to develop the technology readiness level (TRL) of CO_2 storage in saline aquifers and depleted oil and gas fields GCCSI (2021b).

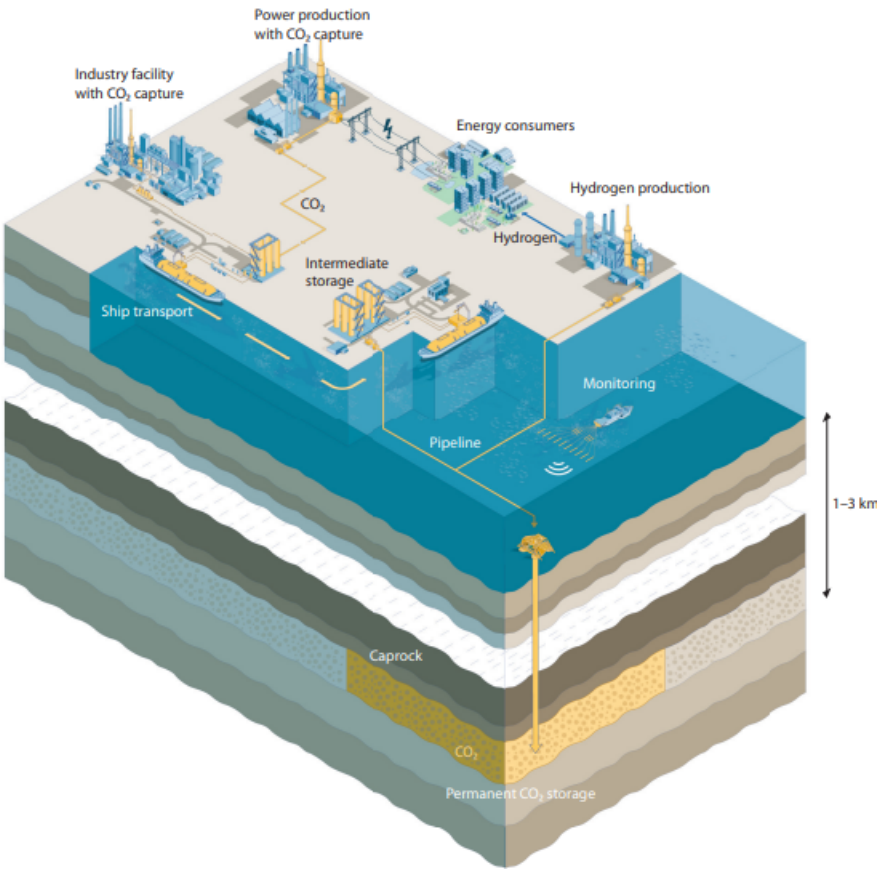

Figure 2.1: Figure illustrating the CCS value-chain from capture, transport and storage of the CO_2. Figure is taken from Gassnova in the Longship White Paper report to the Storting Petroleum and Energy (2020).

2.2 CO2 storage in saline aquifers

The 50 years experience from CO_2 injection and monitoring from the CO_2-EOR industry and from the Sleipner project Eiken et al. (2011) have been crucial to develop the high technology readiness level (TRL) of CO_2 storage in saline aquifers GCCSI (2021b). Here, a total of $20Mt$ of CO_2 has been stored to date and big leaps in dedicated CO_2 storage, injection and monitoring techniques have been developed. The Snøhvit CCS project in the Barents Sea in Norway from 2008 and the In Salah project in Algeria from 2004-2011 are in addition central projects even more confirming that CO_2 can be injected at a Mt-scale rate, CO_2 can be safely monitored and be stored permanently (GCCSI 2021b).

Saline aquifers often lie in the same sedimentary basins as the producing hydrocarbon fields. They have much of the same physical properties, as the porosity and permeability are key parameters to have in place for CO_2 storage in saline aquifers Halland et al. (2014). In addition, as in a hydrocarbon play system, impermeable

layers above the CO_2 storage prospects are needed, as a seal, to be sure that the injected CO_2 will not leak. Three important CO_2 storage resources to have in place for a sufficient storage project are (Ringrose 2020):

- containment: the ability of a CO_2 storage site to securely contain the injected CO_2 with regards to sealing capacity, fault structures and migrate routes.
- capacity: the ability of the storage site to store the amount of planned CO_2 supply. Porosity values and distribution is important to meet these requirements.
- injectivity: the characteristic of the CO_2 storage formation or site to be able to inject the planned CO_2 stored with regards to flow capabilities, rate and pressure regimes. Permeability is amongst the key parameters here.

In this thesis the focus is on estimating CO_2 storage resources based on CO_2 storage capacity and injectivity. The reservoir properties porosity and permeability forms the basis for understanding these terms.

Chapter 3

Theory

This chapter forms the set of equations and theory applied in the steps done in the methodology (chap. 4). The geophysical framework is presented building the basement for this master thesis, going through theory about seismic waves, rock physics, CO_2 storage capacity and injectivity, in-situ conditions and petrophysical properties.

3.1 Seismic waves

Seismic waves can act as elastic waves and the applied force in an isotropic, elastic media penetrating through the earths' layers. Seismic waves measure the elasticity and the compressibility of a rock system and information about difference in reflection between subsurface rock layers and travel time are amongst the information possible to retrieve (Hampson and Russell 1999; Z. Wang 2001; Lumley 2019).

Seismic velocity

The elastic moduli forms the basis of defining seismic velocities. Seismic waves can be measured by the velocities P-wave velocity, V_P, and S-wave velocity, V_S (Mavko et al. 2020):

$$V_P = \sqrt{\frac{K + \frac{4}{3}\mu}{\rho}}, \tag{3.1}$$

$$V_S = \sqrt{\frac{\mu}{\rho}}, \tag{3.2}$$

where:
K = bulk modulus

μ = shear modulus
ρ = density.
V_P and V_S can also be written in relationship with Poisson's ration, ν ν (Mavko et al. 2020):

$$\frac{V_P^2}{V_S^2} = \frac{2(1-\nu)}{1-2\nu} \tag{3.3}$$

Acoustic impedance

The **acoustic impedance** is central in describing the penetrating seismic wave, as it travels through rocks and fluid in the subsurface. Acoustic impedance, I, is defined by the density, ρ, and the velocity, V, (Mavko et al. 2020; Richards and Aki 1980; Hampson and Russell 1999):

$$I = \rho V. \tag{3.4}$$

Subscripting P-wave velocity as V_P and S-wave velocity as V_S, the seismic P- and S-impedances can be written as (Mavko et al. 2020):

$$I_P = \rho V_P, \tag{3.5}$$

$$I_S = \rho V_S. \tag{3.6}$$

As the seismic waves penetrates through different rock layers, natural variability in the acoustic impedance can be measured. The difference in the acoustic impedance between two rock layers generates a seismic reflection. The **reflection coefficient**, R, describes this, giving a relationship between the displacement amplitude and incident wave amplitude, A_r and A_i, respectively. Assuming two isotropic, elastic and homogeneous layers separated between a plane interface, the normal incidence reflection coefficient can be defined as (Mavko et al. 2020; Hampson and Russell 1999; Lindseth 1979):

$$R = \frac{\rho_2 V_2 - \rho_1 V_1}{\rho_2 V_2 + \rho_1 V_1} = \frac{A_r}{A_i}, \tag{3.7}$$

where ρ_1 and V_1 is density and velocity of layer 1, respectively, and ρ_2 and V_2 is the density and velocity of layer 2, respectively.

Following with the reflection coefficient, the **convolutional model** of a seismic trace, the synthetic S_t, can further be expressed by the the wavelet, $w(t)$, and the noise measurement, $n(t)$, as (Hampson and Russell 1999; Liner 1999):

$$S_t = R_t * w_t + n_t, \tag{3.8}$$

where $*$ depicts the convolution. If density and sonic logs are available and a wavelet is applied, **synthetic seismograms** can be made, based on eq. 3.8.

3.2 Rock physics

Rock physics is a central toolbox to relate seismic data with reservoir properties and characteristics. Properties of the rock and fluid systems subsurface such as porosity, permeability, lithology, saturation and pore fluids, can be described more thorough with linking rock physics and seismic data (Z. Wang 2001).

3.2.1 Elastic moduli: bulk and shear modulus

Assuming isotropic and linear elastic media, the media returns to its former state after some applied force has deformed the media (Lumley 2019). Within these assumptions, Hooke's law defines the stress and strain relationship in the following way (Mavko et al. 2020; Timoshenko and Goodier 1934):

$$\sigma_{ij} = \lambda\delta_{ij}\varepsilon_{\alpha\alpha} + 2\mu\varepsilon_{ij}, \tag{3.9}$$

$$\varepsilon_{ij} = \frac{1}{E}[(1+\nu)\sigma_{ij} - \nu\delta_{ij}\sigma_{\alpha\alpha}] \tag{3.10}$$

where the strain tensor elements are expressed by ε_{ij} and stress tensor elements by σ_{ij}. We further have that:
λ=Lamé's constant,
μ=shear modulus,
ν=Poisson's ratio,
δ_{ij}=0 if $i \neq j$,
δ_{ij}=1 if $i = j$,
$\varepsilon_{\alpha\alpha}$=volumetric strain,
$\sigma_{\alpha\alpha}$=mean stress.

This further builds the definition of the bulk modulus, K. The bulk modulus can be expressed as (Mavko et al. 2020):

$$\sigma_0 = \frac{1}{3}\sigma_{\alpha\alpha} = K\varepsilon_{\alpha\alpha} \tag{3.11}$$

where σ_0 is the hydrostatic stress. And we reach the expression for compressibility, β:

$$\beta = \frac{1}{K}. \tag{3.12}$$

Compressibility describes the elastic stiffness of a fluid or solid (Lumley, 2019).

The elements of the strain and stress tensors further defines the shear modulus, μ (Rock physics handbook):

$$\sigma_{ij} = 2\mu\varepsilon_{ij}, i \neq j \tag{3.13}$$

Batzle and Z. Wang (1992) defines density in terms of molecular weight and molar volume:

$$\rho = \frac{M}{V} \tag{3.14}$$

where
M=molecular weight
V=molar volume.

3.2.2 Rock physics models

Greenberg and Castagna's V_S relation

Estimations of shear wave, V_S is often needed and different models exists relating V_P (Mavko et al. 2020). Greenberg and Castagna (1992) suggest relating V_S with V_P in the following way (Mavko et al. 2020; Greenberg and Castagna 1992):

$$V_S = \frac{1}{2}((\sum_{i=1}^{L} X_i \sum_{j=0}^{N_i} a_{ij} V_P^j) + (\sum_{i=1}^{L} X_i (\sum_{j=0}^{N_i} a_{ij} V_P^j)^{-1})^{-1}), \sum_{i=1}^{L} X_i = 1, \tag{3.15}$$

where:
X_i = fraction of the lithological constituents of the rock
L = no. of monomineralic lithological constituents
N_i = order of the polynomial for constituent i
a_{ij} = regression coefficients, listed for shale and sandstone in table 3.1. The Greenberg and Castagna (1992) relation calculates shear wave in brine-saturated rock systems, from P-wave, V_P.

Lithology	a_{i1}	a_{i0}
Sandstone	0.80416	-0.85588
Shale	0.76969	-0.86735

Table 3.1: Regression coefficients for shale and sandstone in pure lithologies, used in Greenberg and Castagna (1992). Table modified from Mavko et al. (2020).

Gassman's relation

When a seismic wave penetrates through the earths' subsurface, the Gassmann relation is one of the most important equations describing the increase in effective bulk modulus, K_{sat} (Mavko et al. 2020). An important assumption for the Gassman relation is that it only yields at low frequencies. The Gassmmann equation is often used for the fluid substitution and can be described as (Mavko et al. 2020; Gassmann 1951; Biot 1956):

$$\frac{K_{sat}}{K_0 - Ksat} = \frac{K_{dry}}{K_0 - K_{dry}} + \frac{K_{fl}}{\phi(K_0 - K_{fl})}, \mu_{sat} = \mu_{dry}. \tag{3.16}$$

We have that:
ϕ = porosity,

μ_{dry} = effective shear modulus of a dry rock,
mu_{sat} = effective shear modulus of a rock with pore fluid,
K_{dry} = effective bulk modulus of a dry rock,
K_{sat} = effective bulk modulus of a rock with pore fluid,
K_0 = bulk modulus of the mineral making up the rock,
K_{fl} = effective bulk modulus of the pore fluid.

As the Gassmann relation help describe the bulk modulus when fluid mix in the rock systems changes, the Gassmann equation can be applied twice two describe the change that is happening (Mavko et al. 2020):

$$\frac{K_{sat-1}}{K_0 - K_{sat-1}} - \frac{K_{fl-1}}{\phi(K_0 - K_{fl-1})} = \frac{K_{sat-2}}{K_0 - K_{sat-2}} - \frac{K_{fl-2}}{\phi(K_0 - K_{fl-2})}, \tag{3.17}$$

where the K_{fl-1}, K_{fl-2} and K_{fl-1}, K_{fl-2} describes the two different states of the fluid mix after the fluid substitution has happened, for the fluid bulk modulus and rock saturated bulk modulus.

3.3 Seismic inversion

A seismic inversion process is an attempt to estimate the reflection coefficient (eq. 3.7), and thus the acoustic or elastic impedance, density or velocity, from the seismic traces and hence the convolutional model (eq. 3.8) (Hampson and Russell 1999; Veeken et al. 2004). Seismic inversion can be divided into two types; deterministic inversion and stochastic inversion (Veeken et al. 2004; Simm and Bacon 2014). Further approaches of the seismic inversion is either done pre-stack or post-stack (Veeken et al. 2004). Russell and Hampson (1991) summarized the different seismic inversion approaches:

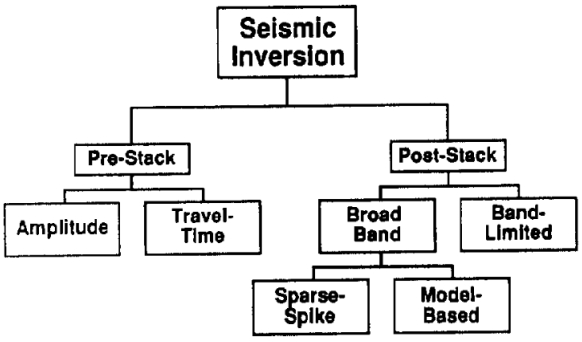

Figure 3.1: An overview of the different seismic inversion approaches summarized by Russell and Hampson (1991). Figure courtesy of Russell and Hampson (1991).

3.3.1 Post-stack inversion

Post-stack seismic inversion attempts to generate I, acoustic impedance, estimations from the seismic traces penetrating through the subsurface (Russell and Hampson 1991). From the beginning, the assumption is that the seismic traces are represented and modelled by the convolutional model, eq. 3.8. The post-stack inversion process deconvolves the wavelet, w_t. There are two steps involved in the **deconvolution** of the wavelet (Hampson and Russell 1999):

- The wavelet is found.
- With applying the inverse, the wavelet is removed.

With further removing the noise, n_t, an expression for the acoustic impedance can be retrieved (Russell and Hampson 1991):

$$I_{t+1} = I_t(\frac{1+R_t}{1-R_t}) \tag{3.18}$$

3.3.2 Wavelet

Hampson and Russell (1999) Geoview software has two ways of extracting wavelets. Geoview's statistical wavelet extraction method based on the STRATA model building utilizes only the seismic traces for the wavelet extraction and the phase spectrum is not calculated (Hampson and Russell 1999). This has to be set by the user. The other method of extracting a wavelet in STRATA is from utilizing information from a well log. It is possible to only use the well for phase decision and full amplitude spectrum (Hampson and Russell 1999). It also possible to combine information from the well to decide an exact phase constant and further decide the amplitude spectrum from the statistical wavelet extraction process from the seismic data.

3.3.3 Model-based inversion

Model-based inversion is a deterministic broadband inversion process. The starting point in a model-based inversion is an initial geologic model with constraints. Then an iteration process with this initial model is done to create synthetic seismograms as close as the original seismic data. The process is well visualized in fig. 3.2 by Veeken et al. (2004):

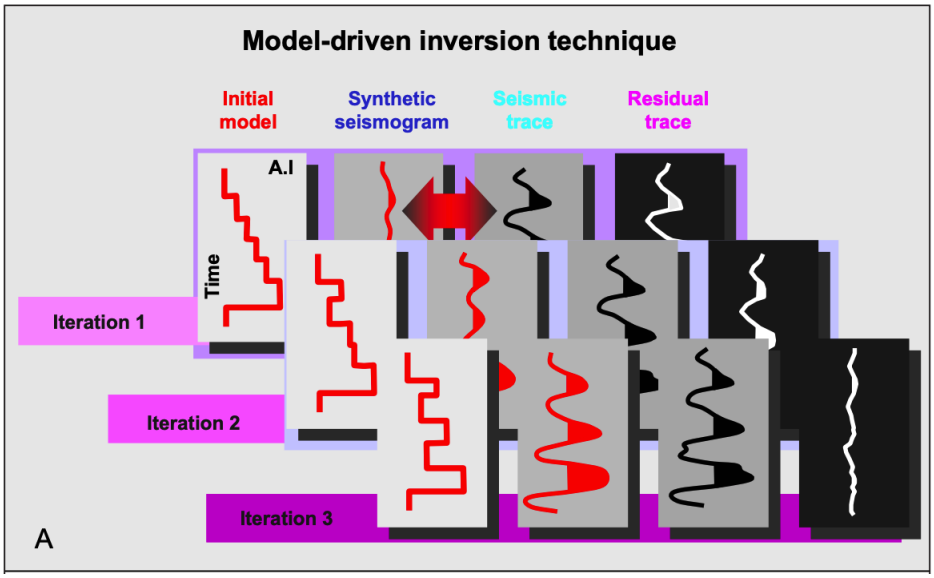

Figure 3.2: The process of the model-base seismic inversion. Figure courtesy of Veeken et al. (2004)

3.4 Permeability

Permeability, κ, can be expressed in terms of Darcy's equation. Darcy's law states (Mavko et al. 2020):

$$Q = -\kappa \frac{A}{\eta} \frac{\Delta P}{L}, \tag{3.19}$$

where:
A = cross-sectional area,
P = pressure,
η = dynamic viscosity.

Kozeny-Carman equation is one of the most popular methods to relate porosity with permeability. The Kozeny-Carman relation can be expressed as (Carman 1961; Mavko et al. 2020):

$$\kappa = B \frac{\phi^3}{S^2 \tau^2}. \tag{3.20}$$

We have that:
B = geometric factor accounting for the irregularities of pore shapes,
ϕ = porosity,
S = specific surface area,
τ = tortuosity.

3.5 CO_2 storage capacity

The first key element in describing a CO_2 storage reservoir is the CO_2 storage capacity. CO_2 storage capacity can be defined in different ways. Bachu et al. (2007) defined in four different ways: theoretical, effective, practical and matched capacity. Theoretical capacity, V_{CO_2} can be defined as (Ringrose 2020):

$$V_{CO_2} = V_{trap}\phi(1-S_{wirr}), \tag{3.21}$$

where V_{trap} is the volume of the trap, ϕ is the porosity and S_{wirr} is the irreducible water saturation, so $(1-S_{wirr})$ is an expression of max CO_2 saturation at pore-scale.

Equation 3.21 describes the estimated CO_2 storage capacity in terms of the theoretical available volume. Thus it does not count for fluid effects when the CO_2 flows into the reservoir. Bachu (2015) suggested an effective storage capacity expression and taking into consideration the maximum saturation of CO_2, (1-S_{wirr}) we get the expression for effective storage capacity (Ringrose 2020):

$$M_{CO_2} = V_b\phi N/G\rho_{CO_2}\varepsilon(1-S_{wirr}). \tag{3.22}$$

V_b is the bulk rock volume, N/G is the net to gross ratio and ε is the storage efficiency factor. Practical CO_2 storage capacity would be the next step, including regulatory and economic factors into the estimation. In the end, when a specific storage site is chosen and linked to a CO_2 storage project, the matched capacity can be estimated.

3.6 CO_2 injectivity

The second key element to further describe a CO_2 storage reservoir is the CO_2 injectivity. An often used expression is the permeability*thickness product. It is differently referred as either the *kh*-estimate, *kh* or the *k*-*h*product (Halland et al. 2011; Miri and Hellevang 2018; Statoil 2016; Ringrose 2020; Valluri et al. 2021). In this thesis we study the CO_2 injectivity in terms of the *kh*-estimate, which we define as:

$$kh-estimate = k*h*N/G, \tag{3.23}$$

where *k* is the permeability of the reservoir, *h* is the reservoir thickness and taking into consideration the N/G, the net reservoir (Statoil 2016).

However, CO_2 injectivity can also be defined by the CO_2 injectivity index, II_{CO_2} (Ringrose 2020; Miri and Hellevang 2018; Valluri et al. 2021):

$$II_{CO_2} = \frac{q_g}{(p_{wi}-p_{res})} = \frac{1.406kh_i(p/\mu_g Z)}{T[ln(r_e/r_w)-0.75]}, \tag{3.24}$$

where high flow rates are assumed.
q_g = flow rate

p_{res} = reservoir formation pressure p_{wi} = bottom-hole pressure/pressure at the well injection
h_i = height of injection well interval
$p/\mu_g Z$ = pressure depth function
T = temperature
r_e = effective radius of the reservoir unit
r_w = radius of the well.

3.7 Thermodynamic conditions in saline aquifers

Thermodynamic conditions like pressure and temperature define how the CO_2 behaves deep underground in the subsurface. With knowing the pressure and temperature regimes, the CO_2 density can be found and the state of whether it is in a gaseous, liquid or supercritical state. When storing CO_2 deep underground in saline aquifers, the preferable state of the CO_2 is to be in a supercritical state, because it is 500 times denser than it is in a gaseous state at the surface (Lumley 2019).

Pressure is a key parameter for the thermodynamic conditions in saline aquifers. Following from Næss (2021), hydrostatic pressure regime is preferable when storing CO_2 underground (Halland et al. 2014). Hydrostatic pressure can be expressed as (Carcione et al. 2006):

$$p = \rho_w g z \tag{3.25}$$

where:
ρ_w = density of the water,
g = acceleration of gravity,
z = depth.

Moreover, pressures points in hydraulically connected formation can be calculated as such (Zhang 2011):

$$p_2 = p_1 + \rho_w g(z_2 - z_1), \tag{3.26}$$

we have that:
p_2 = formation pressure at subscript 2,
z_2 = depth subscript 2,
p_1 = formation pressure at subscript 1,
z_2 = depth subscript 2.

Further, the **temperature** plays in as an important factor on the in-situ conditions. Following from Næss (2021), temperature changes with depth. Fourier's Law of Conduction is central in defining this behaviour (Banks 2012):

$$q = \lambda A \frac{dT}{dZ}, \tag{3.27}$$

where:
q = heat flow,
λ = thermal conductivity,
A = cross-sectional area,
T = temperature,
Z = depth.

The theory about pressure and temperature forms the basis that the most suitable state for the injected CO_2 is in a supercritical state, and thus the pressure and temperature need to have the right conditions. Figure 3.3 illustrates the states of the CO_2 with regards to pressure and temperature. At pressure of 73.9 bar and temperature of 31.10°, the CO_2 is at a supercritical state (Span and Wagner 1996; Lumley 2019). The state of the CO_2 changes thus with depth and figure 3.4 illustrates this behaviour.

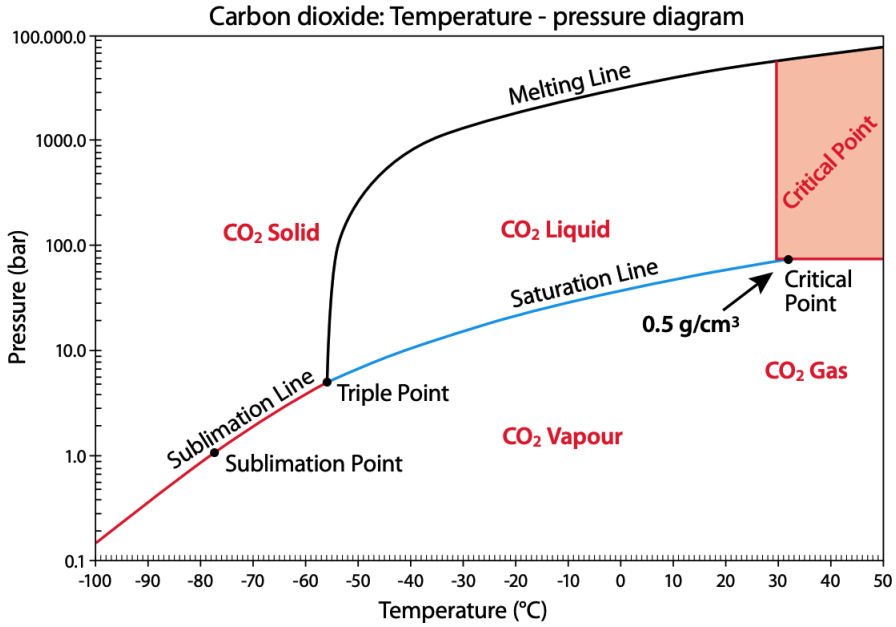

Figure 3.3: Diagram showing the behaviour of CO_2 with regards to temperature and pressure. Figure courtesy of Halland et al. (2011)

3.8 Petrophysical properties

3.8.1 Shale and clay content

The shale and clay volume, V_{sh} and V_{cl}, respectively can be found from the Gamma Ray log readings (Glover 2000):

$$V_{sh} = \frac{GR_{log} - GR_{min}}{GR_{max} - GR_{min}}, \tag{3.28}$$

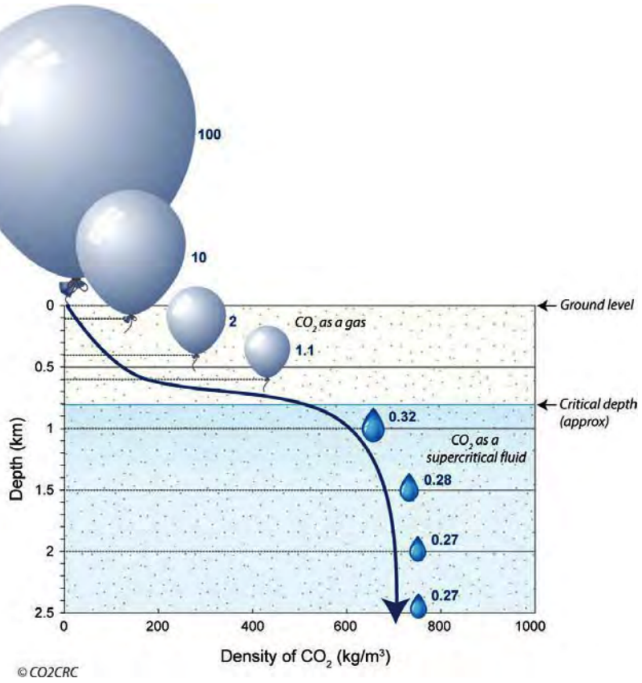

Figure 3.4: Illustration of the state of CO_2 changes vs. depth. Figure courtesy of CO2CRC, taken from Funnell et al. (2008)

where:
GR_{log} = Gamma Ray log readings GR_{min} = Gamma Ray sand trend value GR_{max} = Gamma Ray shale trend value

The clay volume is further related with the Gamma Ray log readings and the volume of shale, V_{sh}:

$$V_{dry-clay} = 0.60 V_{sh} \tag{3.29}$$

Another measurement of the clay volume, taking into account density porosity, ϕ_D, and neutron porosity, ϕ_N measurements are (La Vigne et al. 1994):

$$V_{dry-clay} = \frac{\phi_N - \phi_D - (-0.025)}{\phi_{N-dry-clay}}, \tag{3.30}$$

where $\phi_{N-dry-clay}$ is the porosity dry-clay.

3.8.2 Porosity measurements

With density measurements from the well log, the total porosity, ϕ_t, and the bulk density, ρ_b can be expressed (Ellis and Singer 2007; Glover 2000):

$$\rho_b = \phi \rho_f l + (1 - \phi)\rho_{ma}, \tag{3.31}$$

where ρ_{fl} is the fluid density and ρ_{ma} is the matrix density. Furthermore, the total porosity, ϕ_t, can be expressed in terms of bulk density (Ellis and Singer 2007; Glover 2000):

$$\phi_t = \phi_D = \frac{\rho_{ma} - \rho_b}{\rho_{ma} - \rho_f l}, \tag{3.32}$$

where ϕ_D is density porosity and ρ_b van be desnity readings from log. The total porosity can further be expressed with the neutron porosity, ϕ_N, if neutron logs are available (Ellis and Singer 2007):

$$\phi_t = \phi_a vg = \frac{\phi_N - \phi_D}{2}. \tag{3.33}$$

The effective porosity, ϕ_e can further be related (Dvorkin et al. 2007; Wu and Berg 2003):

$$\phi_e = \phi_t - V_{cl}(\frac{\rho_{ma} - \rho_{cl}}{\rho_{ma} - \rho fl}), \tag{3.34}$$

where V_{cl} is the volume of clay and ρ_{cl} is the density of clay.

3.8.3 Water saturation

The water saturation can be found from following the Archie's synthesis and with resistivity measurements the water saturation, S_w can be expressed as (Ellis and Singer 2007):

$$S_w^n = \frac{a}{\phi^m}\frac{R_w}{R_t}, \tag{3.35}$$

where: m = cementation exponent
a = tortuosity factor
R_w = formation water resistivity
R_t = true resistivity.

Chapter 4

Methodology

This chapter describes the methodology for this master thesis. The theory from chapter 3 is applied. The further steps done to characterize the CO_2 storage resources — based on CO_2 storage capacity and injectivity — are done here. The dataset used in this master thesis is the SMEAHEIA dataset, publicly available from CO2 Storage Data Consortium (2020).

Figure 4.1 visualizes the most central steps in this thesis' seismic quantitative workflow. The proposed workflow demonstrates a contribution of seismically derived CO_2 storage properties to improve storage and injection estimates of geological formations. To perform the different steps of the project, *Petrel 2021* was used for the seismic interpretation, well-tie and depth conversion. Furthermore *Petrel 2021* was used to generate structure maps and inverted I-, ϕ- and k-volumes, as well as kh-estimate derived traffic-light injectivity maps. Python and python scripts inspired by McDonald (2021b) and McDonald (2021a) were used to conduct the petrophysical calulations, create the well panels and cross-plot petrophysical properties. Hampson-Russell´s *Geoview* (Hampson and Russell 1999) was used to aid in the petrophysical calculations, well log interpretation and cross-plotting. *Geoview* was more importantly used to do the post-stack seismic inversion to generate the acoustic impedance volume.

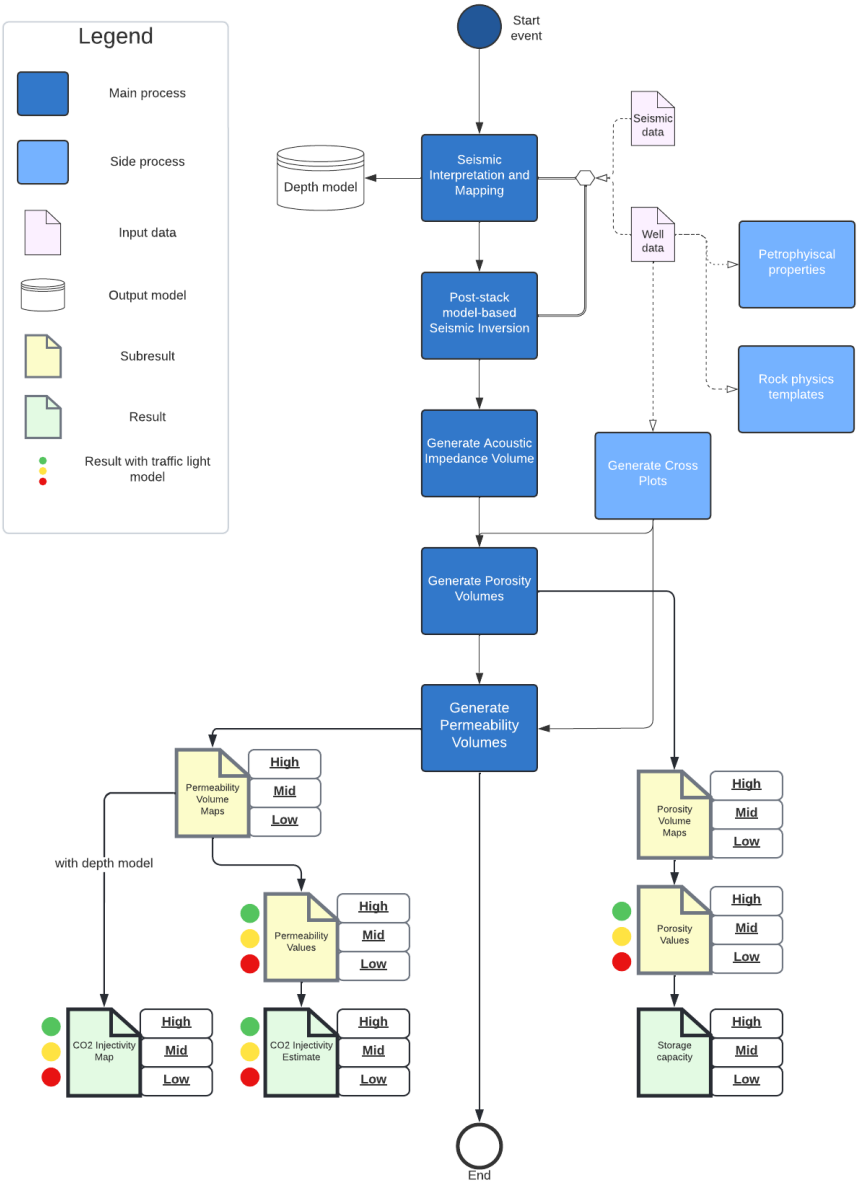

Figure 4.1: Flow-chart for all the steps done for the seismic quantitative process done in this thesis.

4.1 Choice of study area

The SMEAHEIA dataset is one of the datasets publicly available and free to download from CO2 Storage Data Consortium (2020) purely dedicated to study CO_2 storage for academia and industry. Thus, these datasets are important to study and utilize, so the most mature CO_2 storage areas develop fast to actual CO_2 storage projects.

The Smeaheia CO_2 storage area has been evaluated and studied through the years in Bøe et al. (2002), Christensen and Holloway (2003), the Norwegian CO_2 storage atlas (Halland et al. 2011; Halland et al. 2014), Sundal et al. (2014), Dupuy et al. (2018), Miri and Hellevang (2018), Kaufman and Gasda (2018), Ane Lothe et al. (2019), with more. The alpha and beta prospects have been pointed out as the main targets for CO_2 storage in the Smeaheia aquifer. Sognefjord, Fensfjord and Krossfjord Fm constitutes the potential storage reservoir formations of Smeaheia, with Sognefjord as the main target formation. Smeaheia CO_2 storage area has thus been one of the areas evaluated to be chosen for the full-scale CCS project, planned as the *Northern Lights* project (Gassnova 2022). Ross et al. (2013) and Statoil (2016) was studied for this purpose. However, the Johansen formation and the Aurora prospect was chosen as the optimal CO_2 storage prospect for the Norwegian full-scale CCS project (Ane Lothe et al. 2019).

In september 2021 the Norwegian Government licensed out areas for CO_2 storage Ministry of Petroleum and Energy (2021). Smeaheia was one of two areas licensed out. 5th of April, the Smeaheia CO_2 storage license was awarded out to Equinor (Equinor 2022; Ministry of Petroleum and Energy 2022). Thus the Smeaheia area is highly relevant and important to study thorough. In figure 4.2 is a location map of the Horda platform visualizing the Smeaheia area and the Aurora prospect for the Northern Lights project.

4.2 Dataset

4.2.1 Well data and core data

Summary of the wells studied can be seen in table 4.1. As the wells 32/4-1 and 32/2-1 is a part of the Smeaheia CO_2 storage dataset (SMEAHEIA) and within the 3D seismic data area, figure 4.3, these were studied the most. Wells 31/6-6 and 31/6-3 are not a part of the Smeaheia Dataset, but were studied as well to give additional data. Well 31/6-6 is positioned in the Troll gas area and contains gas 7,5 m into the Sognfjord Fm (Den Norske Stats Oljeselskap AS 1984). The gas-filled interval within the Sognefjord Fm was thus not used in the petrophysical calculations.

Well 32/4-1 and 31/6-6 entails core data used for the creation of the poro-perm relationships described more in chapter 4.8. Martin and Lowrey (1997) and Philips

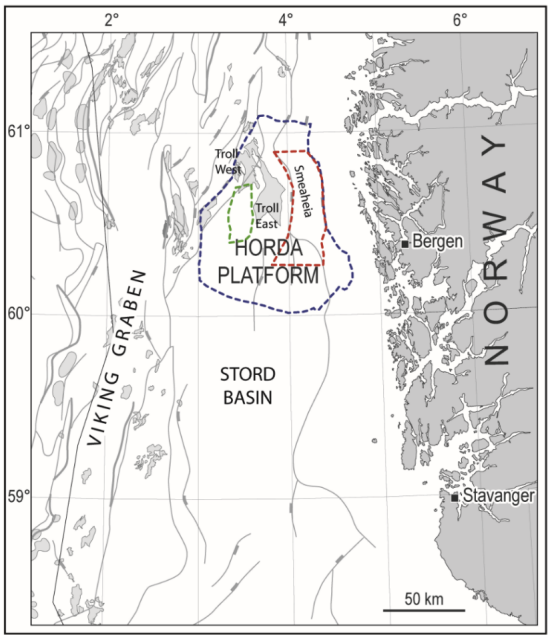

Figure 4.2: Location map of the Horda platform outlining the Smeaheia aquifer in red and Aurora complex in green. Figure courtesy of Ane Lothe et al. (2019).

Petroleum Company (1997) entails 41.25m of conventional core data, core plugs and porosity and permeability data. Statoil AS (1984) entails routine core analysis with porosity and permeability data points.

Well	Year	Type	Status	TVD (m)	Water depth (m)
32/4-1	1996	Exploration	Dry/P and A	3185	312
32/2-1	2008	Exploration	Dry/P and A	1300	351
31/6-6	1984	Exploration	Gas/P and A	2291	313
31/6-3	1983	Exploration	Dry/P and A	2250	301

Table 4.1: Basic information about the wells studied in this thesis (Philips Petroleum Company 1997), (Talisman Energy 2008), (Den Norske Stats Oljeselskap AS 1984), (Norsk Hydro Produksjon AS 2004). Well 32/4-1 and 32/2-1 are the main wells studied.

4.2.2 Seismic dataset

From the Smeaheia CO_2 storage dataset (SMEAHEIA) (from CO2 Storage Data Consortium (2020)), both 2D seismic lines and 3D seismic data were available. The 3D survey TNE01 shot for HYDRO in 2001 and the 3D seismic dataset GN1101 for Gassnova in 2011 were available.

However, the seismic dataset used and studied in this thesis is the 3D seismic dataset GN1101 (GN1101 Dataset 2011). The survey was shot for and collected

by Gassnova with regards to the pre-feasibility study of the Smeaheia CO_2 storage area and the *Troll Kystnær report* (Ross et al. 2013). A general QC of the seismic dataset was done (Liner 1999). The 3D seismic dataset is of general good quality.

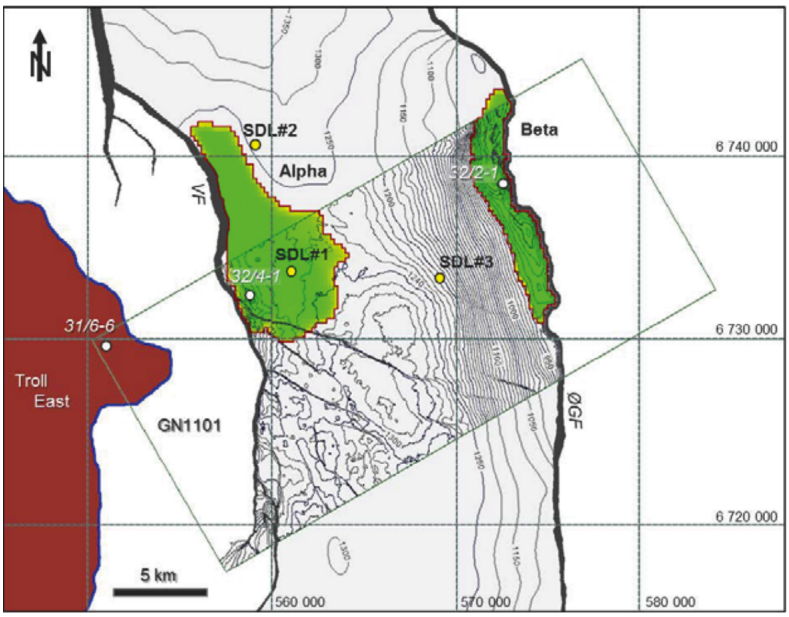

Figure 4.3: Overview map showing the Smeaheia aqufier outlined laterally with the Øygarden fault complex (ØGF) in the east and Vette fault (VF) in the west. The position of wells 32/4-1 and 32/2-1 can be seen within the alpha and beta prospect outline and well 31/6-6 lie in the Troll field area. Lastly the 3D seismic cube GN1101 can be seen. Figure courtesy of Statoil (2016).

4.3 Geological background

The Smeaheia CO_2 storage area can be found in the Norwegian North Sea, within the blocks 32/4 and 32/1 (Statoil 2016; Ross et al. 2013). It is located on the Horda Platform in the Stord Basin and the Troll Field is west for the Smeaheia CO_2 storage area, as seen in figure 4.2. A fault block defines the edges and lateral seals of the storage prospect, with the Vette fault in the west and north and the Øygarden fault complex in the east. Studies from the Ross et al. (2013) further confirms the suitable structural framework and storage formations presence, showing that the prospect sand formations are pinching out southwards.

The Viking Group from middle to upper Jurassic comprises the formations for the Smeaheia CO_2 storage complex (Ross et al. 2013), as seen in figure 4.4. The reservoir formations consists of the shallow-marine to shelf sandstone formations Sognefjord, Fensfjord and Krossfjord. Sognefjord Fm and Krossfjord Fm is the youngest and oldest formation, respectively. The more fine-grained, silty and low porosity Heather Fm was deposited on top of the Sognefjord Fm and further be-

low in the storage prospect interfingering the Sognefjord Fm, Fensfjord Fm and Krossfjord Fm, fig. 4.4) (Ross et al. 2013; Holgate et al. 2013). The low permeable claystone formation Draupne act as the primary caprock formation, and the sealing capacity can be confirmed from the Troll Field penetrated wells (Ross et al. 2013). The younger Shetland and Cromer Knoll Gp can act as additional seal capacity as these groups consist of Cretaceous limestones and shales (Halland et al. 2014).

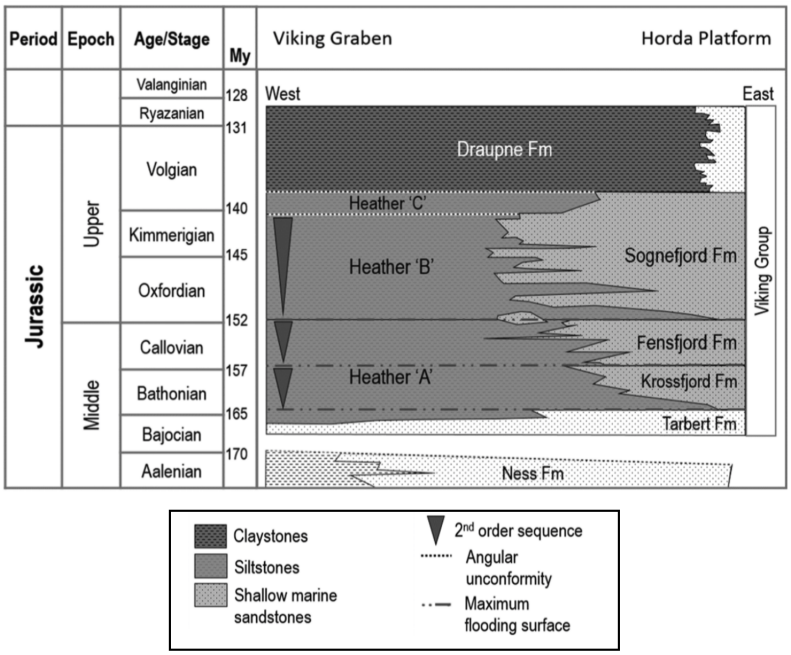

Figure 4.4: Figure of the chronostratigraphic section for the Viking Group with the Sognefjord, Fensfjord and Krossfjord Fm. Figure courtesy of Holgate et al. (2013), taken from Ane Lothe et al. (2019).

4.4 Seismic interpretation

The seismic interpretation strategy, as described in this chapter, is done in these general main steps:

- Establish time-depth relationship
- Well-tie
- Fault interpretation
- Horizon interpretation
- Depth conversion
- Horizons into surfaces
- Generate structure maps

Time-Depth relationship

Check-shot data files for wells 32/4-1 and 32/2-1 were not available from the SMEAHEIA dataset. However, time-depth relationships and check-shot data was possible to generate from the VSP data from the final well report for well 32/4-1 (Philips Petroleum Company 1997) and OWT data from well 32/2-1 (Talisman Energy 2008). Both wells, 32/4-1 and 32/2-1, have P-wave sonic log data for the intervals of interest.

Well-tie

Before time horizons were picked, the wells are tied with the seismic data. The integrated seismic well-tie procedure in Petrel were done, using a Ricker wavelet (Yanghua Wang 2015). This procedure is following the theory of generating synthetic seismograms (Lindseth 1979; Lindseth 1979) and equation 3.8 is applied. The sonic logs were edited and calibrated with the existing time-depth relationships. Figure 4.5 shows the well-tie process focused on the horizons and well tops studied in this thesis from Top Sognefjord Fm to Brent Gp. Figure 4.6 shows the well tie for well 32/4-1 tied to the seismic.

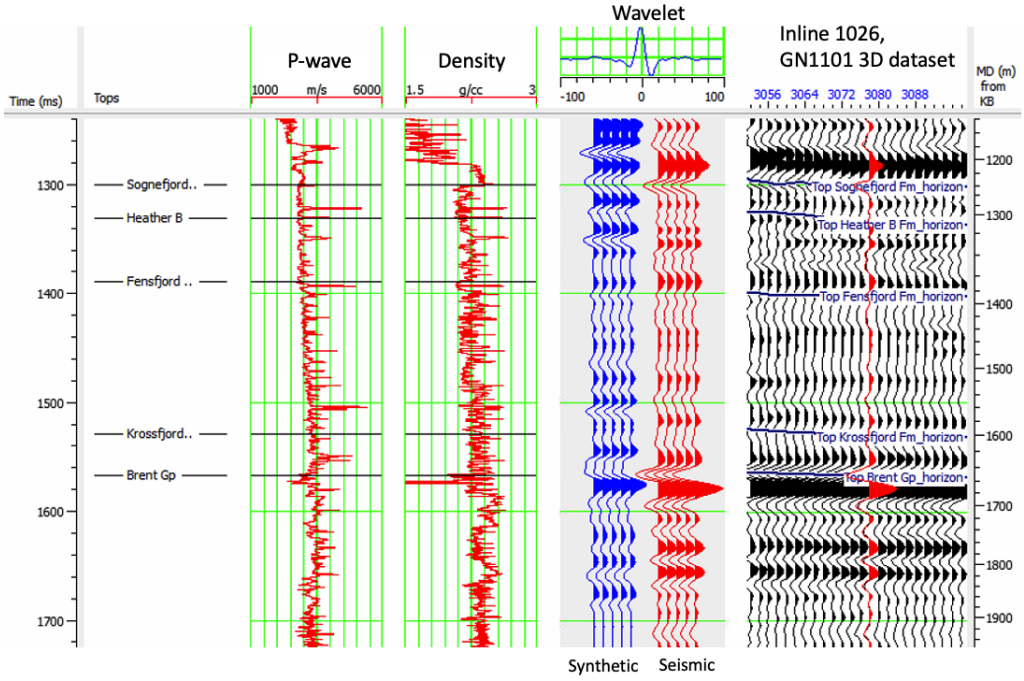

Figure 4.5: Well-tie for well 32/4-1 for the focused horizons and well tops studied in this thesis. Reading from left to the right, the tracks show the P-wave log and Density log. Further the synthetics is shown in blue traces and the seismic in red. Farthest to the right, the synthetic trace is placed over the seismic data, inline 1026.

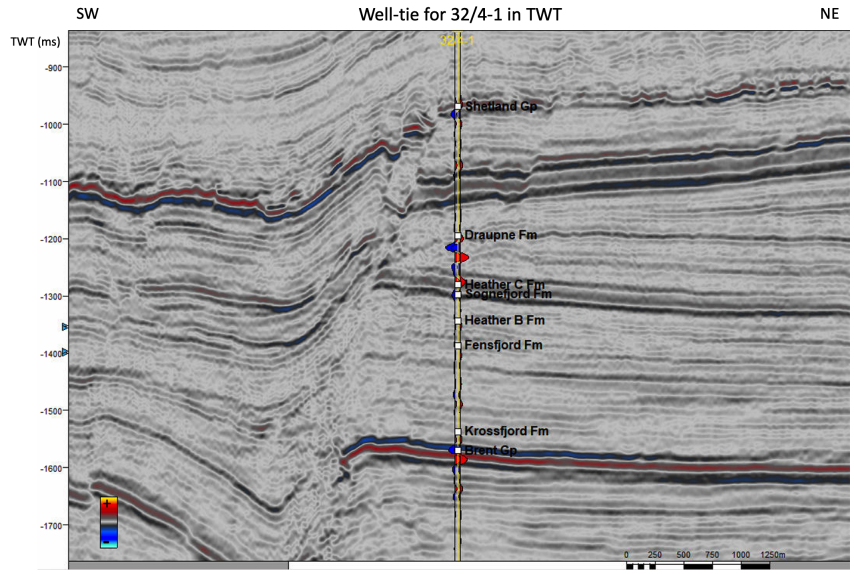

Figure 4.6: Well-tie synthetics for well 32/4-1 overlain at the seismic, seen on inline 1026, from SW to the left and NE to the right.

Fault interpretation

The Smeaheia CO_2 storage dataset (SMEAHEIA) entails a thorough fault interpretation of the Smeaheia area, and for this thesis it was decided to utilize this. The most extensive faults were imported and included in the Petrel project, with the Øygarden fault complex in the north-east and Vette fault in the south-west as the defining fault structures for the lateral boundaries of the Smeaheia storage area (Ross et al. 2013).

Formation tops and horizons picked

Aligned with the well ties and seismic to well calibration, the following formation top horizons were picked and interpreted:

- Seabed
- Base Quaternary
- Top Shetland Group
- Top Draupne Fm
- Top Heather C Fm
- Top Sognefjord Fm
- Top Heather B Fm
- Top Fensfjord Fm
- Top Krossfjord Fm
- Top Brent Group

The most thorough horizon interpretations were made on Top Sognefjord Fm, Top Fensfjord Fm, Top Krossfjord Fm and Top Brent Gp, as these make up the storage reservoir interval, that is most relevant for this thesis. Top Heather B Fm was also studied to try to understand the impact of this formation in the storage reservoir interval. The 3D autotracking tool in Petrel were utilized where it fitted to fulfill the horizon interpretation.

The Smeaheia CO_2 storage dataset (SMEAHEIA) entails interpreted horizons for many of the formations studied in this thesis. These were imported into the Petrel project to QC the trend of the horizons and added value where it fitted the yielding well tie. Figure 4.7 shows the most focused interpreted horizons in this thesis.

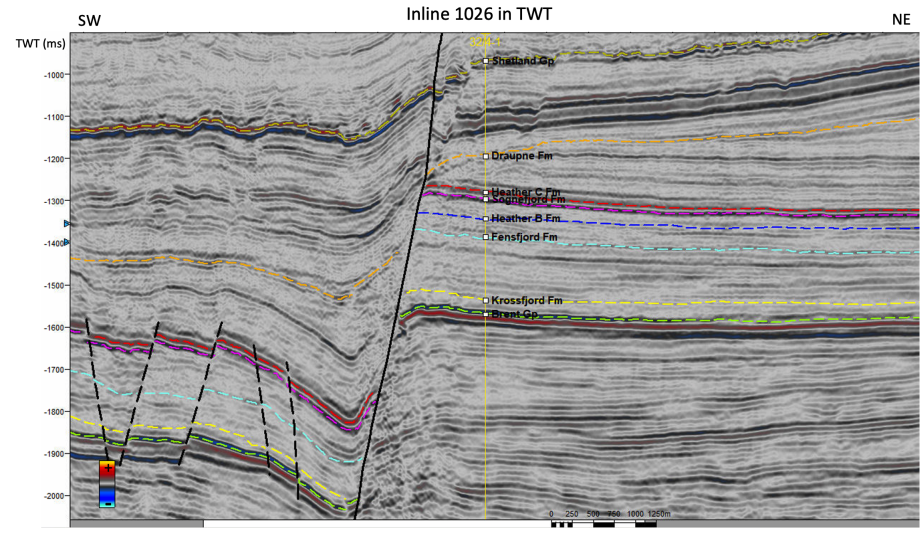

Figure 4.7: The horizons interpreted visualized in inline 1026.

Description of the interpreted horizons:

Top Shetland Group: This horizon was picked on a peak, with a moderate to strong reflection through the dataset.
Top Draupne Fm: The Draupne claystone is interpreted on a peak with moderate reflection throughout.
Top Heather C Fm: Interpreted on a peak, just above Sognefjord Fm.
Top Sognefjord Fm:The horizon is interpreted on a trough with a strong reflection. With the thick overlying and higher velocity layer Draupne Fm and higher velocity and thin layer Heather C Fm, the Sognefjord sandstone Fm is recognized by a decrease in acoustic impedance. The strong reflection identified of Top Sognefjord Fm is recognized well throughout the seismic dataset.
Top Heather B Fm: Picked at a weak reflected trough and difficult to follow through the dataset.
Top Fensfjord Fm: Top Fensfjord Fm was picked at trough, however as a low amplitude from the well tie. With the higher density and velocity Heather B Fm

above, Fensfjord has lower acoustic impedance. The top reflection was moderate to weak and difficult to follow in parts of the dataset.
Top Krossfjord Fm: The Top of Krossfjord Fm was difficult to identify due to low difference in acoustic impedance from the above Fensfjord Fm. However the top of the formation was picked on a trough. The reflection was generally weak throughout the dataset.
Top Brent Group: The top reflection is strong and continuous and picked at a trough. The top Brent Gp reflection was easy to follow.

Depth conversion

To build the depth model and generate surfaces and seismic cubes from the time to depth domain, the velocity model process was done in Petrel. Depth conversion using layers was done as the velocity varies from the overburden and layers below through the interval of interest (Brown 2011). The main steps in the depth conversion were:

- QC of input data.
- Define intervals to build up the layer depth model.
- Correction with well tops.
- Define velocity relationships for each interval.
- Depth conversion.
- QC of the output data.

QC of the input time-depth relationships was first done. Outliers from the generated check-shot data were removed. Constant interval velocities were then picked out from computed interval velocities and built up layer for layer, as seen in figure 4.8. Well tops from well data was used as correction before the velocity model was built. The depth model was then created. Checking eventual mis-ties with well tops and a QC of the depth model was lastly done.

	Base		Correction		Model		
	Surface	Seabed surface	Well tops	Nordland Gp (Well tops 1)	V=V0=VInt	V0: Constant	1480
	Surface	Top Shetland Gp surface	Well tops	Shetland Gp (Well tops 1)	V=V0=VInt	V0: Constant	1900
	Surface	Top Draupne Fm surface	Well tops	Draupne Fm (Well tops 1)	V=V0=VInt	V0: Constant	2600
	Surface	Top Sognefjord Fm surface	Well tops	Sognefjord Fm (Well tops 1)	V=V0=VInt	V0: Constant	2300
	Surface	Top Fensfjord Fm surface	Well tops	Fensfjord Fm (Well tops 1)	V=V0=VInt	V0: Constant	2815
	Surface	Top Krossfjord Fm surface	Well tops	Krossfjord Fm (Well tops 1)	V=V0=VInt	V0: Constant	2981
	Surface	Top Brent Gp surface	Well tops	Brent Gp (Well tops 1)	V=V0=VInt	V0: Constant	3152

Figure 4.8: The velocity model process in Petrel used in the depth conversion.

Make horizons into surfaces and structure maps

From the interpreted horizons, surfaces were further generated through Petrel's "Make surface" process. Polygons were made after purpose of the use of the generated surfaces. Surfaces from the horizons were first made to build up the depth

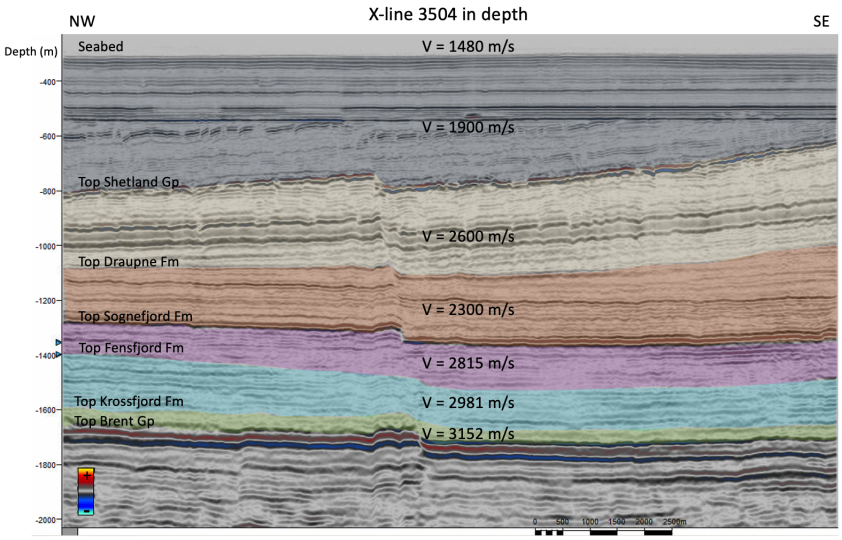

Figure 4.9: The depth model visualized in X-line 3504 with the interval velocities for each layer, starting from the top with the seabed to the deeper Brent Gp.

model. Surfaces were further made to generate TWT and depth structure and thickness maps, based on the depth conversion and velocity model described above in chapter 4.4.

4.5 Petrophysical and rock physics cross-plotting

A petrophysical evaluation is done to initially evaluate the Smeaheia CO_2 storage complex and reservoir formations. A rock physics template cross-plotting is further done, with the petrophysical evaluation taken into consideration, to link the seismic and well data, but also to understand the formations even more with regards to rock physics models.

4.5.1 Petrophysical evaluation

A petrophysical evaluation is done to calculate petrophysical properties, and is a preliminary study of the Smeaheia CO_2 storage formations. This is done to confirm the CO_2 storage potential of the reservoir formations Sognefjord Fm, Fensfjord Fm and Krossfjord Fm. The steps done in the petrophysical evaluation are shown in table 4.2. The wells 32/4-1 and 32/2-1 are central in the petrophysical process done, however the wells 31/6-6 and 31/6-3 was used to aid in the evaluation of the formations and preliminary cross-plotting.

Stage	Process	Details
Step 1	Choose wells	32/4-1 and 32/2-1.
Step 2	Create well panels	Python used (McDonald 2021b).
Step 3	QC of the input logs	Identify intervals with good/bad quality.
Step 4	Petrophysical calculations	ϕ_t, ϕ_e, V_{sh}, V_{cl}, S_w, V_P, V_S, Z_P, Z_S, N/G
Step 5	Create calculated well panels	Python used (McDonald 2021b).

Table 4.2: The steps done in the process of making the porosity volumes.

Step 1, Choose wells: The wells studied in the petrophysical evaluation in this thesis are 32/4-1 and 32/2-1. The wells 32/4-1 and 32/2-1 are a part of the SMEAHEIA dataset and are positioned within the GN1101 3D seismic cube.

Step 2, Create well panels: The well panels are generated using Python (McDonald 2021b), see code example in appendix chapter E. Well panels are made for the intervals of interest. The intervals of interest are the formation intervals with the tops considering:

- Lower interval of Draupne Fm
- Heather C Fm
- Sognefjord Fm
- Heather B Fm (only identified in well 32/4-1)
- Fensfjord Fm
- Heather A Fm (only identified in well 32/4-1)
- Krossfjord Fm
- Upper interval of Brent Gp

Well panel for well 32/4-1 is shown in figure A.1 and well panel for well 32/2-1 is found in figure A.3 in chapter A.

Step 3, QC of the input logs: A quality check of the the input logs from the wells were done and intervals of good and bad quality were identified. Guidelines from Glover (2000) and Ellis and Singer (2007) are applied, but some of the QC elements for the well logs were:

1. Check of the density correction curve for the mudcake compensation (Glover 2000; Ellis and Singer 2007), whether it is greater ± $0.15 g/cm^3$. If so, the density readings might not be reliable: The density correction logs looks acceptable for both the wells 32/4-1 and 32/2-1.
2. Check for cavings with the caliper and bit size logs (Glover 2000).
3. Data quality discussions from well reports (well report 32/4-1 og 32/2-1).

Generally it is observed that well 32/2-1 has better data quality than 32/4-1. This is also confirmed from well report 32/2-1 (Talisman Energy 2008) where it is concluded that the data is of generally good quality. For well 32/4-1, however, problems occurred due to washout (Philips Petroleum Company 1997). Even though, it is concluded in well report 32/4-1 (Philips Petroleum Company 1997) that the data gathered was acceptable.

Step 4, Petrophysical calculations There are no shear-wave well data, so V_S is calclulated using Greenberg-Castagna relation (Greenberg and Castagna 1992), see chapter 3.2.2 and equation 3.15. Well panels with calculated ϕ_t, ϕ_e, V_{sh}, V_{cl}, V_P, V_S, P- and S-impedance are shown in appendix chapter A and table 4.4, 4.5 and 4.6 shows the key values calculated the formation evaluation of Sognefjord, Fensfjord and Krossfjord Fm, resepectively. Table 4.3 shows how the petrophysical properties were calculated.

Property	Symbol	Details
Volume shale	V_{sh}	Eq.3.28
Volume clay	V_{cl}	Eq.3.29 and 3.30
Total porosity	ϕ_t	Eq.3.32 and 3.33
Effective porosity	ϕ_e	Eq.3.34
Water saturation	S_w	Eq.3.35
P-wave velocity	V_P	Acoustic log conversion to m/s
S-wave velocity	V_S	Eq.3.15 (Greenberg and Castagna 1992)
P- and S-impedance	I_P, I_S	Eq.3.5 and 3.6
Net to gross	N/G	V_{clay}<25, ϕ_t >0.15

Table 4.3: The calculations done in the petrophysical evaluation.

Below are some process steps taken into account when generating the petrophys-

ical properties:

- V_cl calculated from neutron-density logs (eq.3.30) is a more accurate way of estimating clay volume than directly from the GR-log (eq.3.29), because the GR-log often give an overestimation of the clay content (Glover 2000). Thus V_{cl} was calculated with eq.3.30 if neutron logs were available. This was not the case for well 32/4-1, hence eq.3.29 was used for well 32/4-1 and eq.3.30 for well 32/2-1.
- Following from the above bullet point, the neutron logs were utilized where it was available, and so in the porosity calculations of ϕ_t and ϕ_e.
- To calculate the N/G cut-offs for the porosity and clay ranges were set to decide the reservoir sand intervals in the formations. For this thesis the net reservoir cut-offs were set to V_{clay}<25 and porosity values ϕ_t >0.15.

Porperties	**well 32/4-1**	**well 32/2-1**
Thickness (m)	68	110
ϕ_t (%)	30.3	29.5
ϕ_e (%)	29.9	27.2
V_{sh} (GR log) (%)	22.5	33.0
V_{cl} (GR log) (%)	13.5	19.8
V_{cl} (D-N logs) (%)	-	19.9
S_w (%)	∼100	∼100
N/G (m/m)	0.75	0.6

Table 4.4: Mean values of the petrophysical calculations for Sognefjord Fm.

Properties	**well 32/4-1**	**well 32/2-1**
Thickness (m)	229	103
ϕ_t (%)	24.0	26.9
ϕ_e (%)	23.5	24.2
V_{sh} (GR log) (%)	27.8	31.2
V_{cl} (GR log) (%)	16.7	18.7
V_{cl} (D-N logs) (%)	-	22.3
S_w (%)	∼100	∼100
N/G (m/m)	0.65	0.57

Table 4.5: Mean values of the petrophysical calculations for Fensfjord Fm.

Properties	well 32/4-1	well 32/2-1
Thickness (m)	47	72
ϕ_t (%)	19.6	26.4
ϕ_e (%)	19.1	16.8
V_{sh} (GR log) (%)	25.5	57.2
V_{cl} (GR log) (%)	15.3	34.3
V_{cl} (D-N logs) (%)	-	61.3
S_w (%)	∼100	∼100
N/G (m/m)	0.66	0.3

Table 4.6: Mean values of the petrophysical calculations for Krossfjord Fm.

Step 5, Create calculated well panels: Well panels for the calculated ϕ_t, ϕ_e, V_{sh}, V_{cl}, V_P, V_S, I_P, I_S are finally made. This is done in the same process as step 3 above. The calculated well panels for well 32/4-1 and 32/2-1 are found in figure A.2 and A.4 in appendix chapter A.

4.5.2 Cross-plots and rock physics models

The next process with utilizing the well data is to create cross-plots of the petrophysical properties. Firstly the studied formations is cross-plotted against each other with rock physics models. As rock physics is the link to understand reservoir properties and seismic data (Z. Wang 2001), this aid in understanding of the interpreting the seismic reflection between the data. Secondly, cross-plots with the studied formations using rock physics models help characterize the formations even more and can aid in the interpretation of the seismic inverted results. In this study, the Greenberg-Castagna relation (Mavko et al. 2020; Greenberg and Castagna 1992) with the modelled wet sand and shale trend lines are used in the V_P/V_S vs. I cross-plots. Furtermore, the contact cement model is applied (Dvorkin and Nur 1996; Mavko et al. 2020) in V_P vs. ρ cross-plots for Sognefjord Fm and Fawad et al. (2021) was studied. The V_P/V_S vs. I cross-plotting is shown from well 32/4-1 in figure 4.10 and 4.11.

Lastly, cross-plotting of petrophysical properties aid in creating the relationship between the properties studied in thie thesis; acoustic impedance, porosity and permeability. In this study, impedance-porosity and poro-perm relationships are generated from the cross-plots. This is described more in chapter 4.7 and 4.8.

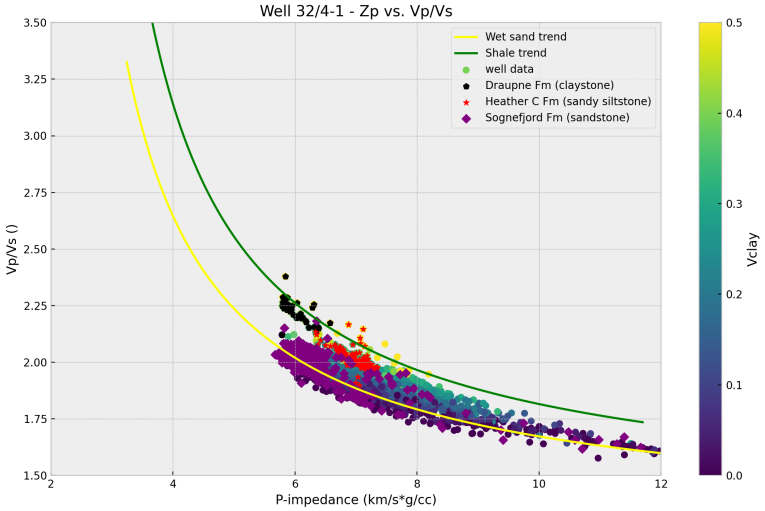

Figure 4.10: Vp/Vs is plotted against P-impedance, with the wet sand and shale trend lines.

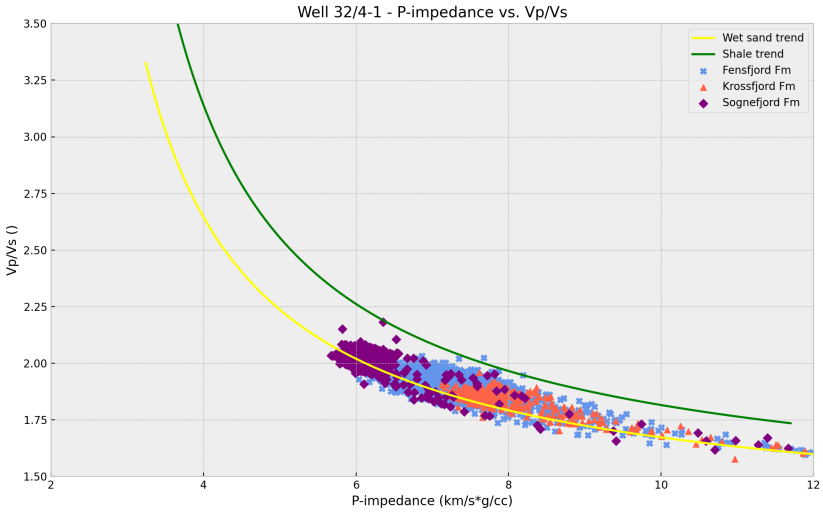

Figure 4.11: Vp/Vs is plotted against P-impedance, with the wet sand and shale trend lines, for the formations.

4.6 Seismic inversion: Post-stack inversion

A seismic post-stack inversion is done to generate an acoustic impedance volume. The process is done in Hampson-Russells Geoview software with the Post-stack

Acoustic Impedance Inversion workflow, that is based on the STRATA model building (Hampson and Russell 1999) and the theory from chapter 3.3.1. A deterministic model-based inversion is done (Simm and Bacon 2014), and the steps done in the workflow is shown in table 4.7.

Stage	Process	Details
Step 1	Select Post-stack seismic	GN1101 3D seismic dataset (GN1101 Dataset 2011)
Step 2	Select horizons	Smeaheia CO_2 storage reservoir interval.
Step 3	Select wells	Well 32/4-1 chosen for the model.
Step 4	Check shot correction**	Time-depth relationship from well 32/4-1.
Step 5	Correlate the wells	Well-tie 32/4-1 and seismic; figure 4.5.
Step 6	Extract wavelet	Wavelet from well 32/4-1 extracted.
Step 7	Build initial model	Input: well 32/4-1 and horizons.
Step 8	Inversion analysis	Model-based inversion was run; figure 6.3
Step 9	Apply to volume	Time window: 500-2200ms.
Step 10	QC Inverted Results	More discussion in 6.5

Table 4.7: All the steps done in the post-stack inversion workflow in Hampson-Russells Geoview software. *Steps added to the default post-stack inversion workflow in Geoview.

Veeken et al. (2004) and Simm and Bacon (2014) address well the model-based inversion procedure. A post-stack model-based inversion generates, in an iterative process, a synthetic response and an inverted impedance volume from starting with an initial model. With utilizing the seismic and well data, a wavelet is extracted and inverted synthetic trace made. The synthetic trace output is compared with the original seismic and an error is calculated. Through a number of iterations with generating new possible solutions for the resulting inverted synthetic trace, the inverted acoustic impedance volume is generated with the least error solution. A generalized flow-chart of the workflow in the model-based inversion process in this thesis, is seen in figure 4.12. This is incorporated in the working process when going through the steps in table 4.7. The inversion QC checklist from Simm and Bacon (2014, p.209) is followed when doing the post-stack inversion. Figure 4.12 illustrates some of the key steps from table 4.7 further described:

Step 1, Select Post-stack seismic: For this thesis it is needed to generate a porosity volume of the CO_2 storage reservoir. Therefore, a post-stack acoustic impedance inversion method generating an acoustic impedance volume is fit for this thesis purpose. As described more in detail in chapter 4.5.2, with an acoustic impedance volume it is possible to link the porosity reservoir conditions.

Step 2, Select horizons: The focus in this thesis is the CO_2 storage reservoir interval, therefore the focus and the horizons chosen to build the inversion model are; Top Sognefjord Fm, Top Fensfjord Fm, Top Krossfjord Fm and Top Brent Gp.

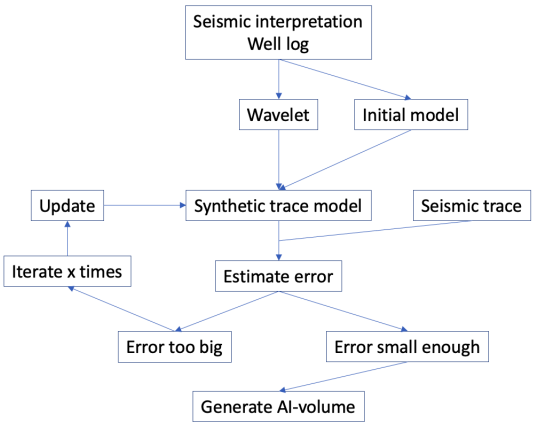

Figure 4.12: Generalized flow-chart of the model-based inversion workflow in this thesis. Figure moderated from Simm and Bacon (2014, p. 201) and Veeken et al. (2004, p. 60)

These horizons were imported from the Petrel project and seismic interpretation done. Top Heather B Fm was also imported, to understand the impact of that interbedding layer between Sognefjord Fm and Fensfjord Fm. These horizons make up the macro model (Veeken et al. 2004).

Step 6, Correlate the wells: Well 32/4-1 was used as the preference well for well-tie in the seismic inversion model. The well-tie is done in the interval with focus from top Sognefjord Fm till top Brent Gp, the same interval defining the intial impedance model. Time-depth relationship from well 32/4-1 and the well tops were used to stretch and apply shifts to tie the seismic and well. Figure 4.5 shows the well-tie process from Geoview with well 32/4-1 tied to the seismic.

Step 7, Extract wavelet: The different wavelet extractions methods in Geoview and STRATA model building is addressed in chapter 3.3.2. In the workflow, both a statistical wavelet and wavelet from well was extracted. This was done to run multiple models and check the errors in step 8, and see what would give the best fit for the projects' purpose. For this project, the wavelet extracted from well 32/4-1 was used in the final inverted impedance volume to set the constant phase. It had a phase average at 35 degrees. The amplitude spectrum is determined from the seismic data. It was decided that this would give the most correct information about the phase spectrum, as this is extracted from the well log, however issues linked to the wavelet is discussed in chapter 6.5. The wavelet extracted can be seen in figure 4.13.

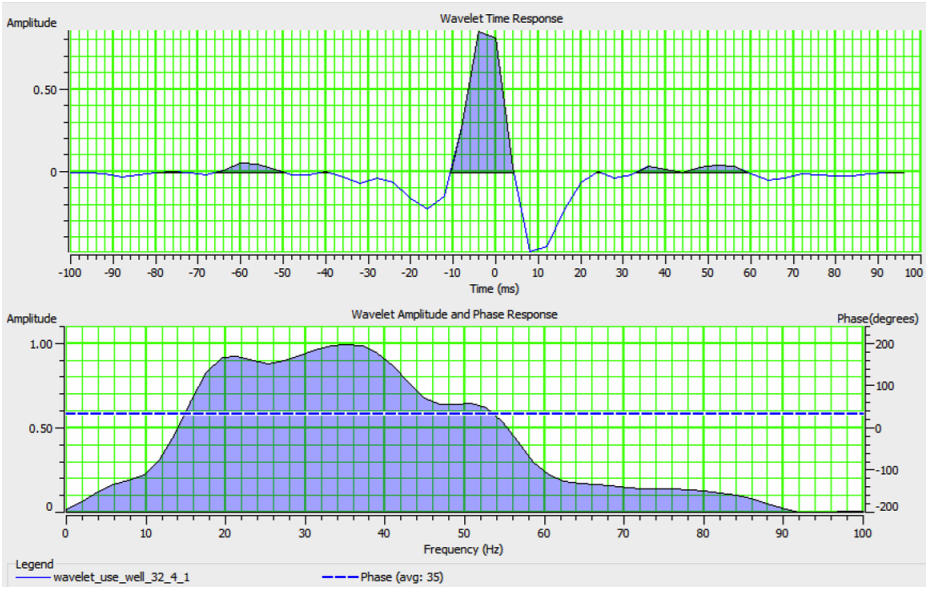

Figure 4.13: The wavelet extracted from well 32/4-1 is shown as a time response and the frequency with the wavelet amplitude and phase response is shown. We have a phase average 35 degrees.

Step 8, Inversion analysis: Model-based inversion can give acceptable results when lack of well control (Veeken et al. 2004). Therefore, a model-based inversion was run in step 8, set with an average block size on 4ms. The inversion was run and then further analyzed with different versions, as f.ex with wavelets as described in step 7. The inversion analysis with the final inverted synthetic trace is visualized in figure 6.3 in the discussion.

Step 10, QC Inverted Results: Inversion analysis in step 9 with well 32/4-1 and cross validation, a blind test, with well 32/2-1 was done to QC the inverted result. These two wells are the only wells in the relevant project area for this thesis. Only one well was decided to use as input to the initial model, so the other well could be used for cross validation. See 6.5 for more discussion.

4.7 Porosity volumes

The acoustic impedance volume that is generated from the process in chapter 4.6 builds the basis for the next step in the seismic quantitative demonstration in this thesis; conducting porosity volumes for porosity estimations and trend analysis. Rock physics links seismic attributes and reservoir properties, if general statistical impedance and porosity relationships are known (Z. Wang 2001). A common way of linking acoustic impedance to porosity is to use rock physics measurements from well data to create impedance-porosity trends and relationships (Dvorkin and Alkhater 2004). This can be done by cross-plotting P-wave acoustic impedance

against porosity and create regression expressions (Guidish and De Buyl 1987; Maureau and Van Wijhe 1979; Angeleri and Carpi 1982).

In this thesis P-impedance and porosity is cross-plotted and regression formulas are made for the reservoir intervals in Sognefjord Fm, Fensfjord Fm and Krossfjord Fm. Impedance-porosity correlations vary from a lithological unit to another (Rasmussen and Maver 1996). Thus, the impedance-porosity relationships for Sognefjord Fm, Fensfjord Fm and Krossfjord Fm are studied individually, and regression formulas are further created. The porosity volumes of Sognefjord Fm, Fensfjord Fm and Krossfjord Fm are further created based on these correlation formulas.

This process is firstly done to investigate the porosity trends for the formations Sognefjord, Fensfjord and Krossfjord, and for the alpha and beta prospects. Secondly, it is done to further use these values in the calculations of CO_2 storage capacity in the prospects and formations.

The steps in this process is presented in table 4.8. Python and Hampson Russells' Geoview is used to cross-plot measured total porosity and P-impedance from the well data and to generate the regressions formulas. Code example used in Python can be find in appendix chapter E. Petrel is used to generate the porosity volumes from the impedance volume made in chapter 4.6.

Stage	**Process**	**Details**
Step 1	Choose wells	Well 32/4-1 and 32/2-1.
Step 2	Calculate porosity and impedance	From chap.4.5.1
Step 3	Cross-plot impedance vs. porosity	Done in Python and Geoview.
Step 4	Remove outliers	Trend analyses.
Step 5	Regression and trend analysis	Formulas extracted.
Step 6	Generate porosity volumes and maps	Done in Petrel.
Step 7	Extract porosity values	Mean porosity values.
Step 8	Uncertainty quantification	More in chap. 6.6

Table 4.8: The steps done in the process of making the porosity volumes.

More details on the steps done in table 4.8 are described below:

Step 1, Choose wells: Well data from wells 32/4-1, 32/2-1, 31/6-6 and 31/6-3 were available for this thesis. However, only well 32/4-1 and 32/2-1 was used to calculate total porosity and P-impedance, done in chapter 4.5.1, and further used in the cross-plotting of P-impedance and porosity. Well 32/4-1 and 32/2-1 penetrate the alpha and beta prospects, respectively, and lie in the relevant project area, within the boundaries of the Vette and Øygarden fault complex, in the GN1101 3D seismic cube. Therefore it is believed that using these two wells would give more accurate impedance-porosity values for the formations within the project

area and for the alpha and beta prospects.

Step 2, Calculate porosity and p-impedance: Total porosity and acoustic P-wave impedance, P-impedance, is used in the cross-plot. This was calculated from density and sonic logs from the wells 32/4-1 and 32/2-1, done in chapter 4.5.1.

Step 3, Cross-plot impedance vs. porosity: Cross-plotting of the p-impedance and total porosity of the data was mainly done in Python, code example is found in E. Geoview was also used to aid in the cross-plotting of understanding the well data with the built-in cross-plotting function.

Step 4, Remove outliers: The trend of the plotted data was studied and outliers were picked and removed to get a better fit of the regression done on the data. The outliers were picked manually.

Step 5, Regression and trend analysis: Least square polynomial linear regression is run with standard error lines applied. Formulas are extracted from the main regression best fit line and from both error lines. The error lines are generated to quantify the uncertainty of the best fit regression line. This is further used to create different scenarios of the porosity volumes and estimates in a high-case, mid-case and low-case. We create such a spread in order to be able to state with a high level of confidence that the result is within that boundary. The plotted regression lines and formulas extracted for Sognefjord, Fensfjord and Krossfjord Fm are found in chapter 4.7.1, 4.7.2 and 4.7.3, respectively.

Step 6, Generate porosity volumes and maps: The formulas extracted from the regression analysis is used in direct relation to the seismic inverted acoustic impedance volume generated from chapter 4.6. The calculator tool in Petrel is used to do the calculation from generating the acoustic impedance volume into high-case, mid-case and low-case porosity volumes. The volumes are further made into maps and run in the "Surface attributes" function in Petrel with the top and base as constraints for each formation. The attribute "Average magnitude" was used for the formations and the attribute "Interval average: Maximum" was used for the prospects. The average magnitude maps for the mid-case volumes are in chapter 5.2.

Step 7, Extract mean porosity values: The mean porosity values from the maps generated in step 6 are extracted. These values are used in the CO_2 storage capacity estimations in chapter 4.9.2 and 4.9.1.

Step 8, Uncertainty quantification: As there will always be uncertainty and error in the data used and approximations done, uncertainty quantification is important to do (Avseth et al. 2005). To quantify some of the uncertainty that contains in the data used to generate the impedance-porosity relationship, and thus the porosity volumes, an uncertainty quantification is therefore done for the input data, P-impedance and total porosity. Error lines is generated for the regression best fit line

and described in step 5 above. Histograms with kernel estimates for the probability density function, pdf, is made (Avseth et al. 2005). This is presented and discussed more in chapter 6.6.

4.7.1 Sognefjord Formation

P-impedance and total porosity from wells 32/4-1 and 32/2-1 are, as described above, plotted against each other. Figure 6.6 is including outliers and visualizing all the data points with gamma ray values, to have a first sight at the data before the regression is done. Outliers were then picked and removed, as in the step 4 from table 4.8. Transparency is applied at the data points to visualize the main trends of the data.

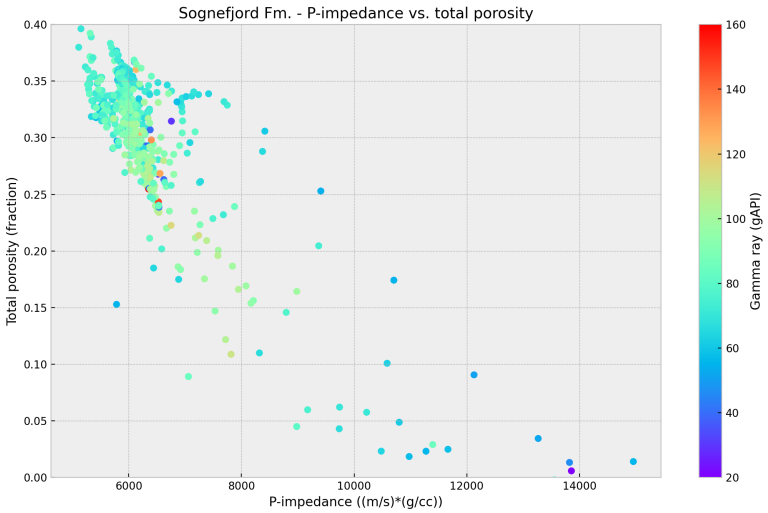

Figure 4.14: Cross-plot of P-impedance vs. total porosity for Sognefjord Fm, data points from wells: 32/4-1 and 32/2-1. The data points are painted with their corresponding GR-value.

From figure 4.15 we see a good correlation for the best fit line at 0.93. The error was found to be ≈ 0.02 around the regression line at the y-values. The regression lines are further extracted in table 4.9.

4.7.2 Fensfjord formation

Figure 4.16 show a correlation of the regression line of 0.94. The error is ≈ 0.02 for the y-values scattered from the regression line. Regression lines are extracted in table 4.10.

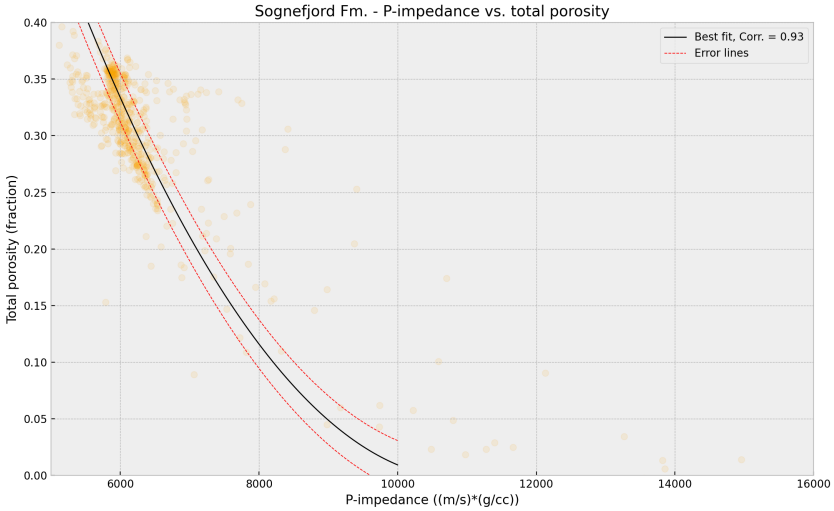

Figure 4.15: Cross-plot p-impedance vs. total porosity for Sognefjord Fm, best fit line with error, data points from wells: 32/4-1 and 32/2-1. Outliers are excluded in the regression analysis and visualized with high transparency.

Scenario	Expression
High-case	$y = 1.67 - 0.0003x + 1.39 * 10^{-8}x^2$
Mid-case	$y = 1.65 - 0.0003x + 1.39 * 10^{-8}x^2$
Low-case	$y = 1.63 - 0.0003x + 1.39 * 10^{-8}x^2$

Table 4.9: P-impedance vs. total porosity linear least square regression relationship equations for Sognefjord Fm from figure 4.15, where x = acoustic impedance and y = porosity.

Scenario	Expression
High-case	$y = 1.40 - 0.0002x + 8.85 * 10^{-9}x^2$
Mid-case	$y = 1.38 - 0.0002x + 8.85 * 10^{-9}x^2$
Low-case	$y = 1.36 - 0.0002x + 8.85 * 10^{-9}x^2$

Table 4.10: P-impedance vs. total porosity linear least square regression relationship equations for Fensfjord Fm based on figure 4.16, where x = acoustic impedance and y = porosity.

4.7.3 Krossfjord formation

The cross-plot in figure 4.17 shows a correlation at 0.88 for the regression line for the data points from Krossfjord Fm. The error in the y-direction is ≈ 0.03. The linear regression lines get the expressions in table 4.11.

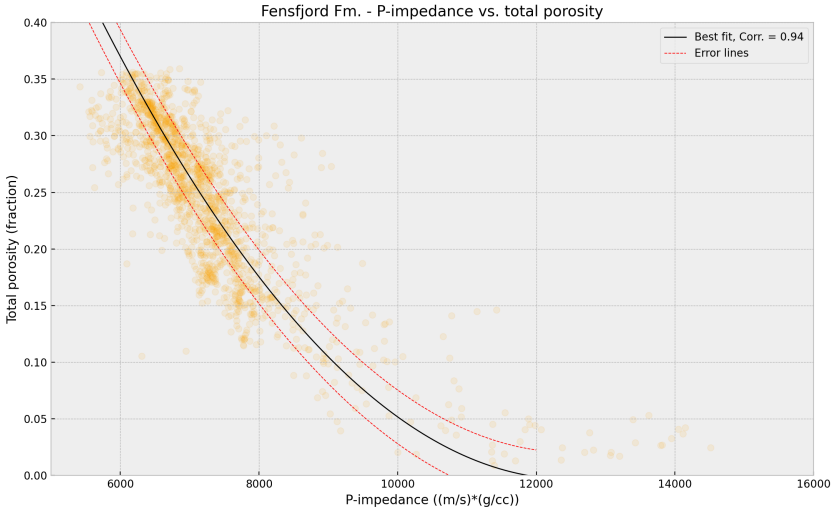

Figure 4.16: Cross-plot p-impedance vs. total porosity for Fensfjord Fm, best fit line with error, data points from wells: 32/4-1 and 32/2-1. Outliers are excluded in the regression analysis and visualized with high transparency.

Scenario	Expression
High-case	$y = 1.45 - 0.0002x + 9.4 * 10^{-9}x^2$
Mid-case	$y = 1.42 - 0.0002x + 9.4 * 10^{-9}x^2$
Low-case	$y = 1.39 - 0.0002x + 9.4 * 10^{-9}x^2$

Table 4.11: P-impedance vs. total porosity linear least square regression relationship equations for Krossfjord Fm based on figure 4.17, where x = acoustic impedance and y = porosity.

4.8 Permeability volumes

Porosity is one of the main contributor to affect permeability. Thus, porosity is used often to measure permeability (Ellis and Singer 2007; Glover 2000). The next step in the quantitative demonstration is thus to utilize the porosity volumes, to generate permeability volumes and measurements. A clear trend is often seen, when plotting permeability against porosity (Glover 2000). The plotting is often done with permeability on a logarithmic scale and porosity on a linear scale. On a logarithmic scale, the porosity and permeability is often suggested to follow a linear relationship (Ellis and Singer 2007). The porosity-permeability plots should be plotted for clear defined reservoir units to get the best fit for the desired unit (Glover 2000).

From the well report for well 32/4-1, porosity and permeability measurements

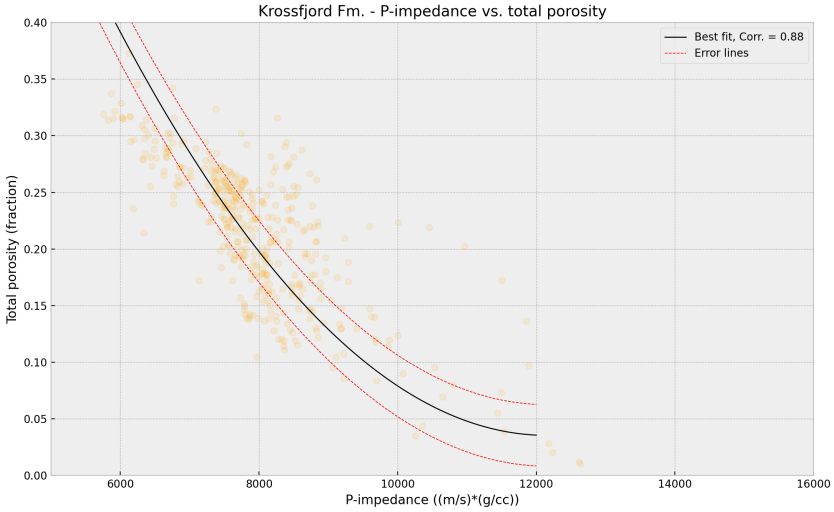

Figure 4.17: Cross-plot of P-impedance vs. total porosity for Krossfjord Fm, best fit line with error, data points from wells: 32/4-1 and 32/2-1. Outliers are excluded in the regression analysis and visualized with high transparency.

from conventional core analysis are available for Sognefjord Fm. For Fensfjord and Krossfjord Fm, well 31/6-6 core measurements were used. Core horizontal permeability (k_{Hor}) and helium porosity were thus plotted against each other. These relationships are further used to generate the permeability volumes. Table 4.12 shows the general approach in this part of the workflow.

Stage	Process	Details
Step 1	Check for core data	Well 32/4-1 and 31/6-6.
Step 2	Cross-plot k vs. ϕ	Done in Python and Geoview.
Step 3	Remove outliers	Trend analysis.
Step 4	Semi-log linear regression	Formulas extracted.
Step 5	Generate the volumes and maps	Done in Petrel.
Step 6	Extract permeability values	Mean permeability values.
Step 7	Uncertainty quantification	Analysis of the data.

Table 4.12: The steps done in the process of making the permeability volumes.

The steps done in table 4.12 follows the same approach as in 4.7, however below are details on the steps done for generating the permeability volumes, where the process of Sognefjord Fm is used as an step-wise example:

4.8.1 Sognefjord Fm

Step 1, Check for core data: From the well report for well 32/4-1, porosity and permeability measurements from conventional core analysis with 61 plugs are available Philips Petroleum Company (1997). The conventional core analysis was done by GeoQuest Schlumberger, Stavanger. These plugs were cored from Heather C Fm and Sognefjord Fm. Five reservoir zones are defined within the cored zones in the final well report (Philips Petroleum Company 1997), where three of these are defined in the Sognefjord Fm.

Step 2, Cross-plot permeability vs. porosity: The measured porosity and horizontal permeability from the core analysis were picked out from tables 2.1-2.5 from the final well report for well 32/4-1 (Philips Petroleum Company 1997). These values were plotted on a logarithmic scale for the zones defined in Sognefjord Fm. As in chapter 4.7 Python and Geoview was used in the same approach to cross-plot the data. Out of the total 61 plugs measurements, 43 of these are in the Sognefjord Fm reservoir interval, in the measured depth interval 1241.50-1275.10m

Step 3, Remove outliers: As the dataset of measured core data points was not that crowded, the most clear outliers were picked and excluded for the regression. This was done manually.

Step 4, Semi-log linear regression: A linear regression on the semi-log is done to create the porosity-permeability relationship, seen in figure 4.18. The regression formulas, with standard error lines as the high- and low-case scenarios, are extracted in table 4.13

Step 5, Generate permeability volumes and maps: The relationship created from regression is used directly to create the permeability volumes. From chapter 4.7 three porosity volumes were created as a low, mid- and high case scenario. These three scenarios are used further in the porosity-permeability relationship as three different inputs, to generate a low-, mid- and high-case scenario for the permeability cubes as well. As in chapter 4.7, the volumes are made into maps and run in the "Surface attributes" function in Petrel with the top and base as constraints for each formation. The attribute "Average magnitude" was used. The mid-case average magnitude maps can be found in chapter 5.3.

Step 6, Extract mean permeability values: The mean permeability values from the inverted volume maps for the formations and prospects are extracted. These values are further used into the CO_2 injectivity estimations described further in chapter 4.10.

Step 7, Uncertainty quantification: The measured horizontal permeability and porosity from the conventional core analysis from well 32/4-1 entails of substantially less data than for the impedance-porosity data used in chapter 4.7, and it is

therefore important to study the spread of the data used as input for creating the porosity-permeability relationship.

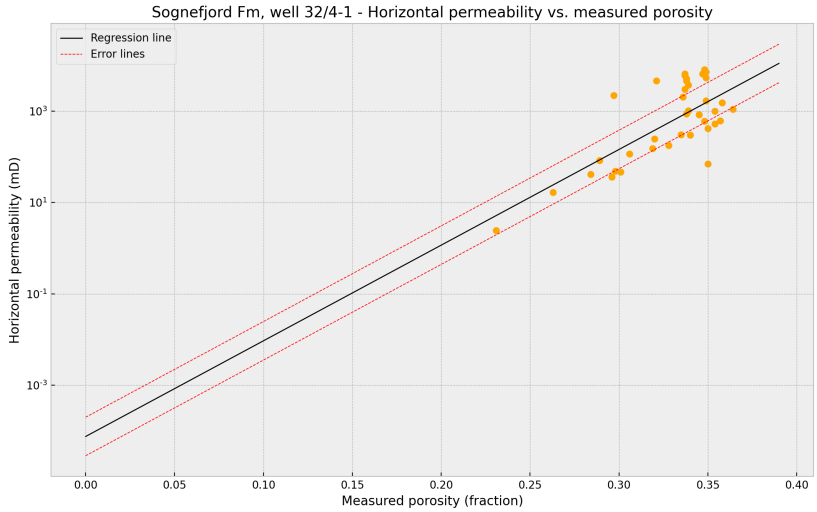

Figure 4.18: Horizontal permeability vs. measured porosity for Sognefjord Fm, best fit line with error. Data points from conventional core analysis from well 32/4-1.

Scenario	Expression
High-case	$log(y) = 48.24x_{high} - 8.52$
Mid-case	$log(y) = 48.24x_{mid} - 9.49$
Low-case	$log(y) = 48.24x_{low} - 10.46$

Table 4.13: Porosity-permeability relationship created for Sognefjord Fm, with core data from well 32/4-1, where x = porosity volume and y = permeability volume.

4.8.2 Fensfjord Fm

The same approach as described above and in table 4.12 was followed, however some details along the process of Fensfjord Fm is described below:

Step 1, Check for core data: As there are no core plugs taken in the Fensfjord interval from neither well 32/4-1 or 32/2-1, other wells nearby with core measurements had to be considered. Therefore, as the nearby well 31/6-6 consisted of core measurements from the Fensfjord interval, this well was used.

Step 2, Cross-plot permeability vs. porosity: From the petrophysical evaluation report for well 31/6-6, there exists poro-perm regression equations based on cross-plots of the measured helium porosity and horizontal permeability in the intervals

1500-1561m and 1561-1775 (Statoil AS 1984; Den Norske Stats Oljeselskap AS 1984). To exclude the Heather B Fm and other formation intervals than Fensfjord Fm, a new poro-perm relationship was made for this thesis. The measured helium porosity and horizontal permeability values within the Fensfjord Fm, 1719-1755.50m, from the routine core analysis report (Statoil AS 1984) was thus cross-plotted.

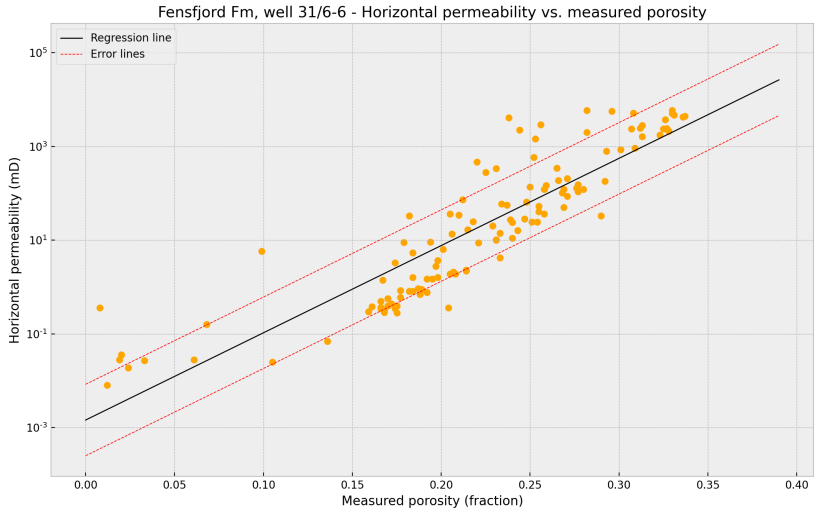

Figure 4.19: Horizontal permeability vs. measured porosity for Fensfjord Fm, best fit line with error. Data points from routine core analysis from well 31/6-6.

Scenario	Expression
High-case	$log(y) = 42.85x_{high} - 4.78$
Mid-case	$log(y) = 42.85x_{mid} - 6.53$
Low-case	$log(y) = 42.85x_{low} - 8.29$

Table 4.14: Porosity-permeability relationship created for Fensfjord Fm extracted from 4.19, with core data from well 31/6-6, where x = porosity volume and y = permeability volume.

4.8.3 Krossfjord Fm

There are also no core plugs and measurements for Krossfjord Fm from well 32/4-1 and 32/2-1. There are four wells that consists of cores from Krossfjord Fm (Oljedirektoratet 2022). No core measurements or poro-perm relationships are, however, found in the public available well documents. As Heather Fm is not interfingering and found between Fensfjord Fm and Krossfjord Fm in well 31/6-6, the poro-perm relationship is believed to follow deeper down for the Krossfjord Fm. Therefore the poro-perm relationship, from well 31/6-6 found for Fensfjord

Fm, is also used for the Krossfjord Fm. Thus the formulas in table 4.14 yield for Krossfjord Fm as well.

4.9 CO_2 storage capacity estimation

The next step in this thesis is to utilize the seismic inverted results quantitatively. With the information and data available it is possible to calculate the CO_2 storage capacity of the studied prospects and formations, based on the inverted porosity volumes from chapter 4.7, seismic mapping done in chapter 4.4 and well data handling in chapter 4.5.1.

There have been different methods demonstrating how to calculate CO_2 storage capacity of aquifers at a regional scale, formations and geological prospect units (Bøe et al. 2002; Bachu et al. 2007; Chadwick et al. 2008; GHG 2009; Vangkilde-Pedersen et al. 2009; Brennan et al. 2010; Gammer et al. 2011; Goodman et al. 2011; Halland et al. 2014; Goodman et al. 2016; Ringrose 2020). In this thesis CO_2 storage capacity estimations are demonstrated first for structural and buoyant trapped CO_2 for the alpha and beta prospects within the Smeaheia CO_2 storage aquifer. Theoretically available pore-space for CO_2 storage capacity is further calculated for the formations Sognefjord, Fensfjord and Krossfjord. This is done to assess the ample potential CO_2 storage capacity potential in the Smeaheia aquifer within the project area. The CO_2 storage capacity equation adapted from Halland et al. (2014) and Ringrose (2020), equation 3.22, is used to calculate the CO_2 storage capacity in the alpha and beta prospects and the formations Sognefjord, Fensfjord and Krossfjord. These CO_2 storage capacity estimations are considered as effective capacity estimations taking into consideration the techno-economic resource-reserve pyramid from Bradshaw et al. (2007), Bachu et al. (2007) and Ringrose (2020). This can be compared to step 2 to in the maturation pyramid from Halland et al. (2014).

Table 4.15 describes the steps taken for the properties to fulfill equation 3.22. The CO_2 storage capacity is estimated in three different scenarios for each prospect and formation. This is based on the low-, mid- and high-case porosity values from the inverted porosity cubes. Furthermore, the low-, mid- and high-cases include ranges for the most uncertain properties being storage efficiency, ε, and the irreducible water saturation, S_{wirr}. Rest of the properties fulfilling equation 3.22 are known from well reports, seismic mapping or well data handling done in this study. These are held constant for the different scenarios, but varies from the different prospect and formation. More details on the assumptions made are in chapters 4.9.1 and 4.9.2.

Details about the general steps taken in the CO_2 storage capacity calculations are presented below:

Step 1, V_b, bulk rock volume: The bulk rock volume is calculated based on the structural constrained trap area multiplied with the column height of the trap. Considering a formation, the area of the formation is multiplied with the formation interval thickness.

Stage	Property	Details
Step 1	V_b, bulk rock volume	Area * thickness
Step 2	ϕ, porosity	low<mid<high
Step 3	N/G, net to gross	Reservoir sands.
Step 4	ρ_{CO_2}, CO_2 density	In-situ P and T conditions.
Step 5	ε, storage efficiency	Aquifer and local scale (low<mid<high)
Step 6	$(1-S_{wirr})$	Max CO_2 saturation (low<mid<high)

Table 4.15: The general steps done in the CO_2 storage capacity calculations to fulfill equation 3.22

Step 2, ϕ, porosity: Low-, mid- and high-case scenario mean porosity values are extracted from the inverted low-, mid- and high-case porosity volumes made in chapter 4.7.

Step 3, N/G, net to gross: CO_2 storage capacity estimations in sandstone formations normally only accounts for storage in the reservoir sandstone intervals and excludes clay and shale fractions (Ringrose 2020). Thus, a net to gross ratio is applied in the CO_2 storage capacity equation.

Step 4, ρ_{CO_2}, CO_2 density: Based on the pressure and temperature regimes, the expected in-situ CO_2 density is included in the equation. With knowing the pressure and temperature values, the CO_2 density can be found (Span and Wagner 1996; Lumley 2019).

Step 5, ε, storage efficiency: Storage efficiency is a complex measure as discussed in 6.1. However, as the project area for the respective prospects and formations lie within the half-open Smeaheia aquifer, some considerations can be taken. Generally storage efficiency is lower at an aquifer scale and higher at a local scale where the geometries and the information about the geological unit is more certain (Bachu 2015). Moreover, the strategy from Chadwick et al. (2008) of distinguishing the storage efficiency between a local and regional scale was done. The prospects were handled on the local scale and the formations on a regional level. Thus two different uncertainty ranges for the storage efficiency for the prospects and the formations were made. The basis for these ranges are made from the "rule of thumb" from Brennan et al. (2010) and Vangkilde-Pedersen et al. (2009) combined with considerations from Goodman et al. (2011), Bachu (2015), Ringrose (2020) and Halland et al. (2014).

Step 6, $(1-S_{wirr})$, max CO_2 saturation at the pore-scale: Ringrose (2020) includes this property in the CO_2 storage capacity. From knowing the irreducible water saturation, an approximate max CO_2 saturation can be estimated and used in the CO_2 storage capacity estimations. Typical values in sandstone formations in saline aquifers can can vary in the range 0.2-0.4 (Ringrose 2020). From the FME

SUCCESS Kaufman and Gasda (2018) report on the Smeaheia aquifer, a connate water value at 0.1 is used. In this thesis it was decided to set an irreducible water saturation range at $0.1 < 0.2 < 0.3$ for both the prospects' and formations' CO_2 storage capacity estimations.

4.9.1 Alpha and beta prospects

Within the Smeaheia aquifer in this thesis' project area, alpha and beta are the two identified structural traps pointed as the main prospects for CO_2 storage, with Sognefjord Fm as the target reservoir (Philips Petroleum Company 1997; Talisman Energy 2008). Table 4.16 entails the inputs for the CO_2 storage capacity estimations for the alpha and beta prospects.

Stage	Alpha	Beta
1: V_b	$18.87km^2(*2)*44.3m$	$27.47km^2*97.3m$
2: ϕ (v/v)	low<mid<high	low<mid<high
3: N/G (M/M)	0.75	0.6
4: ρ_{CO_2} (kg/m^3)	779	816
5: ε (v/v)	0.10<0.15<0.20	0.10<0.15<0.20
6: $(1-S_{wirr})$ (v/v)	0.7<0.8<0.9	0.7<0.8<0.9

Table 4.16: The inputs and steps done in the CO_2 storage capacity calculations for alpha and beta prospect, following the steps in table 4.15.

Further below describes some of the assumptions taken for the CO_2 storage capacity estimations for alpha and beta prospects more in detail, following the steps from table 4.15:

Step 1, V_b, bulk rock volume: The bulk rock volumes for alpha and beta prospects are calculated from the structural trap areas in product with the thickness of the prospect trap column. Polygons are made from the depth structure map for top Sognefjord Fm, with faults and contour lines defining the structural traps for alpha and beta structure, see figure 4.20. A QC of the defined structural traps are done for the prospects from figure 1-2 and 7-2 in the Smeaheia Statoil report (Statoil 2016) and figure 2.1 from the 32/4-1 well report (Philips Petroleum Company 1997). The areas for the structural traps of alpha and beta are calculated in Petrel from the polygons made.

The alpha prospect are defined beyond the GN1101 3D seismic cube where 50% of the structural trap lies outside the GN1101 (Statoil 2016). This is defined further based on the 2D seismic lines. It was chosen for this thesis not to include the 2D seismic data from the SMEAHEIA dataset, as described farther above. However, the area found from the polygon defined above are therefore doubled to get closer to the real alpha prospect area.

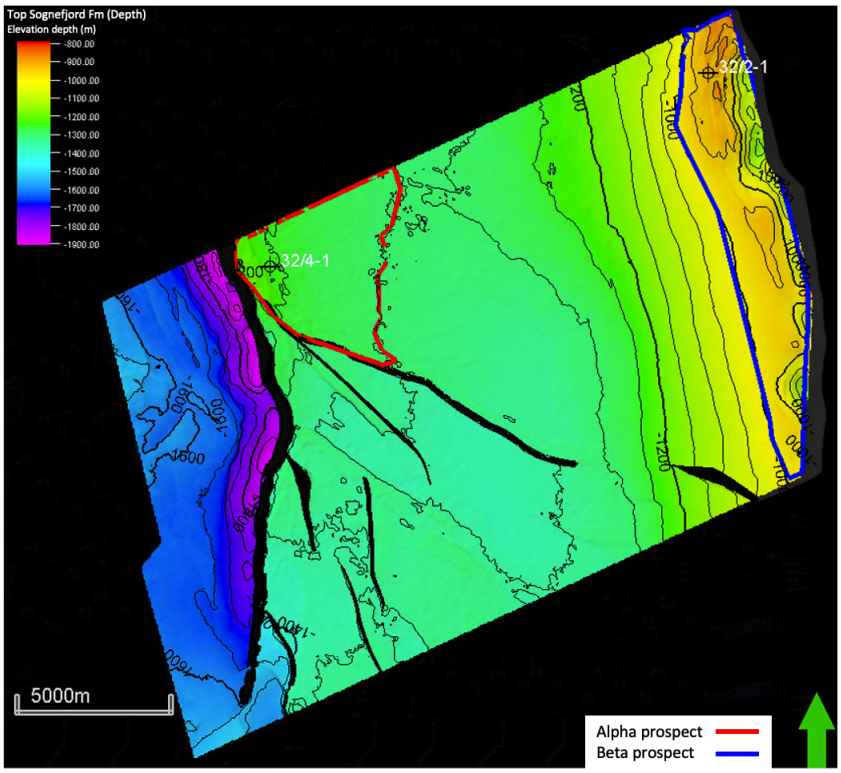

Figure 4.20: Depth structure map for top Sognefjord Fm with the outlined polygons for the alpha and beta prospects area.

Step 2, ϕ, porosity: High, mid and low scenario mean porosity values are extracted from the alpha and beta polygons within the inverted high, mid and low porosity volumes, made in chapter 4.7, for Sognefjord Fm. The surface attribute "Interval average: Maximum" was applied to extract the porosity maps from the inverted porosity volumes. It was decided to be optimistic and utilize the maximum average values within the prospects, as it is reported about higher porosity volumes in the wells 32/4-1 and 32/2-1 for Sognefjord Fm, than other wells penetrating Sognefjord Fm (Statoil 2016; Ross et al. 2013).

Step 3, N/G, net to gross: The net to gross ratio calculated from chapter 4.5.1 for Sognefjord Fm in the wells 32/4-1 and 32/2-1 are used for the alpha and beta prospect, respectively.

Step 4, ρ_{CO_2}, CO_2 density: Based on the pressure and temperature regimes for Sognefjord Fm found from the well reports for well 32/4-1 and 32/2-1, the expected in-situ CO_2 density is decided. The temperature gradient for alpha prospect and well 32/4-1 is found from page 34-35 in 32/4-1 well report (Philips Petroleum Company 1997). The temperature gradient for beta prospect and well 32/2-1 is found on page 48-49 in 32/2-1 well report (Talisman Energy 2008). The pressure

gradient, used for both prospect calculations, is based on pressure points from 32/4-1 and 32/2-1 wells, summed up well in figure 3-5 from Ross et al. (2013, p. 24) Gassnova.

Step 5, ε, storage efficiency: The first assumption taken here is that alpha and beta are known structural prospects at a local scale. Taking into further consideration that Smeaheia is a half-open aquifer in a sedimentary basin and both alpha and beta prospects have good reservoir conditions (based on petrophysical evaluation from chapter 4.5.1), the range $0.10 < 0.15 < 0.20$ for the storage efficiency was made. The higher end of this range is assumed from the "rule of thumb" (Vangkilde-Pedersen et al. 2009; Brennan et al. 2010) at 20%.

4.9.2 Sognefjord, Fensfjord and Krossfjord Fm

The potential of CO_2 storage capacity for the evaluated formations Sognefjord, Fensfjord and Krossfjord can further be evaluated. Table 4.17 gives the steps and inputs for the CO_2 storage capacity estimations for Sognefjord, Fensfjord and Krossfjord formation.

Stage	Sognefjord	Fensfjord	Krossfjord
1: V_b	$248km^2 * 85m$	$248km^2 * 176m$	$248km^2 * 54m$
2: ϕ (v/v)	low<mid<high	low<mid<high	low<mid<high
3: N/G (M/M)	0.65	0.61	0.48
4: ρ_{CO_2} (kg/m^3)	763	746	732
5: ε (v/v)	$0.05 < 0.075 < 0.10$	$0.05 < 0.075 < 0.10$	$0.05 < 0.075 < 0.10$
6: $(1-S_{wirr})$ (v/v)	0.7<0.8<0.9	0.7<0.8<0.9	0.7<0.8<0.9

Table 4.17: The inputs and steps done in the CO_2 storage capacity calculations for Sognefjord, Fensfjord and Krossfjord Fm, following the steps in table 4.15.

The same approach is followed here as for the CO_2 storage capacity estimations for alpha and beta prospects, but more descriptive details following the steps from table 4.15 for Sognefjord, Fensfjord and Krossfjord formation are described below:

Step 1, V_b, bulk rock volume: The bulk rock volumes for the different formations are calculated from the polygon made to outline the Smeaheia storage structure laterally restricted by the Øygarden and Vette fault. The average thicknesses of the formations were calculated from the thickness maps made in chapter 4.4.

Step 2, ϕ, porosity: High-, mid- and low-case scenario mean porosity values are extracted from the inverted high, mid and low porosity volumes for Sognefjord, Fensfjord and Krossfjord Fm made in chapter 4.7. It was chosen to be rather conservative and extract the mean porosity values from the maps made with the surface attribute "Average magnitude". This is done to asses the variation of the values from the whole formation.

Step 3, N/G, net to gross: The net to gross average values calculated from chapter 4.5.1 for the wells 32/4-1 and 32/2-1 are used for the different formations.

Step 4, ρ_{CO_2}, CO_2 density: The average temperature gradient from well 32/4-1 (Philips Petroleum Company 1997, p. 34-35, 59) and 32/2-1 (Talisman Energy 2008, p. 48-49) are used to find the temperature values for Sognefjord, Fensfjord and Krossfjord Fm. The same pressure gradient was used as for the prospect calculations, and further specified for the specific formations average depth.

Step 5, ε, storage efficiency: It is here assumed to consider the formations at a larger aquifer scale. Thus, the storage efficiency is expected ta have lower values (Bachu 2015) and the range was set to $0.05 < 0.075 < 0.10$. From Halland et al. (2014) a storage efficiency for the Sognefjord Delta East was set to 5.5%. The lowest range was thus set to 5% or 0.05. In combination with the rather higher estimates from the "rule of thumb" (Brennan et al. 2010) compared to Goodman et al. (2011), the highest range was chosen to be 0.10 for this thesis studying the formations at an aquifer scale.

4.10 CO_2 injectivity estimation

There are different approaches for evaluating CO_2 injectivity with considering a CO_2 injectivity index or a CO_2 injectivity kh-estimate (Miri and Hellevang 2018; Ringrose 2020; Statoil 2016; Valluri et al. 2021; Valle et al. 2020). We define CO_2 injectivity in terms of the kh-estimate, which is the permeability multiplied with the reservoir thickness (3.23). An accurate design of the CO_2 injectivity process is complex, but some important factors affecting CO_2 injectivity in a CO_2 storage project are (Miri and Hellevang 2018; Ringrose 2020):

- Pressure regimes in the wellbore and formation.
- Well design, placement, well angle.
- Caprock and reservoir formation characteristics.
- Fluid properties.
- Planned and possible CO_2 supply.
- Effects of nearby petroleum provinces and regional aquifers.

The injectivity index tries to put some of this properties into a describing equation, as presented in equation 3.24. A more thorough description of the elements coming into play in the CO_2 injectivity index is well described in figure 4.21 (Miri and Hellevang 2018):

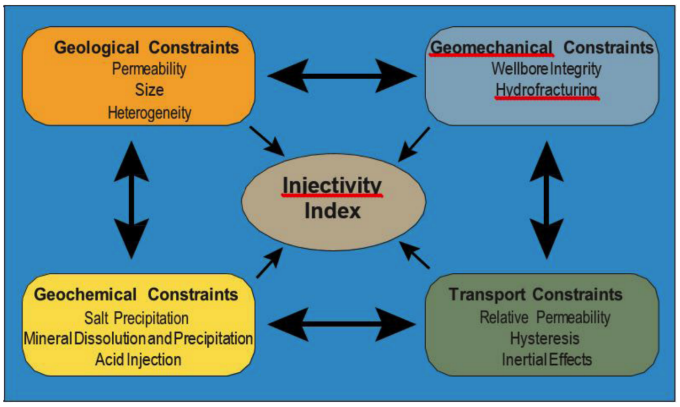

Figure 4.21: Some of the different properties affecting the CO_2 storage injectivity. Figure courtesy of Miri and Hellevang (2018)(p.13).

The kh-estimate (equation 3.23) is also often used to describe CO_2 injectivity (Miri and Hellevang 2018; Halland et al. 2014; Ringrose 2020; Valluri et al. 2021). As it is an estimate of the factors permeability-thickness it can be defined with the units darcy-meter Dm (Statoil 2016) or millidarcy-feet $mD-ft$ (Valluri et al. 2021). In this thesis the kh-estimate is phrased. The kh-estimate may be an oversimplified approach of the complex CO_2 injectivity process, however as the kh-estimate is directly proportional to the CO_2 injectivity index equation 3.24 (Miri and Hellevang 2018; Ringrose 2020), it is descriptive and decisive for the

CO_2 injectivity estimation.

For this thesis it was chosen to evaluate the CO_2 injectivity kh-estimate of the alpha and beta prospect, but also the studied formations Sognefjord, Fensfjord and Krossfjord as a whole. This is done as it might be preferable to inject in the lower lying sediments to utilize the fully CO_2 storage capacity potential in the Smeaheia aquifer (Ross et al. 2013; Fawad et al. 2021). Equation 3.23 is thus used and table 4.18 describes the steps and assumptions taken.

Stage	Property	Details
Step 1	k, permeability	low<mid<high.
Step 2	h, reservoir thickness	Average reservoir thickness.
Step 3	N/G, net to gross	Reservoir sands.

Table 4.18: The general steps done in the CO_2 injectivity kh-estimate calculations to fulfill equation 3.23

Below are more descriptive of the steps taken in the CO_2 kh-estimate of the alpha and beta prospects and Sognefjord Fm, Fensjorf Fm and Krossfjord Fm:

Step 1, k, permeability: The low-, mid- and high-case approach is used for covering different scenarios. Thus the mean permeability values are extracted from the inverted low-, mid- and high-case scenario permeability cubes, done in chapter 4.8, focused on the respective prospect and formation.

Step 2, h, reservoir thickness: The mean prospect thickness of alpha and beta prospects are used, as well as the average formation thickness of Sognefjord, Fensfjord and Krossfjord Fm. These values are extracted from the thickness maps made in chapter 4.4.

Step 3, N/G, net to gross ratio: The same approach used for the prospects alpha and beta in chapter 4.9.1 and for the formations in chapter 4.9.2 is used for the N/G here.

4.11 Traffic-light evaluation

Many authors have tried to characterize, rank and indicate suitable CO_2 storage aquifers and formations and implement that in workflows (Bachu et al. 2007; Chadwick et al. 2008; Halland et al. 2014; Riis and Halland 2014; K. Anthonsen et al. 2014; Hjelm et al. 2020; Lloyd et al. 2021). This is a crucial part of the development of standards in the CCS and CO_2 storage industry, as this defines how to securely find the right area, formations and prospect to store CO_2.

In this thesis the CO_2 storage resources capacity and injectivity is the focus on evaluating a CO_2 storage formation, thus the sealing properties and containment are not considered. It is attempted to use a traffic-light approach and utilize the seismic quantitative results. First, the porosity and permeability results are evaluated for the CO_2 storage capacity and injectivity estimations. Second the inverted permeability maps are generated into CO_2 traffic-light injectivity maps based on the lateral kh-estimate for a specific formation, and the traffic-light thresholds.

In this thesis the thresholds for the reservoir parameters porosity, permeability and reservoir thickness are applied from Halland et al. (2014). Porosity and permeability are of the most heavy weighted parameters when evaluating CO_2 storage capacity and injectivity Halland et al. (2014, p. 23). Porosity and permeability are thus the building parameters for the creation of this thesis' traffic-light approach. Table 4.19 entails thus the indicators for defining a red, yellow or green light for a CO_2 storage formation or prospect assumed in this study.

Property	**Red**	**Yellow**	**Green**
Porosity (ϕ)	$< 15\%$	$15\% < x < 25\%$	$> 25\%$
Permeability (k)	$< 10mD$	$10mD < x < 500mD$	$> 500mD$
Reservoir thickness	$< 15m$	$15m < x < 50m$	$> 50m$
kh-estimate	$< 0.15Dm$	$0.15Dm < x < 25Dm$	$> 25Dm$

Table 4.19: The property indications defining the traffic-light approach for evaluating a CO_2 storage formation in this study. Adapted and modified from Halland et al. (2014, p.23).

The kh-estimate thresholds are the product of the permeability thresholds and reservoir thickness thresholds and defined in Darcy-meter (Dm).

4.11.1 Traffic-light injectivity maps

The kh-estimate can be used as an easy, but useful tool to describe CO_2 injectivity of a formation (Valluri et al. 2021). The CO_2 injectivity kh-estimates from chapter 4.10 gives an approximate average evaluation of that prospect' or formations' CO_2 injectivity characteristics. However, when evaluating a specific formation for CO_2 injection it is even more valuable to know the lateral distribution of the injectivity

and where in the formation injectivity can be suitable. Thus, in addition with knowing the permeability distribution for a formation, the reservoir thickness map provides the additional valuable information. With utilizing the traffic-light kh-estimate thresholds from table 4.19, traffic-light injectivity maps can be made. Table 4.20 describes the step done to generate the traffic-light injectivity maps.

Stage	**Property**	**Details**
Step 1	k, permeability maps	low<mid<high.
Step 2	h, thickness maps	Made in chapter 4.4.
Step 3	N/G, net to gross	Reservoir sands.
Step 4	Generate the maps	Petrel calculator

Table 4.20: The general steps done to generate the traffic-light injectiviy maps

As seen, the creation of the traffic-light injectivity maps follows the same approach as table 4.18, based on equation 3.23, but details on the steps here are described below:

Step 1, permeability maps: The low-, mid- and high-case inverted permeability volumes are utilized and being the first product in equation 3.23.

Step 2, thickness maps: The thickness maps for the specific formation, based on the depth model made in chapter 4.4, are further used.

Step 3, N/G: The N/G is added to the equation, in the same approach as step 3 in table 4.18. The average net to gross ratio for the specific formation is added to the equation.

Step 4, generate the traffic-light injectivity maps: The calculator in Petrel is used to generate the traffic-light injectivity maps, multiplying the permeability and thickness maps and the N/G, following equation 3.23. The mid-case traffic-light injectivity maps are found in the results.

Chapter 5

Results

In this chapter the results of this study are presented. The results are presented in a sequential order - taking the reader through the seismic quantitative method demonstrated in this thesis to study the Smeaheia CO_2 storage area for CO_2 storage resource estimation:

- Acoustic impedance volumes presented in chapter 5.1.
- Porosity volumes and extracted porosity values presented in chapter 5.2.
- Permeability volumes and extracted permeability values in chapter 5.3.
- **Main result 1:** CO_2 storage capacity estimations presented in chapter 5.4.
- **Main result 2:** CO_2 injectivity estimations presented in chapter 5.5.
- **Main result 3:** Traffic-light injectivity maps presented in chapter 5.6.
- Traffic-light evaluation of the prospects and formations presented in 5.7.

As listed, the main results are those presented in chapter 5.4, 5.5 and 5.6. However, the results in chapter 5.1, 5.2 and 5.3 are important because these are results on the way being highly decisive for the main results. This is discussed more in chapter 6. Chapter 5.7 sums everything up, utilizing the seismic quantitative results and the traffic-light approach in this study.

5.1 Seismic inverted acoustic impedance volume

The result from the process described in chapter 4.6 results in a 3D acoustic impedance volume. The background model with the modelled synthetic P-impedance traces and the resulting seismic inverted impedance volume are first shown from Geoview:

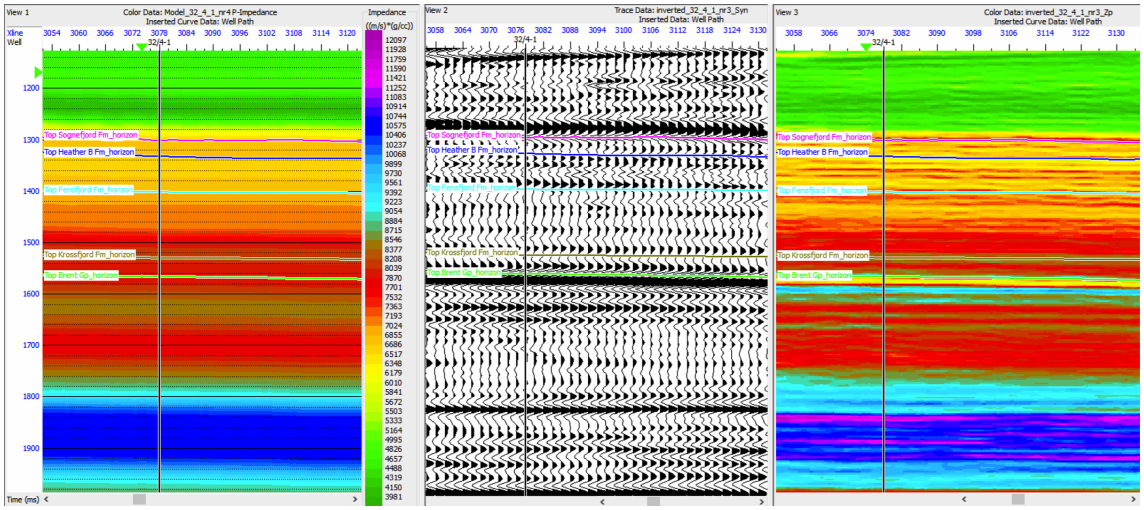

Figure 5.1: Cross-sections of the the background model to the left in view 1, the modelled synthetic p-impedance traces in view 2 and the resulting acoustic impedance volume in view 3. The views are displayed in inline 1026 with the penetrating well 32/4-1.

It is observed from figure 5.1 with the low-frequency background model to the left, that the acoustic impedance increases with depth. Applying the modelled synthetic P-impedance traces we see a strong amplitudes defining the top and base of the Smeaheia reservoir interval, for top Sognefjord Fm and top Brent Gp, respectively. This results in the end acoustic impedance volume to the right in 5.1 and one can see more locally variations within the formation intervals.

The inverted acoustic impedance volume from Geoview is further imported into Petrel. An inline from this cube, focused on the interval of interest, is shown in figure 5.2. Figure 5.2 clarifies the inverted acoustic impedance volume from 5.1 with the impedance variation horizontally and vertically.

The acoustic impedance volume in Petrel is further extracted for the intervals of the studied formations Sognefjord, Fensfjord and Krossfjord Fm:

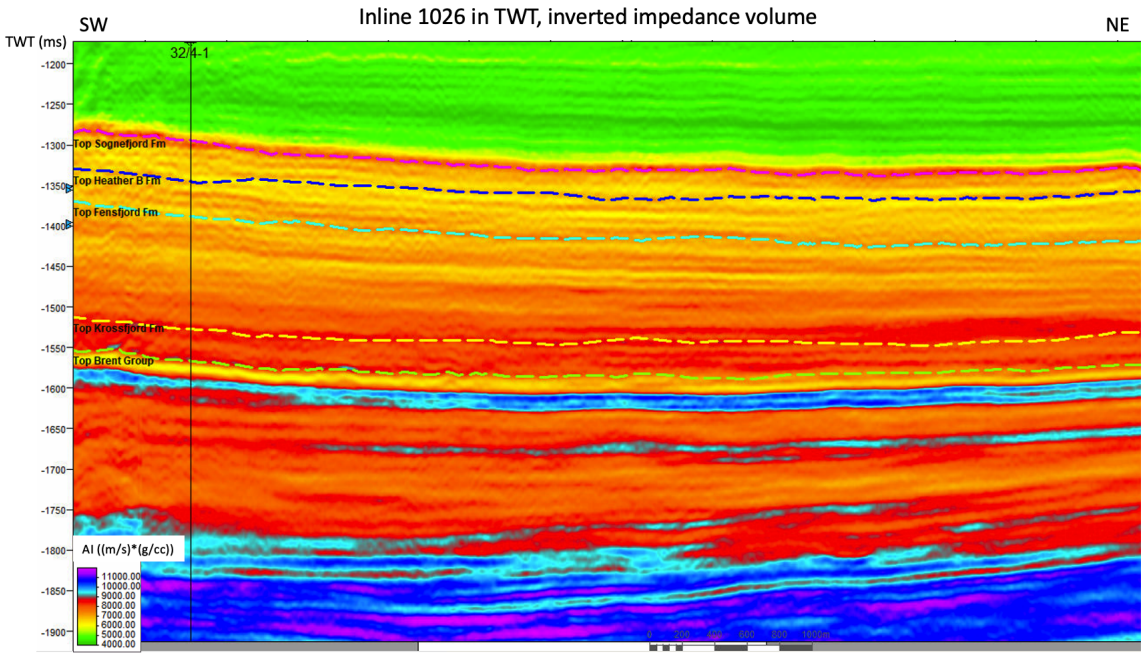

Figure 5.2: Cross-section of the inverted P-impedance volume imported into Petrel from inline 1026 with the penetrating well 32/4-1 and the interpreted horizons. The scale

5.1.1 Sognefjord formation:

The first evaluated formation to extract acoustic impedance values from is the Sognefjord Fm. From the acoustic impedance volume map for Sognefjord Fm in figure 5.3, it can be seen that the acoustic impedance decreases going from the Vette fault, defining the boundary in the SW, to the Øygarden fault complex, being the boundary in the NE. Observing the contour lines, the acoustic impedance shows lower values following the deeper lying Sognefjord Fm in the west, near well 32/4-1, to the more shallow Sognefjord Fm in the east, near well 32/2-1.

5.1.2 Fensfjord formation

The acosutic impedance map volume for Fensfjord Fm is further extracted. From figure 5.4, less clear variations in the acosutic impedance values are here observed. However, some decreasement in the acoustic impedance is observed north in the map.

5.1.3 Krossfjord formation

The last formation to be considered in the Smeaheia CO_2 storage complex for this thesis is the Krossfjord Fm, fig. 5.5. Here, clear variations observing from west to the east are noted. A general trend of decreasement in the acoustic impedance,

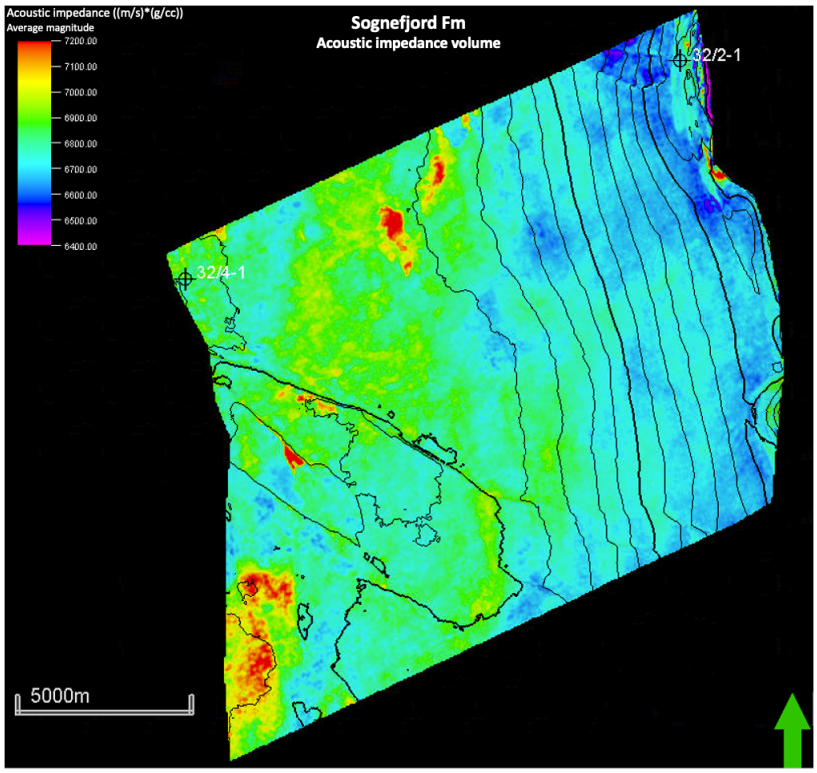

Figure 5.3: Map view of the average magnitude value for Sognefjord Fm interval within the inverted acoustic impedance volume.

going from the deeper Krossfjord Fm in the west, to the shallower Krossfjord in the east, can be seen.

5.2 Porosity volumes

The middle-case estimated inverted porosity volume maps, generated from chapter 4.7, are presented further for Sognefjord Fm, Fensfjord Fm and Krossfjord Fm. The high- and low-case estimated inverted porosity volume maps for all the formations can be found in appendix chapter C. Mean porosity values are further extracted from the porosity volumes for the formations and the alpha and beta prospect, presented in chapter 5.2.4.

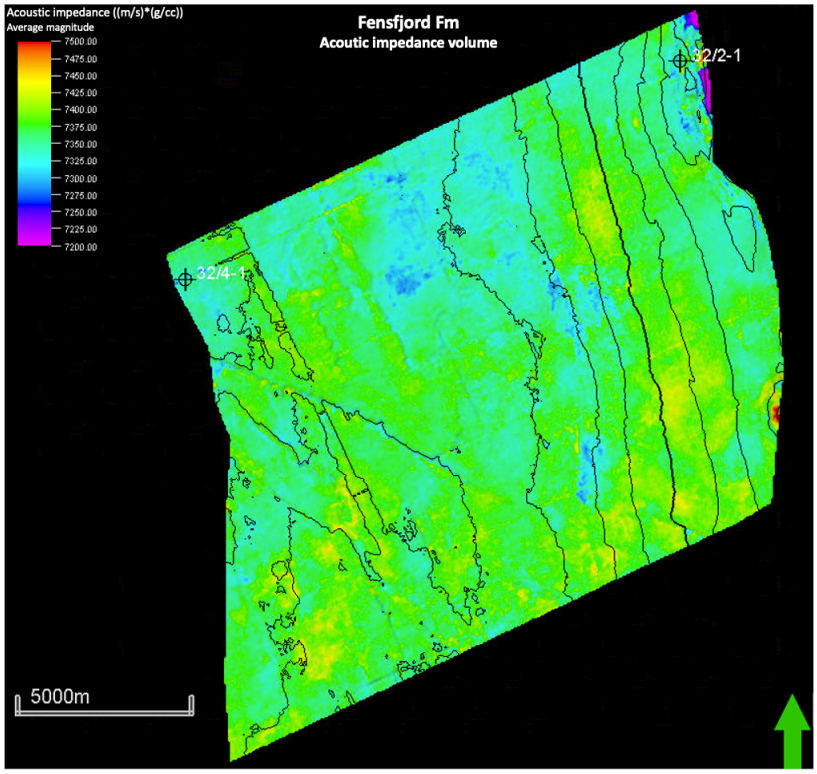

Figure 5.4: Map view of the average magnitude value for Fensfjord Fm interval within the inverted acoustic impedance volume.

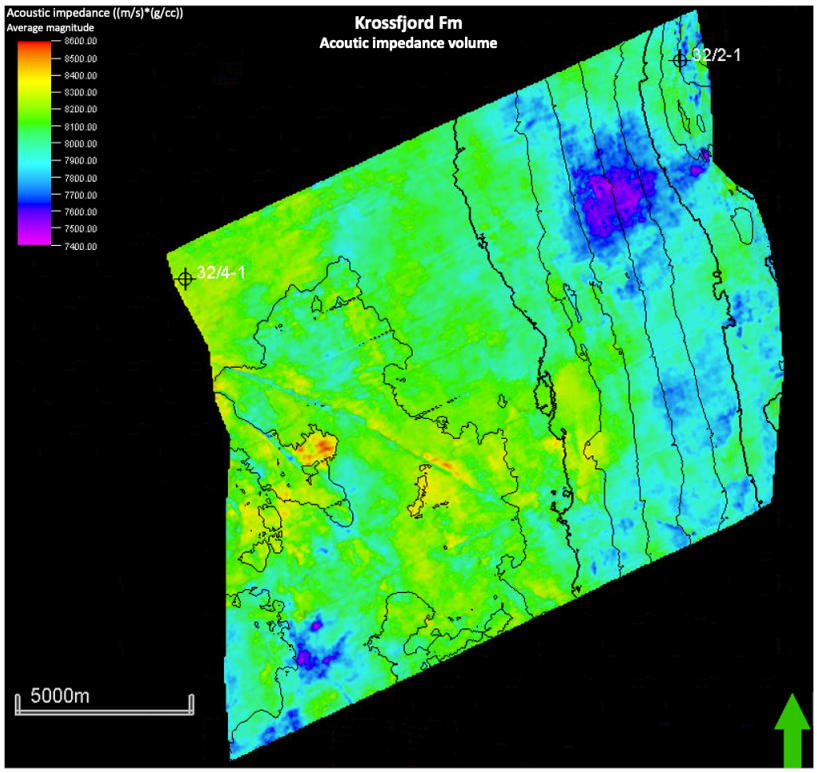

Figure 5.5: Map view of the average magnitude value for Krossfjord Fm interval within the inverted acoustic impedance volume.

5.2.1 Sognefjord formation

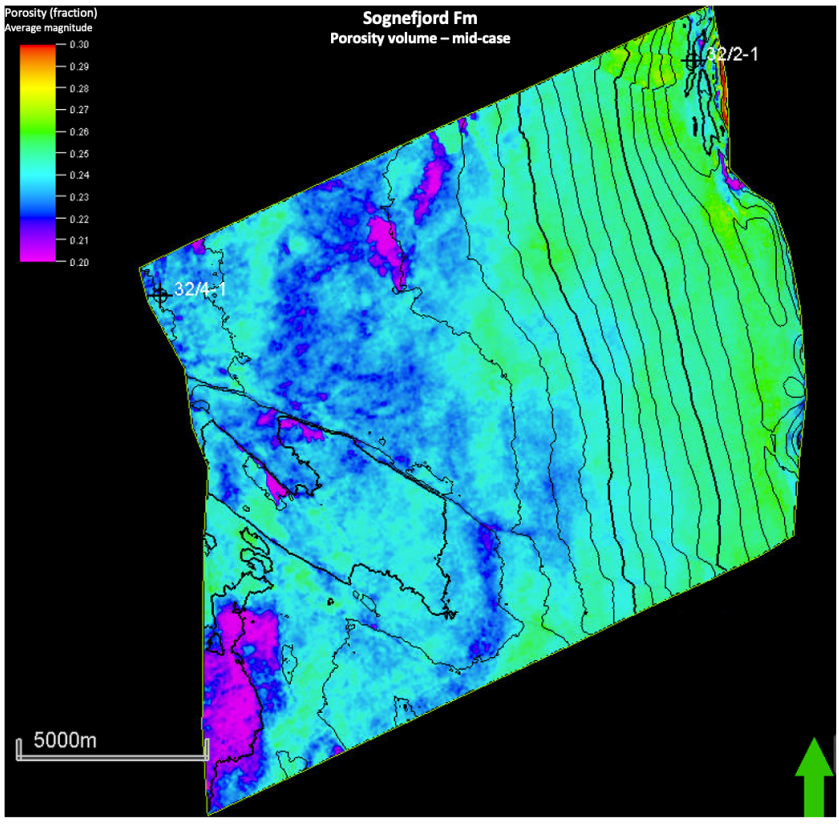

Figure 5.6: Map view of the average magnitude value of porosity for Sognefjord Fm interval within the inverted middle estimated porosity volume.

5.2.2 Fensfjord formation

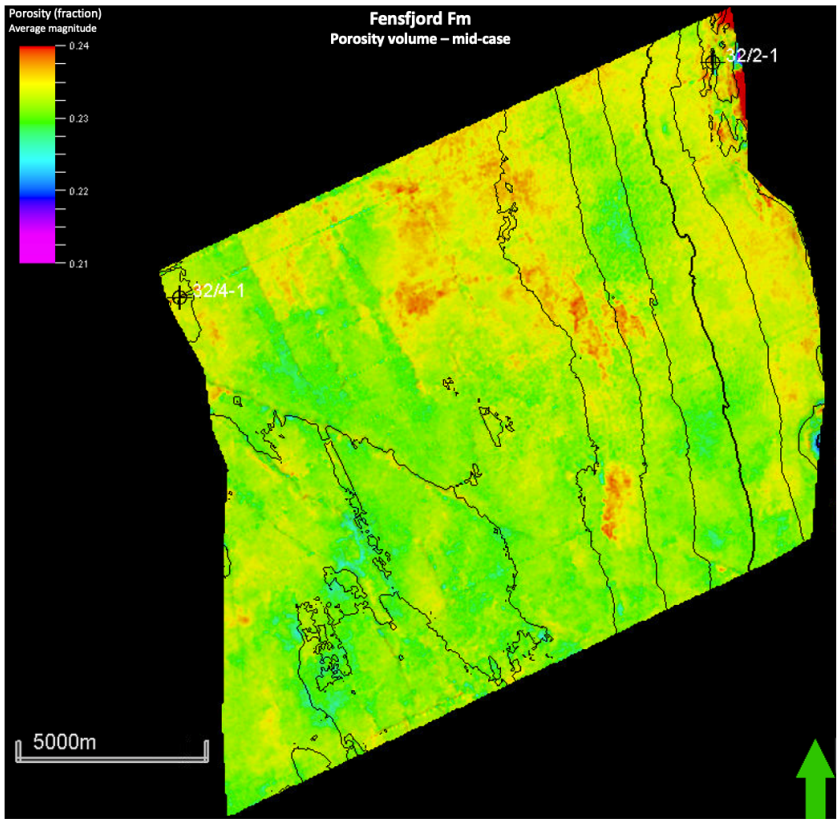

Figure 5.7: Map view of the average magnitude value of porosity for Fensfjord Fm interval within the inverted middle estimated porosity volume.

5.2.3 Krossfjord formation

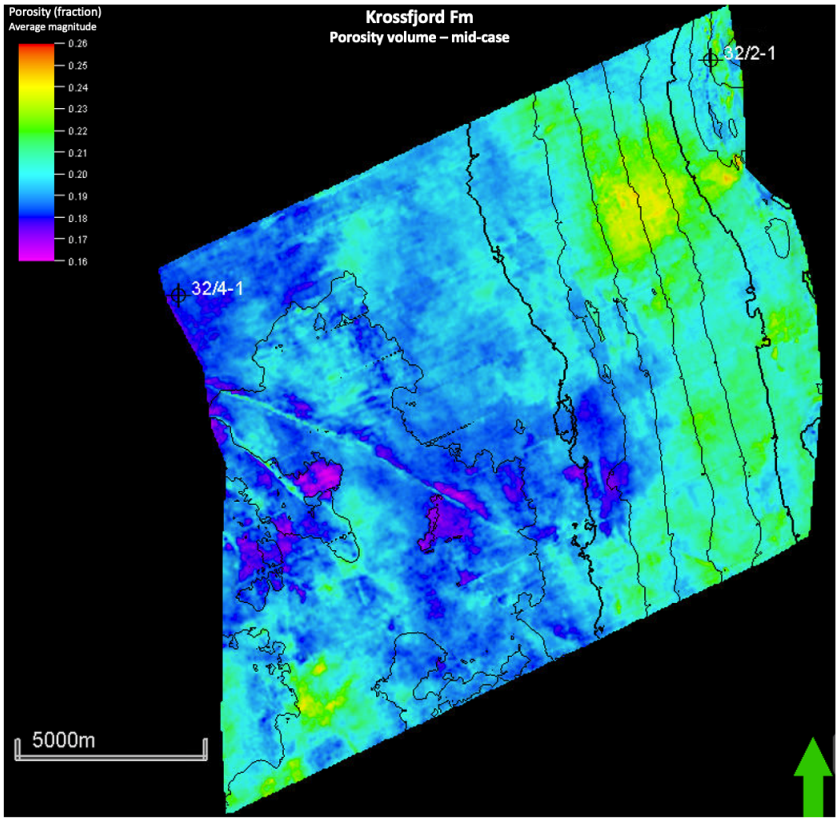

Figure 5.8: Map view of the average magnitude value of porosity for Krossfjord Fm interval within the inverted middle estimated porosity volume.

5.2.4 Porosity values extracted from the inverted porosity volumes

Scenario	Alpha prospect	Beta prospect
High-case (v/v)	0.36	0.39
Mid-case (v/v)	0.34	0.37
Low-case (v/v)	0.32	0.34

Table 5.1: Mean porosity values from the seismic inverted porosity volumes for the low-, mid- and high-case scenarios for alpha and beta prospects.

5.3 Permeability volumes

The mid-case estimated inverted permeability volume maps, from chapter 4.8, are presented in figures (5.9, 5.10, 5.11) for Sognefjord Fm, Fensfjord Fm and Krossfjord Fm. The high- and low-case estimated inverted permeability volume maps

Scenario	Sognefjord Fm	Fensfjord Fm	Krossfjord Fm
High-case (v/v)	0.26	0.26	0.22
Mid-case (v/v)	0.24	0.23	0.20
Low-case (v/v)	0.22	0.21	0.17

Table 5.2: Mean porosity values from the seismic inverted porosity volumes for the low-, mid- and high-case scenarios for Sognefjord, Fensfjord and Krossfjord Fm.

for Sognefjord, Fensfjord and Krossfjord Fm can be found in appendix chapter D. The extracted mean permeability values are further presented in chapter 5.3.4.

5.3.1 Sognefjord formation

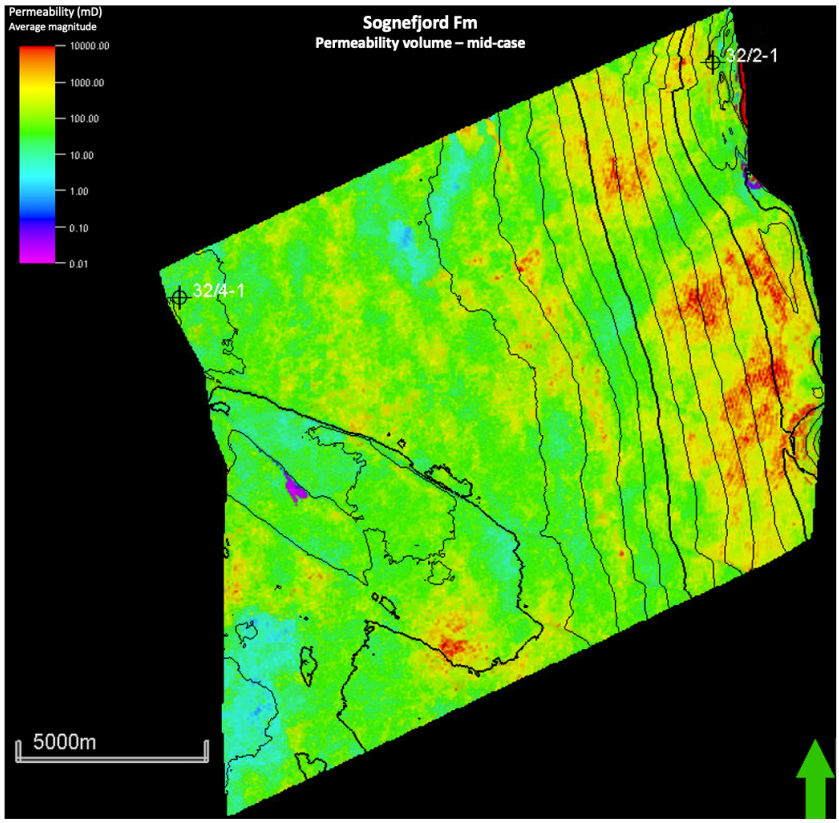

Figure 5.9: Map view of the average magnitude value of permeability for Sognefjord Fm interval within the inverted middle estimated permeability volume.

5.3.2 Fensfjord formation

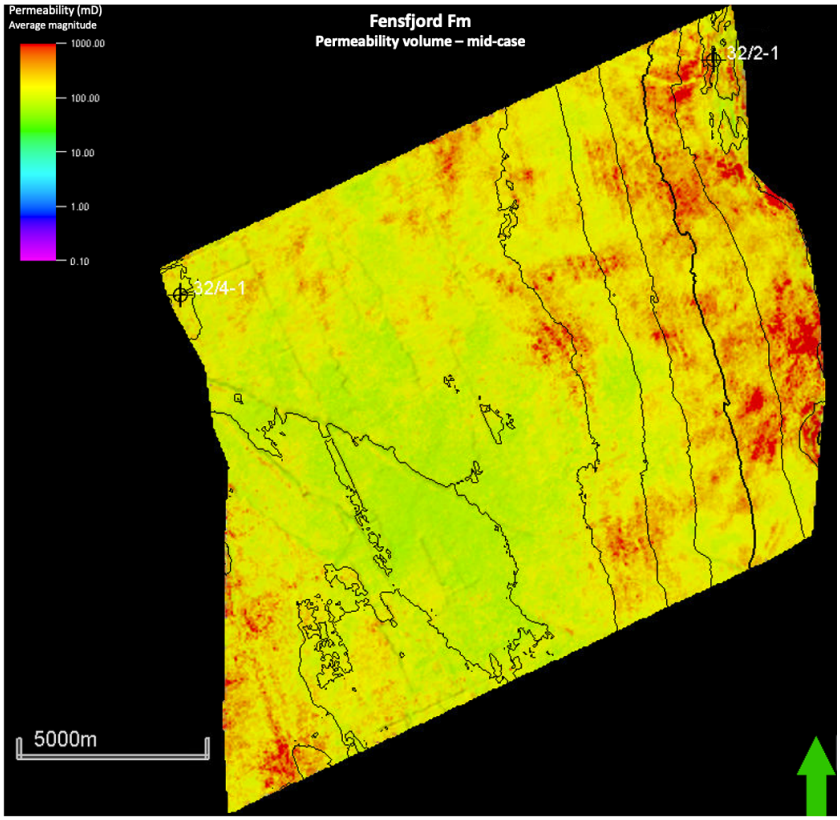

Figure 5.10: Map view of the average magnitude value of permeability for Fensfjord Fm interval within the inverted middle estimated permeability volume.

5.3.3 Krossfjord formation

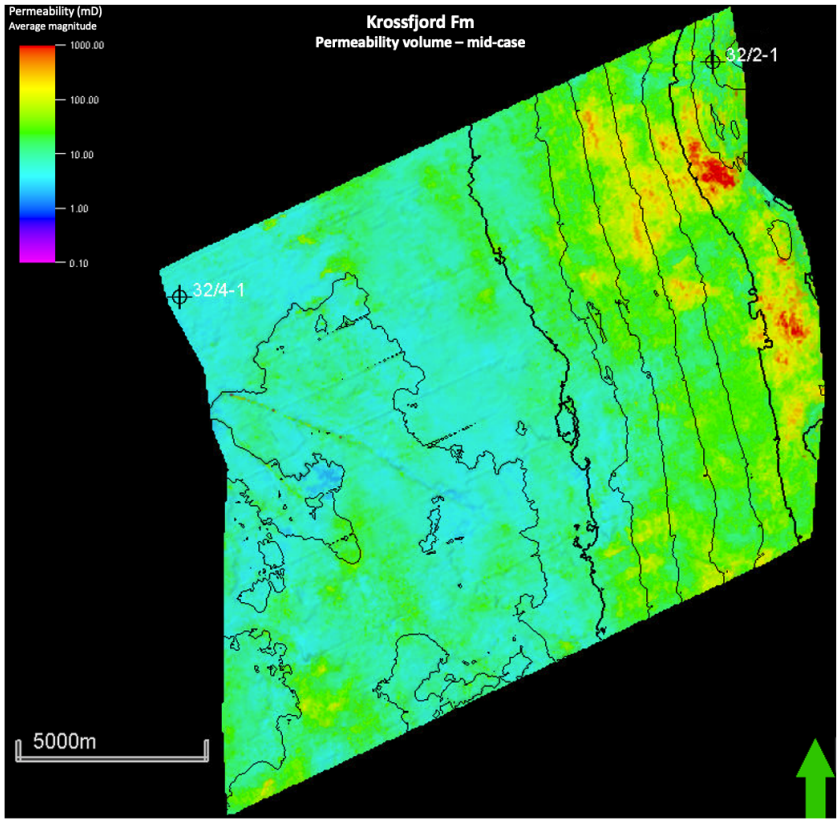

Figure 5.11: Map view of the average magnitude value of permeability for Krossfjord Fm interval within the inverted middle estimated permeability volume.

5.3.4 Permeability values extracted from the inverted permeability volumes

Scenario	Alpha prospect	Beta prospect
High-case (mD)	6923.78	29431.06
Mid-case (mD)	998.99	4246.46
Low-case (mD)	144.14	378.24

Table 5.3: Mean permeability values from the seismic inverted permeability volumes for the low-, mid- and high-case scenarios for alpha and beta prospects.

Scenario	Sognefjord Fm	Fensfjord Fm	Krossfjord Fm
High-case (mD)	4908.68	3426.41	583.62
Mid-case (mD)	658.37	214.49	31.42
Low-case (mD)	88.30	13.43	1.69

Table 5.4: Mean permeability values from the inverted permeability volumes for the low-, mid- and high-case scenarios for Sognefjord, Fensfjord and Krossfjord Fm.

5.4 Main result 1: CO_2 storage capacity

The CO_2 storage capacity estimations constitutes the first part of the main results. The seismic quantitative method demonstrated in this study outputs porosity volumes for the studied prospects and formations making up the Smeaheia CO_2 storage complex. Porosity act as one of the most weighted inputs (Riis and Halland 2014) for the structural CO_2 storage capacity equation and method used in this study, modified from Ringrose (2020) and Halland et al. (2011). In combination with the extracted mean porosity values from chapter 5.2.4, the uncertainty ranges and further inputs, as from chapter 4.9, the CO_2 storage capacity estimations resulted in table 5.5 and 5.6, for the prospects and formations, respectively.

Scenario	Alpha prospect	Beta prospect	Smeaheia prospect total
High-case (Mt)	63.31	91.87	155.18
Mid-case (Mt)	39.86	58.11	97.97
Low-case (Mt)	21.89	31.15	53.04

Table 5.5: CO_2 storage capacity estimations for high-, mid- and low-case Alpha and beta prospects, with the potential total CO_2 storage capacity with the evaluated Smeaheia prospects.

Alpha prospect has CO_2 storage capacity estimations at 63.31, 39.86 and 21.89Mt, for the high-, mid- and low-case scenarios, respectively. The beta prospect has a storage capacity of 91.87, 58.11 and 31.15Mt. Considering adding the capacities of the prospects, the lowest estimate adds up to 53.04Mt.

Scenario	Sognefjord	Fensfjord	Krossfjord	Smeaheia total
High-case (Mt)	254.88	465.23	93.53	813.64
Mid-case (Mt)	156.85	274.37	56.68	487.90
Low-case (Mt)	83.87	146.13	28.11	258.11

Table 5.6: CO_2 storage capacity estimations for high-, mid- and low-case Sognefjord Fm, Fensfjord Fm and Krossfjord Fm, with the potential total CO_2 storage capacity of the Smeaheia formations.

From table 5.6 it can be observed that Sognefjord Fm has estimated CO_2 storage capacities at 254.88, 156.85 and 83.87Mt for the high-, mid- and low-case scenarios, respectively. Fensfjord Fm shows the highest estimations for all the three uncertainty scenarios, reaching 465.23Mt for the high-case scenario. The lowest estimates for the CO_2 storage capacity are found in Krossfjord Fm having a potential of storing 28.11-93.53Mt in the low- to high-case scenario, respectively.

5.5 Main result 2: CO_2 storage injectivity

With the extracted mean permeability values from chapter 5.3.4 and the process done in table 4.18, the CO_2 storage injectivity kh-estimate is calculated for the alpha and beta prospects and Sognefjord, Fensfjord and Krossfjord formations.

Scenario	Alpha prospect	Beta prospect
High-case (Dm)	230.09	1718.36
Mid-case (Dm)	33.20	247.93
Low-case (Dm)	4.79	22.08

Table 5.7: CO_2 storage injectivity kh-estimations for high-, mid- and low-case Alpha and beta prospects.

Scenario	Sognefjord Fm	Fensfjord Fm	Krossfjord Fm
High-case (Dm)	282.56	368.21	15.16
Mid-case (Dm)	37.90	23.05	0.82
Low-case (Dm)	5.08	1.44	0.04

Table 5.8: CO_2 storage injectivity kh-estimations for high-, mid- and low-case Sognefjord Fm, Fensfjord Fm and Krossfjord Fm.

5.6 Main result 3: Traffic-light injectivity maps

Taking into consideration table 4.19 and 4.20, the traffic-light injectivity maps for the studied formations are produced. The mid-case traffic-light injectivity maps are shown in figures 5.13, 5.13, 5.14.

5.6.1 Sognefjord Fm

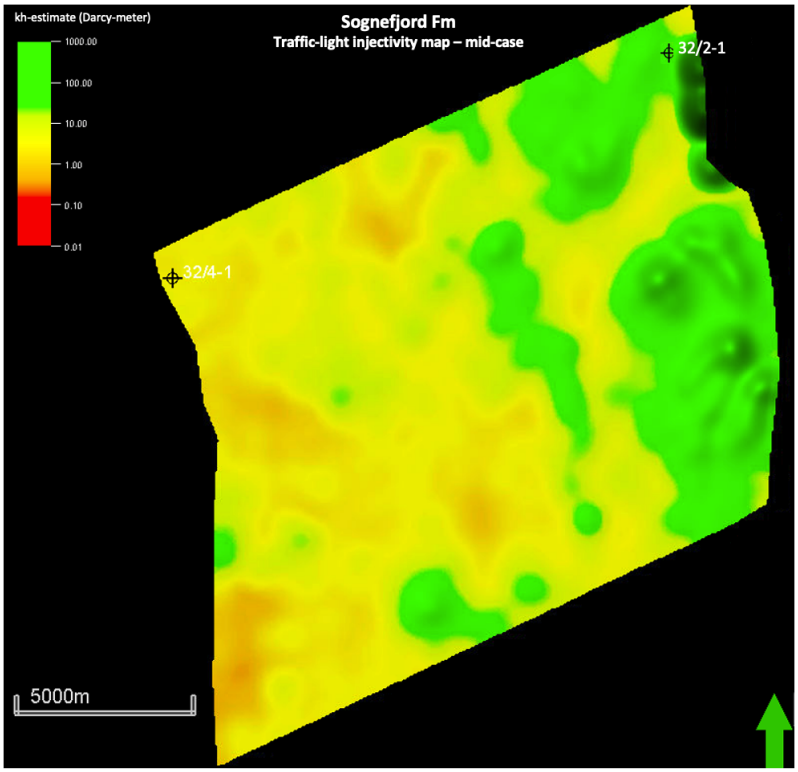

Figure 5.12: Map view of the CO_2 injectivity *kh*-estimate for Sognefjord Fm.

Observing the traffic-light injectivity map for Sognefjord Fm (fig. 5.12), the "green light" areas are in the SE and NE of the map. It is observed a clear traffic-light difference with a yellow and green area, for the 32/4-1 and 32/2-1 well, respectively.

5.6.2 Fensfjord Fm

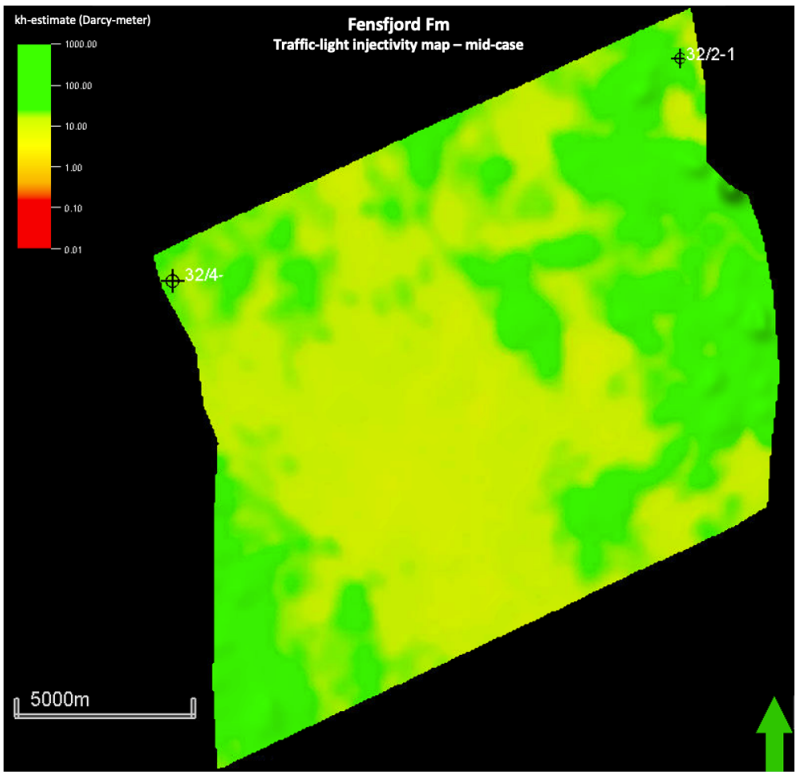

Figure 5.13: Map view of the CO_2 injectivity *kh*-estimate for Fensfjord Fm.

The traffic-light injectivity map for Fensfjord Fm shows green areas throughout in the west and east of the map, however with some differing yellow areas in the middle.

5.6.3 Krossfjord Fm

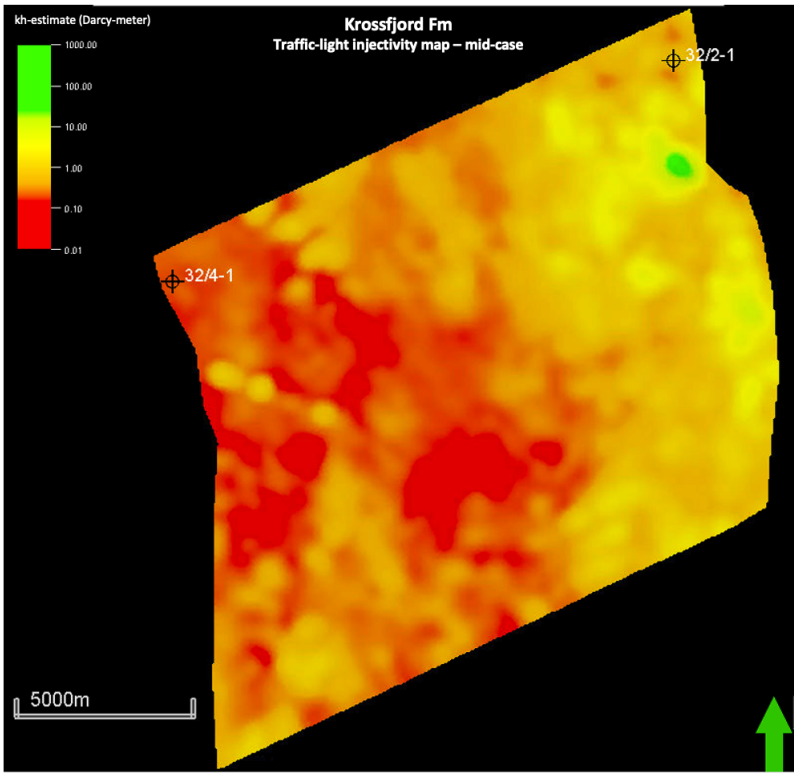

Figure 5.14: Map view of the CO_2 injectivity *kh*-estimate for Krossfjord Fm.

Krossfjord Fm shows middle *kh*-estimate trend in the east, but aggravates westwards. There are areas in the middle of the map showing strong red lights. One clear green spot is observed in the NE, closer to well 32/2-1 and some yellow areas around.

5.7 Traffic-light evaluation of the prospects and formations

Applying the traffic-light approach, from table 4.19, all the formations and prospects are evaluated within the thresholds set and given a traffic-light. Table 5.9 visualizes this. Of the mid-case prospects, beta scores the highest in all metrics. Of the mid-case formations, Sognefjord scores the highest in all but one metric, capacity, which Fensfjord does. On the other hand, Krossfjord scores lowest by a wide margin on all metrics.

Formation/prospect	$\phi(v/v)$	$k(mD)$)	$kh-estimate(Dm)$)	**Capacity** (Mt)
Alpha high	0.36	6923.78	230.09	63.21
Alpha mid	0.34	998.99	33.20	39.86
Alpha low	0.32	144.14	4.79	21.89
Beta high	0.39	29431.06	1718.36	91.87
Beta mid	0.37	4246.46	247.93	58.11
Beta low	0.34	378.24	22.08	31.15
Sognefjord high	0.26	4908.68	282.56	254.88
Sognefjord mid	0.24	658.37	37.90	156.85
Sognefjord low	0.22	88.30	5.08	83.87
Fensfjord high	0.26	3426.41	368.21	465.23
Fensfjord mid	0.23	214.49	23.05	247.37
Fensfjord low	0.21	13.43	1.44	146.13
Krossfjord high	0.22	583.62	15.16	93.53
Krossfjord mid	0.20	31.42	0.82	56.68
Krossfjord low	0.17	1.69	0.04	28.11

Table 5.9: All the extracted and estimated CO_2 storage resource properties with defined traffic-light, applied from the traffic-light approach in this study.

Chapter 6

Discussion

This chapter discusses the results from chapter 5, with a focus on the main results. We derived these results from this thesis' workflow and methodology described in chapter 4. This thesis as an attempt to categorize CO_2 storage resources, based on storage capacity, and injectivity (based on the kh-estimate).

The main uncertainties, drawbacks and strengths linked to the main results are discussed and how different approaches and methods could have changed and/or improved the results of this thesis. The most important uncertainties from the sub-results being decisive for the main results are discussed. The main results are thus discussed first:

- **Main result 1:** CO_2 storage capacity estimations, results from chapter 5.4 are discussed in chapter 6.1.
- **Main result 2:** CO_2 injectivity estimations (based on the kh-estimate), results from chapter 5.5 are discussed in chapter 6.2.
- **Main result 3:** Traffic-light injectivity maps, results from chapter 5.6 are discussed in chapter 6.3.

Building on this, there is a further discussion on how the results and methods applied in this study can contribute in the development of seismic quantitative methods for characterizing and studying CO_2 storage projects. Furthermore, as this thesis demonstrates a seismic quantitative workflow with steps and sub-results being reliant on each other — illustrated in figure 4.1 — the end results are dependant on the steps outlined in the workflow.

Thus, the sub-results and steps important to mention and discuss that are contributing most for the ending results, are:

- The seismic inverted acoustic impedance volume: process done in chapter

4.6 and results from chapter 5.1.
- From acoustic impedance volume to porosity volumes: process done in chapter 4.7 and results from chapter 5.2.
- From porosity volumes to permeability volumes: process done in chapter 4.8 and results from chapter 5.3.

6.1 Main result 1: CO_2 storage capacity

The first main results to discuss are the CO_2 storage capacity estimations generated from chapter 4.9. The results for the prospects and formations are first discussed separately and then the most important uncertainties regarding the calculations.

6.1.1 Alpha and beta prospect

Starting with the CO_2 storage capacity estimations for the evaluated prospects, it can be observed from the results in table 5.5, that the beta prospect potentially has a greater CO_2 storage capacity than the alpha prospect. However, based on the seismic quantitative process done in this thesis, both prospects entails ample potential CO_2 storage capacity. Especially the mid- and high-case scenario capacity estimations are promising estimations. Comparing to other CO_2 storage prospects evaluated on the Norwegian continental shelf (Halland et al. 2014; Ane Lothe et al. 2019; Lloyd et al. 2021) confirms the promising storage capacities for alpha and beta prospect. Halland et al. (2014) evaluated prospects on the NCS having estimated storage capacities in the range 21-220Mt, while Ane Lothe et al. (2019) gives a range estimate of 40-3000Mt, evaluating prospects at the Horda Platform.

There can be valuable to discuss what sufficient storage capacities can be. Lloyd et al. (2021) deals with a cut-off for suitable storage capacities for prospects within the regional Utsira aquifer at $>5Mt$. Thus, based on these considerations, all the uncertainty scenarios capacity calculations done in this study for alpha and beta prospect can be evaluated as sufficient storage capacities. On the other hand, Statoil (2016) mention sufficient values for storage capacities of alpha and beta prospects being more than $33Mt$. From this, the mid- and high-case scenarios for the prospects can be defined as sufficient capacities. Sufficient storage capacities is however a complex discussion because every storage projects' most suitable capacity has to be accurately planned with a holistic value-chain planning of the eventual CCS project. Two indicators can be the amount of the planned CO_2 captured and the planned project lifetime to become economical viable. These factors are very project and site-specific. However typical planned lifetime of integrated CCS and CO_2 storage projects can be 25-30 years (Gassnova Lonsghip rapport; Longship whitepaper; Danmark markedsrapport). Moreover, typical planned capture- and injection-rates are in the range 0,5-3 $Mtpa$, on average (IOGP 2022, Global CCS Institute database). Thus only the low-case scenario for the alpha prospect

might not meet up to these criteria. However, more important factors that are decisive for the sufficient storage capacities are pressure management and possible injection rate, more discussed below.

As observed from table 4.16, the substantial thicker reservoir column for the beta prospect is the first main factor why the storage capacity is higher. The thickness of Sognefjord Fm thickens out from the alpha prospect in the SW to the beta prospect in the NE, with the deeper lying Heather B Fm pinching out.

Furthermore the 2-3% higher mean porosity values for all the three uncertainty scenarios (table 5.5), is the second main reason. Looking at the porosity map for Sognefjord Fm, 5.6, the porosity increases going from SW to the NE in the studied area. Thus, generally higher porosity values are observed in the beta prospect area NE, than the alpha prospect SW. This corresponds to the acoustic impedance map, figure 5.3, as expected, whereas the acoustic impedance decreases from SW to NE and hence we observe the generality that the acoustic impedance increases with decreasing porosity (Z. Wang 2001). However, uncertainties on this trend are further discussed below in chapter 6.1.3.

As the alpha and beta prospects in the Smeaheia area are well studied, it is natural to compare our results with other papers also estimating the storage capacities. The Statoil study on Smeaheia CO_2 storage area evaluated both the alpha and beta prospects (Statoil 2016) and calculated the structural storage capacity of the prospects. The CO_2 storage capacity estimations are suggested to be in the range from 82.7-117 Mt and 87.8-124 Mt, for the alpha and beta prospect, respectively. This thesis' results correspond well in the trend of higher general storage capacity for the beta prospect, however, with clear lower estimated ranges. In Statoil (2016) a storage efficiency coefficient is not applied to the storage capacity estimations for the prospects. This make the comparisons less valid and tell about factors in cancelling each other out when comparisons are matched with this thesis' and Statoil (2016) estimations.

Ane Lothe et al. (2019) studied the alpha prospect as well as the gamma prospect farther south in the Smeaheia area. It is here suggested storage capacities for the alpha prospect from 40-50 Mt. Lauritsen et al. (2018) suggested that the alpha prospect can handle a max capacity of 40 Mt before it eventually spills over east to the beta prospect. This corresponds well to the mid-case scenario in this study for the alpha prospect.

6.1.2 Sognefjord, Fensfjord and Krossfjord Fm

At first glance, the Fensfjord Fm yields the highest numbers with regards to CO_2 storage capacity, with Sognefjord and Krossfjord following. Fensfjord Fm reaches a theoretical CO_2 storage capacity of up to 465.23 Mt at the high-case scenario, and 274.37 and 146.13 Mt for the mid- and low-case scenario, respectively. Sognef-

jord Fm show high numbers as well with the range 83.87-254.88Mt from the low- to high-case scenarios, respectively. Krossfjord Fm, however, shows low numbers, as the highest case is at 93.53 Mt. This is lower than Fensfjord formations' low-case scenario and Sognefjord formation' mid-case scenario. The reason why Fensfjord Fm yields the highest capacity numbers may be due to the ample thickness of the reservoir, compared to Sognefjord and Krossfjord Fm. However, this does not automatically mean that Fensfjord Fm is the optimal CO_2 storage candidate. We will investigate this further below.

The CO_2 storage capacity estimations for the Smeaheia formations combined almost reaches the Gt-scale, at 813.64 Mt for the high-case scenario. Even though these CO_2 storage capacity estimations are only theoretical and not directly applicable, as the whole area for the GN1101 is assumed as the "trap" when doing the calculations, it tells about the enormous CO_2 storage capacity potential of the Smeaheia CO_2 storage area. If the whole Smeaheia aquifer area was taken into account in this thesis' estimations, the number would obviously have been substantially bigger.

Estimations of the CO_2 storage capacity for the Smeaheia aquifer and the formations Sognefjord, Fensfjord and Krossfjord have been done in studies earlier with Bøe et al. (2002), Halland et al. (2014) and K. Anthonsen et al. (2014) being some of them. Halland et al. (2014) calculated a storage capacity at 4.09Gt for the Smeaheia aquifer, referred to as "Sognefjord Delta East", considering the three formations Sognefjord, Fensfjord and Krossfjord. Taking into consideration all the evaluated aquifers in the Norwegian North Sea (Halland et al. 2014, p. 72) there is an average at 4.5Gt for the storage capacity. To compare with results in this thesis, the mid-case scenario is used. The area used in this study for the capacity estimations of the Smeaheia aquifer formations is only considering the area within the data used, hence the GN1101 3D seismic cube. Thus to get comparable numbers, the bulk rock volume was scaled up at the size used in Halland et al. (2014), considering the whole Smeaheia aquifer outline. We then get a CO_2 storage capacity at 3.4Gt for the mid-case scenario. This number can be considered promising, taking into account the average storage capacity of the evaluated aquifers in Halland et al. (2014) and the storage capacity calculated for the "Sognefjord Delta East". It is, however, important to note that Halland et al. (2014) is not using the factor $(1-S_{wirr})$ (max CO_2 saturation at pore scale) in the CO_2 storage capacity calculations. This makes the comparisons less valid, but also tells that the capacity estimations in this thesis could have been even higher.

The structural closures within the Smeaheia aquifer are the main prospectives for CO_2 storage (Halland et al. 2014) in this area. Thus, when discussing CO_2 storage capacity it is most interesting to evaluate the alpha and beta prospects. However, it is important to evaluate the connected aquifer formations when assessing the CO_2 storage capacity of an area with structural closures within a saline aquifer area (Riis and Halland 2014). In addition, utilizing the deeper lying formations

Fensfjord and Krossfjord can contribute with more storage capacity, as mentioned more below. Based on the results discussed above, the Smeaheia aquifer, considering Sognefjord, Fensfjord and Krossfjord formations combined, entails good and sufficient CO_2 storage capacity. However, it is suggested in this study that Sognefjord and Fensfjord should be the main target reservoir formations for best utilization of the storage capacity.

6.1.3 Uncertainties of the CO_2 storage capacity estimations

There are several uncertainties in the calculations of the CO_2 storage capacity, as equation 3.22 consists of many properties having isolated uncertainties both independently and dependent of the other factors. However, for this discussion the main uncertainties in the CO_2 storage capacity estimations for the alpha and beta prospects and the Smeaheia aquifer formations are the uncertainty porosity ranges, the storage efficiency, the effect of pressure depletion on the density, and additional potential storage capacities.

The extracted porosity ranges are important to discuss. The first, and one of the main uncertainties being decisive for capacity estimations are the uncertainty porosity ranges used in the capacity estimations. These are based on the process done in chapter 4.7 and the results from chapter 5.2. The porosity values to cover the uncertainty ranges were extracted out from the mean porosity values from the porosity volume maps made with the surface attributes "Interval average: maximum" and "Average magnitude" for the prospects and formations, respectively, as described in methodology chapter 4.9.1 and 4.9.2.

For the alpha and beta prospects, extracting porosity values from the surface attribute "Interval average: maximum" may give too high porosity uncertainty ranges and may not reflect the lower porosity ranges of the prospects. Hence, the CO_2 storage capacity estimations for the alpha and beta prospects may be too optimistic. Petrophysical calculations from chapter 4.5.1 supports this with the calculated mean ϕ_t values being closest to the low-case scenarios, for well 32/4-1 corresponding to the alpha prospect and 32/2-1 for the beta prospect. Especially the extracted porosity values for the beta prospect from the inverted volumes are substantially higher than the mean ϕ_t from well 32/2-1. On the contrary, porosity ranges from Statoil (2016) suggest porosity values from 31-39% for both the alpha and beta prospect. This coincides better with the extracted porosity value for the alpha and beta prospect, as observed from table 5.1. Even though, it is believed that the uncertainty porosity ranges used in the storage capacity estimations for the alpha and beta prospect in this study may be too high.

An uncertainty noticed in the extracted porosity values from the porosity volumes generated in this thesis, is that the extracted mean porosity values from the inverted porosity volume don't follow the trend of the calculated mean well data ϕ_t values. From chapter 4.5.1 the Sognefjord Fm in well 32/4-1 (penetrating alpha

prospect) has higher ϕ_t than in well 32/2-1 (penetrating the beta prospect). From figure 4.11 and B.2 Sognefjord Fm plots closer to the shale trend line (Mavko et al. 2020; Greenberg and Castagna 1992) in well 32/2-1 than in 32/4-1. However, from table 5.1 the beta prospect show higher extracted porosity values for all the uncertainty scenarios, compared to the alpha prospect. This corresponds to the porosity and acoustic impedance trends discussed farther above in chapter 6.1.1. It is known from Z. Wang (2001) that seismic properties, and thus impedances, vary more caused by compaction, consolidation and cementation trends. The contact cement model (Dvorkin and Nur 1996; Mavko et al. 2020) can f.ex be plotted with the V_P vs. density plot from well data. Figure 6.1, shows that the Sognefjord sandstone in well 32/4-1 plots closer to the contact cement line than in well 32/2-1. The Sognefjord sandstone experience more quartz cementation in the west in the 32/4-1 well area (Fawad et al. 2021). Cemented units entails higher impedances, and thus lower porosity, because of the better connectivity of the grains Z. Wang (2001). This backs up that the porosity trends may be higher in the NE, and the beta prospect area, than the alpha and SW area.

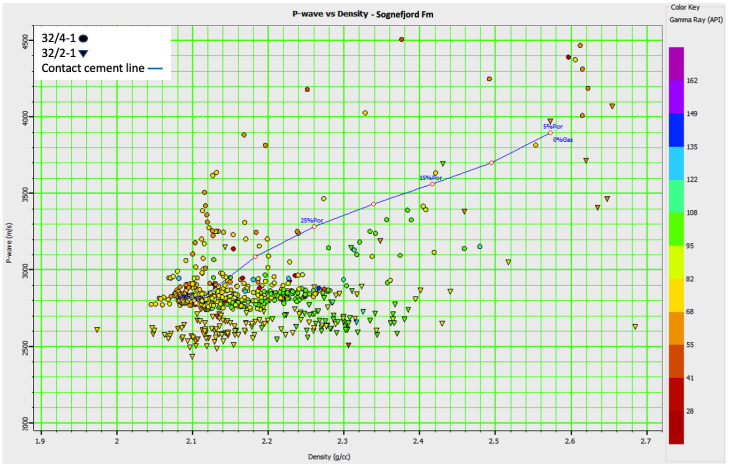

Figure 6.1: V_P vs. density cross-plot for Sognefjord Fm from well 32/4-1 and 32/2-1, with the plotted contact cement line from Dvorkin and Nur (1996). The points are painted with GR-values.

For the Sognefjord, Fensfjord and Krossfjord Fm, the extracted porosity values from the formation maps are substantially lower, as expected when using the surface attribute "Average magnitude". A more realistic average range for the porosity values spanning in the formations are believed to be reflected for the formations, using this surface attribute. However, as the porosity values are extracted from the mean values based on average magnitudes from points within intervals from the different formations, the true variability, especially the higher and lower end may not be reached. The flaw of averages can come into play here and the uncertainty might not catch up the natural variability of the composition of the sandstone

formations (Avseth et al. 2005).

Comparing with mean porosity values from the petrophysical calculations, the calculated total porosity, ϕ_t, from the well data is considered, as above. The high-case scenario porosity values for Sognefjord and Fensfjord Fm are closest to the mean ϕ_t well calculations for well 32/4-1 and 32/2-1. Taking into account well 31/6-6 and 31/6-3, lower porosity for both the formations are found. However these wells are positioned west for the Vette fault and farther south for this thesis 3D cube area, for well 31/6-6 and 31/6-3, respectively, with the Sognefjord and Fensfjord Fm lying deeper. Hence, these values might not reflect the trend of Sognefjord and Fensfjord Fm within this study's project area. For Krossfjord Fm, the mid-case porosity value match pretty well, observed from chapter 4.5.1 and table 5.2. Hence, it is believed that the uncertainty porosity ranges applied for Sognefjord and Fensfjord Fm in the capacity estimations are too low, however the extracted porosity values for Krossfjord Fm might be reasonable.

Furthermore, the storage efficiency entails a big uncertainty. The storage efficiency factors set in this thesis was based on two different approaches for the prospects and formations. The prospects was treated in a more local and site-specific scale and the formations in a wider regional aquifer scale. The ranges set in this thesis varied thus from 10-20% and 5-10%, for the prospects and formations, respectively. Hence, one of the most decisive varying properties in equation 3.22 and the CO_2 storage capacity estimations in this thesis is believed to be the storage efficiency, ϵ. It is also believed to be one of the most uncertain factors in the capacity estimations (Chadwick et al. 2008), and furthermore as studies have shown it can vary from 0.5—40% (Vangkilde-Pedersen et al. 2009; Bachu 2015; Ringrose 2020; Halland et al. 2014). Therefore it is important to discuss its uncertainties applied in this study. Storage efficiency vary based on a range of parameters (Miri and Hellevang 2018). Even though it is difficult to set a general strategy for deciding the storage efficiency of a CO_2 storage site (Bachu 2015), several authors suggest different approaches getting closer to a reasonable estimate (GHG 2009; Brennan et al. 2010; Okwen et al. 2010; Goodman et al. 2011; Yang Wang et al. 2013; Bachu 2015).

As described in 4.9, a rule of thumb strategy (Vangkilde-Pedersen et al. 2009; Brennan et al. 2010; Hjelm et al. 2020) was mainly followed deciding the storage efficiency for the alpha and beta prospects. This approach suggests that the storage efficiency can vary from 3-40% (Hjelm et al. 2020, fig. 11), depending on the reservoir quality and whether it is an open or closed system. Halland et al. (2011) also states that storage efficiencies can be derived from open and closed aquifer systems.

Evaluated prospects in Halland et al. (2011) vary in the range from 0.8-20%. Here it is further argued that the storage efficiency depends on the permeability relationship between horizontal and vertical permeability, k_{Hor} and k_{Ver}, respect-

ively. The higher the k_{Ver}/k_{Hor} ratio, the worse the distribution of the CO_2 in the reservoir will be Halland et al. (2014).

Based on Monte Carlo and numerical methods, Goodman et al. (2011) and GHG (2009), respectively, modelled more narrow ranges for the storage efficiency at a formation and site-specific scale, divided into lithologies within saline formations. A range from 3.1-14.92% is found for locally site-specific clastic sediments within these two studies (Goodman et al. 2011, p. 963, 12, table 14).

Ringrose (2020) further argues that the latest research demonstrates storage efficiencies in the 0.6-6% range. This is based on Okwen et al. (2010) gravity factor (Nordbotten et al. 2005), Γ, range found to be around 10-50 for CO_2 storage sites. Ringrose (2020) compares and confirms this with real experience from an operating CO_2 storage project. Based on time-lapse seismic data, the storage efficiency for the Utsira formation in the Sleipner CO_2 storage project can be calculated. Here, a storage efficiency of up to 5% is found (Ringrose 2020). Thus, it is believed that the storage efficiency range set in this study may be too high and optimistic for the CO_2 storage capacity estimations for the alpha and beta prospect.

The storage efficiency set for the formations was applied as guidelines more close to the aquifer at a larger scale, thus the storage efficiency was set lower. The studied regional aquifers in Halland et al. (2011) has storage efficiencies in the range from 0.8-5.5% and as mentioned in chapter 4.9.2 a storage efficiency for the "Sognefjord Delta East" was set to 5.5%. Further considering Goodman et al. (2011) and GHG (2009), a range for the storage efficiency for clastics at a formation scale is found to vary between 1.2-6% (Goodman et al. 2011, p. 963, 12, table 14). In regards to the storage efficiency uncertainty range (4.17) set in this research, it is assumed that the low-case scenario may have been set too high.

An important issue to address — and not considered in this study's CO_2 storage capacity estimations — is possible different scenarios for the density of the CO_2. The effect of pressure drawdown and depletion resulting from gas production of the nearby Troll field (Ane Lothe et al. 2019; Ane E Lothe et al. 2018; Statoil 2016; F. Riis et al. 2017) can lower the density of the injected CO_2 drastically, and thus lower the storage capacity (Lumley 2019; Statoil 2016). Thus, scenarios of the CO_2 being in a dense or gaseous phase is important to understand. For the alpha prospect the Statoil report (Statoil 2016) suggests a decrease in the CO_2 storage capacities in the range from 50-70 Mt with a pressure drawdown from 0-50 bar (Statoil 2016, p. 36, table 8). Furthermore the beta prospect can expect lower storage capacity values down in the range from 24-13 Mt in total considering the same pressure drawdown (Statoil 2016, p. 36, table 10). Thus, to get a more thorough evaluation of the CO_2 storage capacities of the alpha and beta prospects, pressure modelling and scenarios with pressure depletion should be done.

Calculating the structural capacity may be a lower limit estimation of the CO_2 stor-

age capacity of the prospects and formations. Thus, mechanisms not considered in this study might add additional storage capacities. First of all the phenomenon of stacked plume dispersion caused by semipermeable thin shale or siltstone layers can result in higher storage capacity, as firstly discussed by Lindeberg (1997) and Lothe and Zweigel (1999) with regards to the dissolution of CO_2 in the brine and the vertical sweep that causes the possible added storage capacity. The Sleipner project experienced some of these effects (Lindeberg et al. 2001; Arts et al. 2000). It is believed that this can add storage capacities for the alpha and beta prospect Statoil (2016), as the Sognefjord Fm entails of thin layers interbedded of limestone, siltstone and claystone within the sandstone intervals (Philips Petroleum Company 1997; Martin and Lowrey 1997; Talisman Energy 2008). Interbedded thin layers with higher acoustic impedance values (slightly red layers) from figure 5.2 may depict the thin interbedded higher velocity limestone and siltstone layers.

There is a possibility that injections into the deeper lying formations of Fensfjord or Krossfjord can trigger the layered plume dispersion phenomena, due to the less permeable interfingering of the Heather Fm. This is located in the SW of the Smeaheia area, within the GN1101 Dataset (2011) 3D cube. However, until reservoir modelling is done, these postulations remain as such (Statoil 2016).

Furthermore, building on the above, there is important to mention the ample potential capacities in the mechanisms of (Chadwick et al. 2008; Halland et al. 2014; Ringrose 2020), with varying effects:

- Residual trapping of the CO_2
- Dissolution of the CO_2 into the brine
- Mineral and geochemical trapping

Hence, to get more accurate estimations of the Smeaheia CO_2 storage area, numerical and dynamic reservoir modelling and geochemical analysis needs to be done.

6.2 Main result 2: CO_2 injectivity

6.2.1 Alpha and beta prospect

The beta prospect shows substantially higher kh-estimates than the alpha prospect. This is expected, with generally higher permeability values and thicker reservoir intervals in the beta prospect area. However, it is observed that both alpha and beta prospect have kh-estimates for the mid- and high-case scenarios that can be defined with a green light, applying the traffic-light constraints used in this thesis, seen from table 4.19. The low-case scenarios are also acceptable being defined in the yellow-light area with the estimates $4.79 Dm$ and $22.08 Dm$ for the alpha and beta prospect, respectively.

Statoil (2016) estimated the *kh*-estimate for both the alpha and beta prospect. From the lowest scenario it is estimated a *kh*-estimate at $13Dm$, followed by $66Dm$ and $304Dm$ for the middle and high scenario set in that study (Statoil 2016). The results for the alpha prospect corresponds OK with these estimates, even though a bit lower. This thesis' beta prospect *kh*-estimates are, however, substantially higher. This is mainly due to the high permeability values extracted from the beta prospect (table 5.3). Hence, these *kh*-estimates might have to be considered with caution.

6.2.2 Sognefjord, Fensfjord og Krossfjord Fm

Sognefjord and Fensfjord Fm show the best average injectivity values, however, the high-case Fensfjord Fm is considered the formation with best injectivity *kh*-estimate at $368.21Dm$. The Krossfjord Fm can generally be considered not as preferable for CO_2 injectivity as Fensfjord and Sognefjord, with only the high-case scenario defined as sufficient, taking into account the traffic-light cut-offs (table 4.19).

It can be valuable to compare with other evaluated *kh*-estimates. Valluri et al. (2021) entails field data on *kh*-estimate from operating and completed CO_2 storage projects. Statoil (2016) also has a *kh*-value for the Utsira formation in the Sleipner project. From the 11 evaluated projects an average of the *kh*-estimate is found to be $12Dm$. The highest *kh*-estimate is found to be $80Dm$ from the Sleipner project and the lowest estimates are reported to be $0.085Dm$. Taking the Sleipner project out of consideration, the highest *kh*-estimate reads $17.98Dm$. It emerges from these findings that the yellow light set for the traffic-light approach applied in this study (table 4.19) gives acceptable values from field experience. Thus, the green light cut-off for the *kh*-estimate is maybe set too high.

For further analysis of comparing the *kh*-estimates of the Smeaheia storage formations, some of the formations evaluated for CO_2 storage in Halland et al. (2014) is taken into consideration. The Cook formation gives the lowest value at $9Dm$ and Skade formation has the highest *kh*-estimate at $84Dm$, calculating the *kh*-estimate.

Following on the discussions above tells about good *kh*-estimates for both the alpha and beta prospect in the mid- and high-case scenarios and acceptable for the low-case scenarios. Considering the formations, both the Sognefjord and Fensfjord formation show good *kh*-estimates for the high- and mid-case scenarios and acceptable values for the low-case scenarios. Krossfjord Fm show good *kh*-estimate for the high-case scenario, acceptable for the mid-case scenario, however the low-case scenario is considered not an acceptable *kh*-estimate.

6.2.3 Uncertainties of the CO_2 injectivity estimations

First of all, it is an uncertainty factor in the average h set from the thickness maps for the prospects and formations. The depth model made in chapter 4.4 can entail uncertainties originating from the seismic interpretation done. The highest uncertainties lie in the horizon interpreted for top Heather B. As the top Heather B horizon reflection was difficult to follow and this formation interfingers in between Sognefjord and Fensfjord Fm (Ross et al. 2013), thins and pinches out moving from SW to NE, makes this a high uncertainty. Thus the thickness of the Sognefjord Fm is highly uncertain.

Secondly, the h might have been set too high. When calculating the kh-estimate for the alpha, beta prospects and the formations Sognefjord, Fensfjord and Krossfjord, the h-value used was the reservoir thickness. A more accurate estimation of kh will be to use h as the height of the interval for the injection well. Even though the most optimal well placement would be to inject from the base of CO_2 storage reservoir unit, using the reservoir thickness in the kh-estimate will therefore most likely overestimate the kh-estimate in some way. However, in cases where well design is not in place, the reservoir or column thickness of a formation or prospect will be an indicator for the h in the kh-estimate.

The kh-estimate approach might be too simple for describing CO_2 injectivity. The injectivity index (eq.3.24) is more robust, and a more accurate description of the actual nature of CO_2 injectivity, e.g. it includes the important parameters of the pressure regime, which is vital when ranking potential CO_2 storage areas and prospects (Halland et al. 2014). Figure 6.2 illustrates additional strengths of the injectivity index, relating it to the flow rate, and time frame.

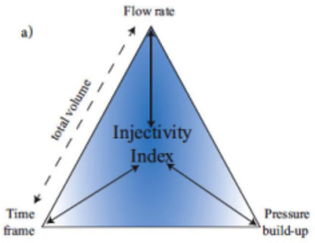

Figure 6.2: Injectivity index triangle describing the correlation with pressure, flow rate and time frame. Figure courtesy of Miri and Hellevang (2018)

However, the kh-estimate can perform as an effective CO_2 injectivity characterization. As already mentioned, the kh-estimate is proportional to the injectivity index formula and thus the injectivity of a well (Ringrose 2020; Miri and Hellevang 2018). This can be utilized and simplify injectivity estimations further. Mishra et al. (2013) concluded a correlation expression between the injectivity index and

the kh-estimate, based on field data. Valluri et al. (2021) examined the injectivity index - kh-estimate correlation further based on more field data. The study concluded with the correlation $J = 0.23kh$ for the upper bound, $J = 0.03kh$ for the lower bound and $J = 0.08kh$ for the median trend. Based on this, it is possible to estimate the injectivity index if the kh-estimate is known. This can give further valuable information about the CO_2 injectivity. Thus, by knowing only the permeability and reservoir thickness, evaluations whether a high/low permeability formation need longer/shorter injection intervals can be done.

6.3 Main result 3: Traffic-light injectivity maps

The kh-estimate results in 5.7 and 5.8 give indications of the average prospect and the formations' injectivity. However, when evaluating the CO_2 injectivity for a potential formation for a CO_2 storage project, it can be even more valuable to study the spatial variability of the injectivity. It is important to understand the injectivity trend of the formation and where it can be most suitable to inject CO_2. The traffic-light injectivity maps generated in this thesis is a an attempt to take the quantitative seismic study into understanding CO_2 injectivity of a formation, based on the traffic-light cut-off approach for the kh-estimate. In this chapter the mid-case uncertainty scenario maps are discussed.

The permeability volumes are made from poro-perm relationship (chap. 4.8). Hence, the traffic-light maps also follow the trend of the porosity volumes. The porosity volumes further vary based on the inverted acoustic impedance volume (chap. 4.7). Thus, understanding the rock properties being decisive for the seismic properties can help to understand the traffic-light injectivity maps.

Sognefjord Fm: Observations from figure 5.12 show that CO_2 injectivity can be considered more suitable in the NE of the Sognefjord Fm, following the trend from the lower kh-estimates (yellow light) in the SW to the higher kh-estimates in the NE (green light). This SW-NE trend coincides first of all with the increasing thickness of the Sognefjord Fm from SW-NE. Secondly a SW-NE trend correspond to the permeability map for Sognefjord Fm (fig. 5.9), with the high permeability spots corresponding to some of the clear green areas, in the east. Sognefjord Fm consists of high permeability values (with the average of $658.37mD$) with some of the low permeability ares reflecting the orange-red spots for the traffic-light map.

From figure 4.11 and B.2 the Sognefjord Fm plots closest to the wet sand trend (Greenberg and Castagna 1992) of the three formations, plotting closer to the shale trend in well 32/2-1 (fig. B.2). Figure 6.1 corresponds to the increasing SW-NE porosity, and thus permeability, trend. The green injectivity trend following more in the middle corresponds to the Statoil (2016) suggested drilling location nr. 3 for the alpha and beta prospects. If injection is done below the spill-points for the alpha and beta prospects, the vertical sweep effect is increased and thus the

potential storage capacities (Statoil 2016; Lindeberg 1997). However, migration analysis and pathways of the injected CO_2 need to be more accurate modelled to predict this.

Fensfjord Fm: Fensfjord formation shows promising injectivity throughout the formation with no red spots and generally middle to high injectivity values (fig. 5.13). However the best areas appear to be in the east with continuous high kh-estimates from NE to SE. High permeability values from 5.10 corresponds with the most suitable injectivity and green areas. The map further shows generally medium to high permeability values for Fensfjord Fm. With the good thickness throughout the formation it further confirms the good results of the traffic-light injectivity map for Fensfjord Fm.

Fensfjord Fm plots generally closer to the shale trend line (Greenberg and Castagna 1992) than Sognefjord Fm, seen from figure 4.11 and B.2. In well 32/2-1 Fensfjord Fm plots closer to the shale trend line than in well 32/4-1 and corresponds to the higher shale volume (chap. 4.5.1). Same as Sognefjord Fm, Fensfjord sandstone near well 32/4-1 consists of more abundant quartz cementation than near well 32/2-1, proved by Fawad et al. (2021), corresponding to the good injectivity areas in the east (5.13). Thus, with lower cementation, higher porosity and permeability values, injectivity might be preferable here NE near well 32/2-1. Moreover, with higher shale volume possibly contributing with interbedded semi-permeable thin shale beds, layered plume dispersion of the injected CO_2 might increase CO_2 storage capacity.

Krossfjord Fm: Figure 5.13 immediately shows an unpromising injectivity trend. kh-estimates are low decreasing from NE to the SW. The clear red areas in the middle and west of the traffic-light map are areas not suitable for CO_2 injection. The single green spot with the highest kh-estimates of the map shows the only potentially sufficient injection area, NE in the map and south for well 32/2-1. Medium kh-estimates is observed nearby, and a bit farther south, and with the green spot these areas entails the best area for injection in Krossfjord Fm, if ever considered. The bad injectivity trend and the low kh-estimates are originated from the rather thin Krossfjord Fm throughout the project area. The increasing SW-NE permeability trend is once again decisive for the end traffic-light trend and describes the slightly better injectivity areas in the east for Krossfjord Fm. With the mean permeability value at $31.42mD$ for the mid-case gives Krossfjord Fm the lowest permeability values of the evaluated formations.

Krossfjord Fm plots generally closer to the shale trend line (Greenberg and Castagna 1992) in well 32/2-1 than 32/4-1 (figure 4.11 and B.2). Also the cementation is lower in the east near well 32/2-1 proved by (Fawad et al. 2021).

To sum up, from the traffic-light injectivity maps, Fensfjord Fm trends with the utmost green areas and thus best injectivity potential. Sognefjord Fm shows also

generally good injectivity throughout the formation, however some areas SW in the map shows some red "lights" and thus not preferable for injection. Krossfjord Fm shows of the three formations the most red trend, as expected.

Based on this it is suggested to utilize the good injectivity potential of Fensfjord Fm. Targeting both Fensfjord and Sognefjord Fm for CO_2 storage, a great Mt-scale capacity will be expected and the sweep effect will contribute to additional storage capacity. However, thorough migration analysis and well design is needed to understand how the CO_2 will behave in the interaction between Sognefjord and Fensfjord Fm, in addition to the interfingering Heather Fm siltstone in the SW of the project area.

6.3.1 Uncertainties of the traffic-light injectivity maps:

The main reservoir property being decisive for the CO_2 injectivity kh-estimate is the permeability. Thus it is important to understand the spatial variability of the permeability maps. The injectivity and permeability trends are argued above based on rock properties mainly being decisive for porosity, since the permeability volumes originates from the poro-perm relationships. Even though permeability may vary by the same properties indirectly, permeability is greatly affected by other factors. Bedding, pore geometry and tortuosity, and stress conditions are some of the important properties being decisive for the permeability within a rock system (Glover 2001). As the traffic-light injectivity maps are highly dependent on the permeability, there is a weakness of understanding the true permeability trends from the traffic-light maps.

As discussed in chapter 6.2, the thickness h is an uncertainty. However, with the traffic-light injectivity maps, the trend of the thickness maps have to be understood better and can be decisive for the injectivity in the areas where there are low permeability values, f.ex. Thus, uncertainties can be linked to discrepancies in the thickness maps.

The N/G is used from the mean value N/G calculated from well data for the respective formations. Hence, this is not reflecting the spatial variability of the shale volume and the N/G. Errors thus exist, with averaging over areas with lower or higher N/G.

6.4 Applicability of this thesis' workflow

With this thesis traffic light model, to seismically guide estimations of CO_2 storage resources, it can be an effective workflow for evaluating regional aquifers being candidates for CO_2 storage. In this thesis, the Smeaheia aquifer has been seismically evaluated, within a 3D seismic cube, to derive CO_2 storage resource estimations for the entailing prospects and reservoir formations. Discussing the results of the traffic-light approach in table 5.9, both alpha and beta are prom-

ising prospects, but beta is decidedly the better of them, due to the significantly higher scores.

Furthermore, Fensfjord does yield the highest CO_2 capacity numbers, yet Sognefjord is the optimal candidate. We can say this due to the higher CO_2 storage resource properties (porosity, permeability, and *kh*-estimate). If we focus on the mid-case, it even comes close to the capacity estimate for Fensfjord. But, it is important to emphasise the high potential of Fensfjord Fm as it shows a generally good injectivity across its formation based on the traffic-light injectivity map. In an ideal case we would perhaps inject in the deeper lying Fensfjord Fm and utilize both the formations' CO_2 storage potential.

Reflecting further on the applicability of such a method proposed in this thesis, scaling the method and sight more regionally, but at the same time handling the prospects for CO_2 storage at a local scale, can be even more interesting. Imagining conducting several 3D seismic datasets over different candidate aquifers along the NCS, the most suitable CO_2 storage prospects and formations within the aquifer could be mapped. The latter describes the work done in Halland et al. (2014), however with this thesis' seismically guided traffic-light approach, the seismic data can be utilized even more robust and effective to identify the best CO_2 storage sites. Moreover, our traffic-light approach take the utilization of typical high and low scores CO_2 storage reservoir properties (Chadwick et al. 2008; Halland et al. 2014; K. Anthonsen et al. 2014) a step further with characterizing CO_2 injectivity (with regards to the *kh*-estimate) and generation of volume maps.

Following on the above, Lloyd et al. (2021) do suggest a regional screening workflow for CO_2 storage sites, with seismically aided methods. Based on play-based and risking exploration approaches, suitable prospects within the Utsira aquifer formation are identified and an elegant CO_2 prospect portfolio is made. Comparing the works of Lloyd et al. (2021) with this thesis methodology, Lloyd et al. (2021) act as a more robust approach taking into account the mapping of containment, in combination with mapping porosity, intra-formation mudstones and fill & spill behaviour. In fact, a big drawback with our workflow is by not including the containment aspect as accurate, as containment act as one the most important requirements for characterizing CO_2 storage sites. Hence, a further development of the optimal workflow for CO_2 storage site screening and resource estimation should take the containment aspect into account.

6.5 Seismic inversion: Post-stack inversion

Figure 5.2 is an important result in this thesis, as it is the first step in the seismic quantitative process and decisive for the further results for the porosity and permeability volumes and values extraction of the Smeaheia CO_2 storage complex. In this chapter, the uncertainties in the post-stack seismic inversion process

are discussed. Below are some of the uncertainties being decisive for the seismic inverted acoustic impedance volume:

Post-stack inversion method chosen: There are not always an obvious correct post-stack inversion method to use (Russell and Hampson 1991). As described in chapter 4.6, a model-based inversion was done to generate the final acoustic impedance model in figure 5.2. It is argued in Veeken et al. (2004) that with little well control, the model-based inversion method can still give reliable results. In this thesis, only two wells are available in the relevant project area, and hence used in the post-stack seismic inversion process. Hence, the model-based inversion method is believed to fit this thesis purpose OK, with this in mind. Lack of well control is discussed further down.

QC of the inverted result: A normal procedure of quality checking the seismic inversion result is to plot the synthetic and seismic error and check the acoustic impedance values at well locations with the inverted result (Simm and Bacon 2014). This can be done through the **inversion analysis** step and **cross validation** (Simm and Bacon 2014). Figure 6.3 shows the inversion analysis, from step 9 in table 4.7.

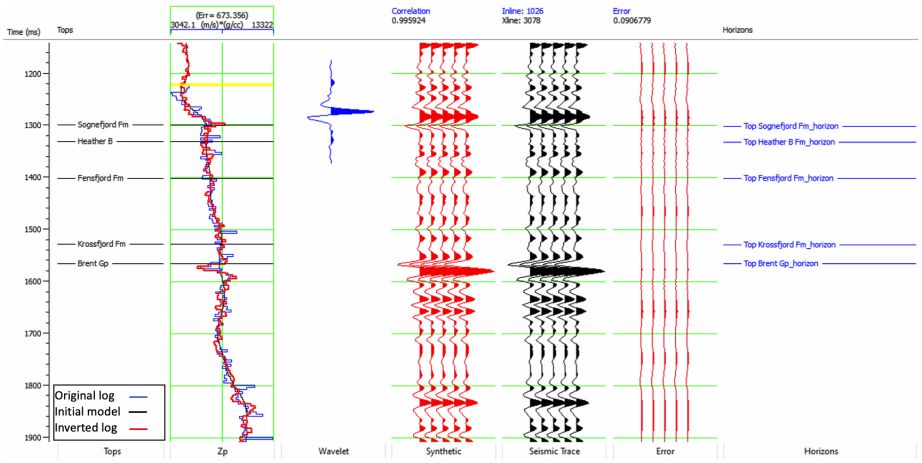

Figure 6.3: Inversion analysis at well 32/4-1. From left we see the I curves compared at the well position; the original I log in blue, initial model in black and inverted log in red. The error compared with the synthetic model and the seismic data is visualized in the right end.

It is observed that there is a pretty good fit with the original acoustic impedance log from well 32/4-1 in blue and the inverted impedance log in red. We further see there is a high correlation at 0.9959 and a small error, between the inverted synthetic trace and the original seismic trace, at approximately 0.0907. However, as well 32/4-1 is used as an input for creating the initial model, we would expect a good fit at this position.

A cross validation and a blind test can further be done and maybe tell more about how good the inversion result is (Simm and Bacon 2014). This is done with a well that is in the project area, but not used in the model. For this, well 32/2-1 is checked for a cross validation, as this is the only other well in the project area:

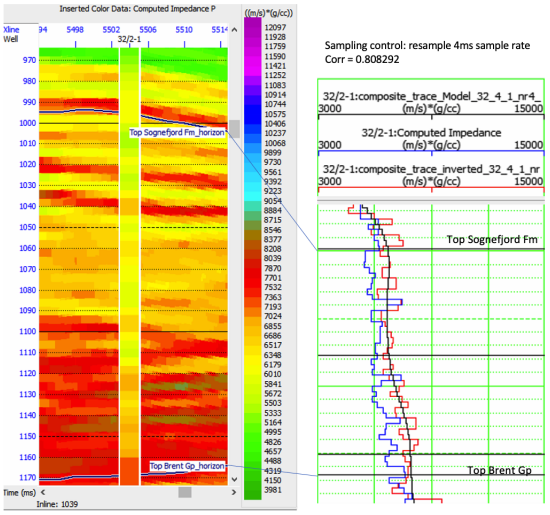

Figure 6.4: Cross validation of the resulting impedance volume and computed impedance at well 32/2-1. To the left: inverted impedance volume visualised at well 32/2-1 position, with computed impedance from well 32/2-1. To the right: Sampling control: the original I log (resampled at 4ms) is in blue, the initial model is in black and the inverted I log is in red.

The plotted impedance logs from well 32/2-1 and the inverted log, to the right in figure 6.4, show a correlation of approximately 0.8083. Here the sampling control is done with resampling at 4ms sample rate to compare with the inverted log. When displaying the original impedance log from well 32/2-1 (Talisman Energy 2008) and comparing with the inverted log, the correlation increase to 0.8246.

Observations show a moderate fit of the general trend vertically; the acoustic impedance generally increase with depth, both in the well and the inverted impedance volume. However, to the left, we see that the computed acoustic impedance from well 32/2-1 overlain on the inverted impedance volume show a generally lower value trend of the acoustic impedance. That is also seen on the plot of their acoustic impedance to the right. The inverted impedance volume seem maybe to overestimate the acoustic impedance going from SW around well 32/4-1, to the NE around well 32/2-1.

Even though there are a good fit at well location in 32/4-1 and moderate fit for well 32/2-1, the resulting inversion model might not be laterally accurate, as only one well is used in the initial model and one well for the cross validation. In fact, doing a cross validation for only one well can be a weakness. Simm and Bacon

(2014) argue that doing a cross validation is only a good test if a fair amount of wells are available in the project area. The correlation and trend in figure 6.4 is therefore considered with caution. Presence of few wells used in the initial model and to cross validate with is thus a weakness of the inversion result in this thesis, also emphasized below in the problems with wavelet and tuning.

Non-uniqueness problem: As a deterministic model-based inversion is used for quantitative processes, the problem of non-uniqueness is highly abundant and important to address. When executing a model-based inversion and iterating to get a small error, there are multiple solutions that can fit the input data and the choices made throughout the inversion process (Hampson and Russell 1999; Simm and Bacon 2014). Therefore the small error and good correlation seen in figure 6.3 is firstly maybe not the smallest error possible to generate for the solution. Secondly, there might be more solutions that generate almost the same fit and error, and visually can look almost exactly alike (Hampson and Russell 1999).

Low frequency error trend: The non-uniqueness problem is often linked to the low-frequency error trend problem (Hampson and Russell 1999). When calculating the reflection coefficients and the derived impedance, small errors in the reflection coefficients calculations can contribute in significant errors in the resulting impedance. Due to the lack of low-frequency information from seismic, we thus can get a low-frequency error trend when merging the impedance model with an inversion algorithm (Hampson and Russell 1999; Simm and Bacon 2014).

Wavelet: The extracted wavelet used in the generated model is decisive for a good inversion result (Hampson and Russell 1999; Simm and Bacon 2014), and it is important to address the wavelet methods and issues connected. As described in 4.6, in the end generated inverted impedance volume, a wavelet extracted from well 32/4-1 was used to set a constant phase, combined with amplitude spectrum information from the seismic.

Using well log information for wavelet extraction is reliant on a good well-tie (Hampson and Russell 1999; Simm and Bacon 2014). Getting the full wavelet information from the well log can in theory calculate an exact wavelet at that well position (Hampson and Russell 1999). However, any small errors or misinterpretations of stretching and time-shifting the well-tie can have consequences on the resulting inverted result. Firstly, these errors can have consequences on the phase spectrum. Wrong generated side-lobes in the end result and distorted high frequency spectrum in the wavelet can furthermore come from errors in the well-tie (Hampson and Russell 1999). These errors are especially addressed when using the well log for both the phase spectrum and full amplitude. When the well log information is only used to define the average constant phase, information from the seismic and statistical wavelet information can be utilized, so an eventual mistake in a well-tie is not that decisive in the inversion process (Hampson and Russell 1999).

If more wells were abundant in the project area, a solution to the wavelet uncertainty could be to to average the wavelets extracted from the wells in the project area (Simm and Bacon 2014). That is, however, not the case in this project, as only a well-tie from well 32/4-1 is done. The well-tie in 32/4-1, from 4.5, is believed to show an OK correlation. Hence, it is believed that the wavelet information extracted from well 32/4-1 and seismic, and decided for the last input for the seismic inverted impedance volume, is more accurate than if only the statistical extracted wavelet was used or only the well log for phase and full amplitude spectrum.

Resolution and tuning: An issue to address with the deterministic seismic inversion method used in this thesis, is the simplicity and resolution of the modelled data and eventual residual tuning effects present. As deterministic inversion is a smoothed solution of a modelled seismic trace, based on limitations from the bandwidth of the data, intervals of interest on the scale lower than 1/4 of the seismic wavelength are not reliable (Simm and Bacon 2014). Executing seismic quantitative calculations from intervals like these would therefore in most cases not give accurate results. Furthermore on the horizontal resolution, there is important to emphasize the lateral uncertainties in the seismic inverted result, as the inversion in this thesis is based on two wells far from each other. Most likely, residual tuning effects are present due to this (Simm and Bacon 2014). However, with the horizon constraints building up the interval of interest, the most important tuning effects are believed to be removed. The impedance values and trend of the interfaces of the most important formations are thus believed to be understood.

Based on this it is reflected that this thesis will not generate the most precise quantitative results of the Smeaheia CO_2 storage formations, based on the generated inverted impedance volume. The scale-up problem from handling of the well and seismic data is important to emphasize. However, reasonable values and trends of the Sognefjord, Fensfjord and Krossfjord Fm is believed to have an OK basis with inverted impedance volume, before continuing with quantitative porosity and permeability measurements.

6.6 Generation of the porosity volume maps

The impedance-porosity relationship interpreted and created in 4.7 builds the basis for the results in chapter 5.2. It is therefore important to discuss the uncertainties linked to this process.

There can be two uncertainties that comes into account when indirectly correlating porosity to seismic data and an inverted acoustic impedance volume (Doyen 1988). Doyen (1988) first underlines the problem of non-uniqueness of the seismic data, and thus in the seismic inverted volume. This continues on the discussion above, in chapter 6.5, about the non-uniqueness problem in the model-based inversion method. Hence, as there may be multiple other possible solutions for the acoustic impedance volume generated in the post-stack inversion, done in chapter 4.6, there are indirectly multiple solutions for the porosity volumes generated. Furthermore, the uncertainties coming into account when generating the acoustic impedance volume, indirectly affects the generated porosity volumes and results in 5.2. Only correlating the porosity to the variation of acoustic impedance might be a further flaw (Doyen 1988).

The methods of correlating acoustic impedance and porosity with only regression formulas can have their drawbacks and is a weakness in this thesis. Doyen (1988) compares the regression approach (Guidish and De Buyl 1987; Maureau and Van Wijhe 1979; Angeleri and Carpi 1982) with geostatistical approaches. Doyen (1988) argues that the regression approach handles the data of being independent of spatial variations, and to overcome that drawback, geostatistical methods like kriging and co-kriging is inherited in the workflow. Bosch et al. (2010) demonstrates how geostatistical approaches in the seismic inversion process are adding value in the sense of adding constraints of the spatial uncertainty. As discussed earlier, the spatial uncertainty in this thesis is clear with the sparse wells available. A more holistic approach and thorough workflows of combining rock physics and geostatistical approaches in the seismic inversion process, discussed in Bosch et al. (2014), would make the process more robust. However, these geostatistical approaches in the inversion process has been out of scope for this thesis.

The uncertainties of the porosity maps are further discussed. When plotting the impedance-porosity data from the well data and for the chosen formations, the trend of the data was first studied. It was chosen only to use data from the well 32/4-1 and 32/2-1. However, if the p-impedance and total porosity is plotted with data from more wells, the general trend and results of the specific formation might be more accurate for the general Sognefjord Fm, as more data is used. P-impedance and total porosity data for Sognefjord Fm from all the wells are plotted in figure 6.5, as an example.

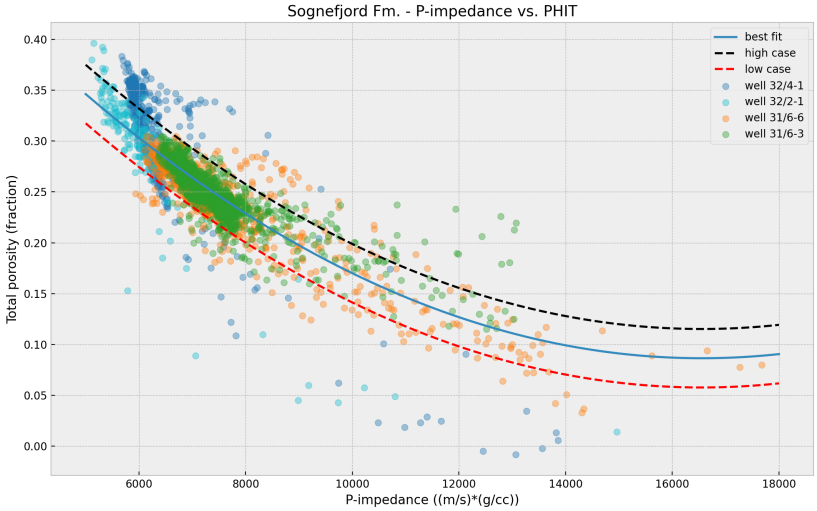

Figure 6.5: P-impedance vs. PHIT for Sognefjord Fm, best fit line with error, data points from all wells: 32/4-1, 32/2-1, 31/6-6, 31/6-3. All the formations are water-filled.

It is observed here, from 6.5, that the best fit line shows a much less steep trend than in the final used correlation in figure 4.15. We also see that the data points from well 31/6-6 and 31/6-3 generally show lower porosity values, as they also show lower average porosity values from the petrophysical evaluation in table 4.4. Using a correlation from figure 6.5 might would have given a better understanding of the general extended Sognefjord Fm, as mentioned, especially outside of the project area. However, just by looking at the plotted data, we see that data from well 31/6-6 and 31/6-3 dominate the density of high p-impedance values and higher porosity data in this area. Hence, a regression formula extracted from figure 6.5 and used with the inverted impedance volume from 4.6, would have overestimated the porosity values substantially in the higher acoustic impedance areas 5.2. This is not desirable and would perhaps give a wrong trend for the Sognefjord Fm that lies in the Smeaheia CO_2 storage area. As a result of this, it is believed that the correlation used in figure 4.15, utilizing only well 32/4-1 and 32/2-1, fits this thesis purpose.

The importance of removing outliers in the used data for the cross-plotting is also important to emphasize. In the figure 6.6, the data includes outliers and a best fit polynomial regression line, with error lines, is plotted. The correlation is 0.85. With removing the outliers figure 4.15 shows even better correlation. However, the outliers were removed manually. This should perhaps have been an automated step, e.g. a filter.

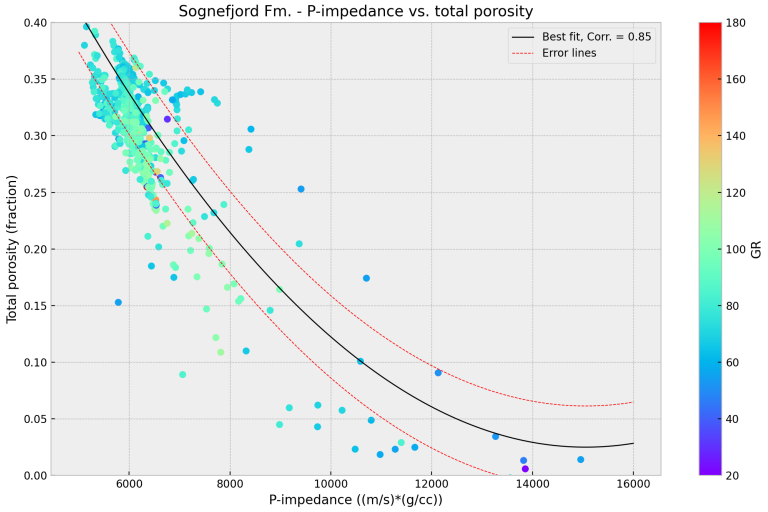

Figure 6.6: P-impedance vs. total porosity for Sognefjord Fm, best fit line with error, data points from wells: 32/4-1 and 32/2-1. The data points are painted with their corresponding GR-value.

It is further important to discuss the uncertainty ranges set in this thesis that builds on the regression analysis in chapter 4.7; the high-, mid- and low-case scenarios for the prospects and formations. These uncertainty ranges inherently follows in the methodology and results generated. The R^2 numbers for the impedance-porosity regression analysis done for the formations shows good statistical fit; 0.93, 0.94 and 0.88 for the Sognefjord, Fensfjord and Krossfjord Fm, respectively. However, these correlations were made removing the outliers. Therefore it is important to look at the clean data with histograms (fig. 6.7) and pdfs (fig. 6.8).

To further quantify some of the uncertainty that lies in the data to create the impedance-porosity relationship, uncertainty quantification of the P-impedance and total porosity from the well data is done. Total porosity data calculated from the Sognefjord Fm is quantified, as an example to quantify the porosity uncertainty. Histograms and kernel estimates for pdf (Avseth et al. 2005) of the total porosity, ϕ_t, from the calculated well data is presented in figure 6.7 6.8. Observing at the spread of the data it spans out from low porosity values around 10% up till 37-38%. The histogram visualizes the distribution of our dataset, here we can observe the outliers and use this information as part of our cleanup. The left tail for the low porosity values are identified as the outliers.

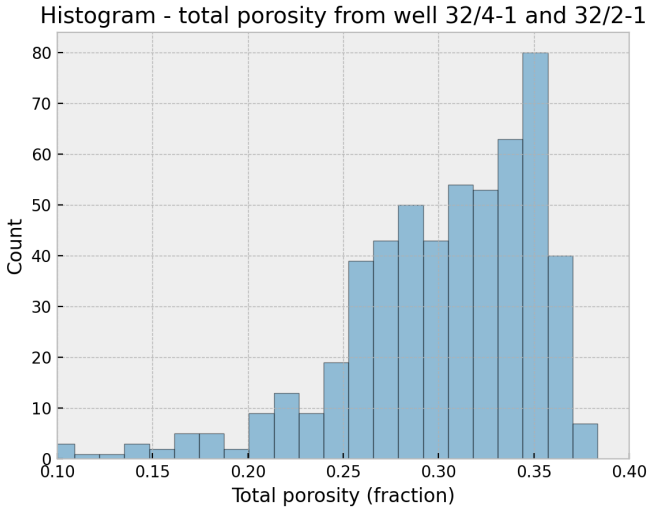

Figure 6.7: The histogram for the calculated ϕ_t for Sognefjord Fm from the well data from well 32/4-1 and 32/2-1.

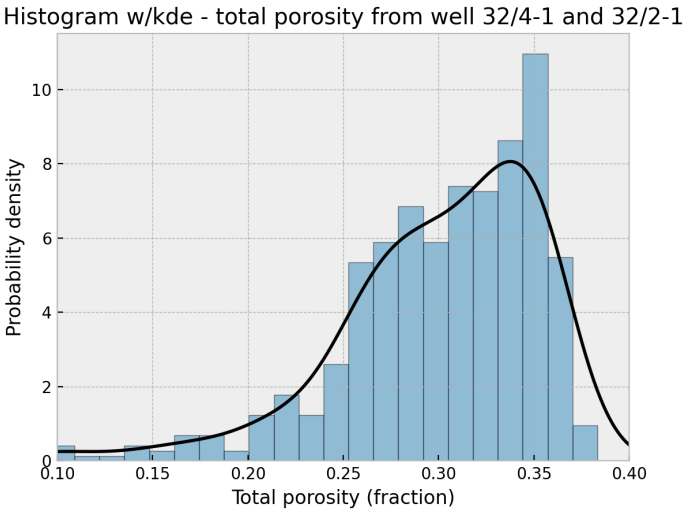

Figure 6.8: The kernel density estimations over the Sognefjord Fm calculated total porosity dataset for well 32/4-1 and 32/2-1.

6.7 Generation of the permeability volume maps

As previously we have correlated the porosity volumes with the permeability volumes based on the creation of the poro-perm relationship, described in chapter 4.8. The generation of the permeability volume maps are the next sub-result being decisive

for the *kh*-estimate and the traffic-light injectivity maps. As the processing steps go, the porosity volumes sub-result feeds into the permeability volumes sub-result. It is important to point out that the porosity volumes high-, mid-, and low-case feed into their respective permeability volumes high-, mid-, and low-case. This means that any errors that are borne in these cases, will carry on and potentially be exacerbated in the next steps, as errors are prone to grow.

From well 32/4-1 and the conventional core analysis, the sedimentology and petrography report (Martin and Lowrey 1997) entails cross-plots of the measured porosity and horizontal permeability (k_{Hor}) from the core analysis. Thus, it is possible to do a quick QC of the cross-plot that is created in this thesis. Figure 6.9 is compared with thesis' poro-perm relationship, scaled up in figure 6.10. It can be observed that the cross-plots has a good match. The permeability values picked out from the final well report from well 32/4-1 (Philips Petroleum Company 1997) are therefore believed to be understood. Of the available porosity-permeability data for Sognefjord Fm, this is considered as the closest one can get.

An uncertainty lies in the poro-perm relationship made for both Fensfjorf Fm and Krossfjord Fm. As no core data exists for Fensfjord and Krossfjord Fm from the wells in the 3D seismic area (32/2-1 and 32/4-1), core data from well 31/6-6 was used instead. Well 31/6-6 lies in the troll area, west for the vette fault, and thus outside the Smeaheia area. Furthermore top Fensfjord and Krossfjord Fm are found 350m deeper in well 31/6-6. Thus, the poro-perm relationship made for Fensfjord Fm from well 31/6-6 are would most likely differ from the real poro-perm relationship in the Smeaheia area.

Furthermore, an even higher uncertainty lies in the poro-perm relationshop assumed for Krossfjord Fm. No core data existed in well 31/6-6 for Krossfjord either, and the poro-perm relationship for Fensfjord was assumed following the trend in the deeper and more shaly Krossfjord Fm, as described in chapter 4.8. Hence, a more thorough poro-perm relationship for the Fensfjord and Krossfjord Fm are needed to generate more reliable permeability volumes, and moreover more reliable injectivity estimations and traffic-light injectivity maps.

When available core data for porosity and permeability it is important to examine the correlation. If a correlation is seen, as often expected for sandstone reservoirs if the data is available and reservoir unit is well defined, this correlation can give surprisingly good results (Ellis and Singer 2007). However, if more data is available, it is important to correlate with more data, as permeability varies with more factors. This is not done in this thesis and the results in this thesis are clearly biased with the porosity variations, and thus acoustic impedance. It is also important to emphasize the uncertainy linked to the core measurements done in Philips Petroleum Company (1997) and Statoil AS (1984).

A check with the kozeny-carman relation 3.20 was done (Carman 1961), as per-

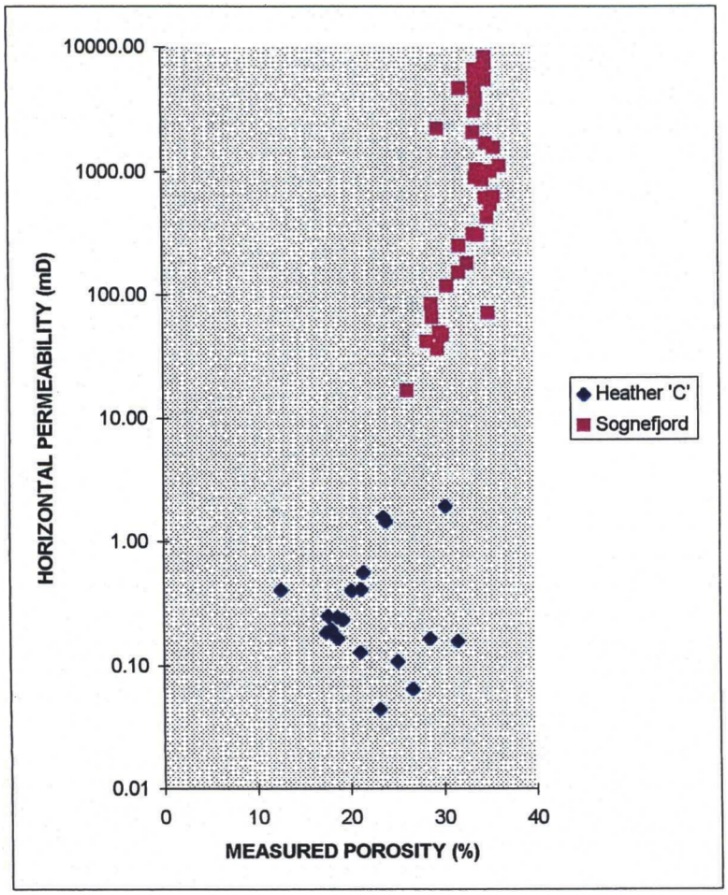

Figure 6.9: Measured porosity vs. horizontal permeability cross-plot from core analysis from the sedimentology and petrography report for well 32/4-1. Figure taken from (Martin and Lowrey 1997).

meability models can aid when lacking of poro-perm data. If such a model is found to fit a dataset good, the model may be a good relationship than a correlated poro-perm relationship, especially if the poro-perm core data is limited. Maybe the most known is the Kozeny-Carman relationship (Ellis and Singer 2007; Glover 2000; Mavko et al. 2020). It is possible to model Kozeny-Carman curves with differing tortuosity to see where existing data plot against the model. This can tell about how well a formation fit the Kozeny-Carman model (Mavko et al. 2020). The core data from well 32/4-1 for Sognefjord Fm was thus plotted with the Kozeny-Carman model curve. We did not get a good relationship, and it was decided that the core measurements would be a better fit, especially for Sognefjord Fm.

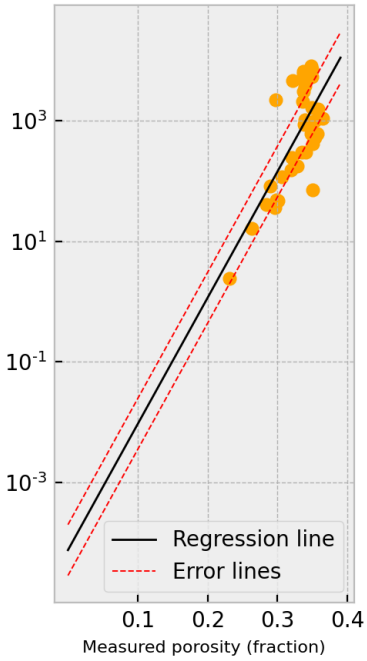

Figure 6.10: Measured porosity vs. horizontal permeability cross-plotted, figure 4.18 re-scaled. Horizontal permeability on the y-axis and measure porosity on the x-axis.

Chapter 7

Conclusion

This study demonstrates how seismic quantitative estimates from seismic data can be an effective tool to aid in CO_2 storage site characterization. Through post-stack seismic inversion, porosity and permeability trends and values are derived, and we can determine and improve estimates of CO_2 storage capacity and injectivity (in terms of the kh-estimate). Through a traffic-light approach applied in this thesis, the relevant prospects and formations in the Smeaheia CO_2 storage area are ranked and visualized.

Based on the CO_2 storage resource estimations from this work, alpha and beta prospects are identified as especially good candidates for storage. Alpha mid-case shows average porosity, permeability and kh-estimate values of 34%, 998.99mD and 33.20Dm, respectively. The estimated CO_2 storage capacity shows promising value of about 40Mt. The Beta mid-case gives an even stronger green-light signal, showing porosity, permeability and kh-estimates values of 37%, 4246.46mD and 247.93Dm respectively. Beta-mid's permeability score is far higher than the threshold of 500mD.

Of the evaluated formations, Sognefjord Fm shows the most promising CO_2 storage resource estimations, scoring high with generally green lights for both the mid- and high-case. Sognefjord mid-case shows porosity, permeability and kh-estimate values of 24%, 658.37mD and 37.90Dm. The traffic-light injectivity map for Sognefjord mid shows best injectivity in the east. Fensfjord's high-case does indicate a potentially good candidate, whilst the mid-, and low-case suggest that it is perhaps sub-par. However, the traffic-light injectivity map paints a more positive view, showing major patches of green and sufficient injectivity locations throughout. Krossfjord, on the other hand, is a poor candidate, even the optimistic high-case scenario does not give the all-green. The probabilistically more reliable mid-case is all-yellow, with porosity, permeability and kh-estimate values of 20%, 31.42mD and 0.82Dm, respectively.

The mid-case represents the actual result, and we create a spread with boundaries low and high. We create such a spread in order to be able to state with a high level of confidence that the result is within that boundary. The spread is quite substantial in many cases however, e.g. Fensfjord's k low-case is $13.43mD$, and high-case at $3426.41mD$. However, the mid-case remains the core metric, and the boundaries are to be regarded as useful yet supplemental data.

Chapter 8

Further work

This master thesis workflow and methodology shows how seismic data can be utilized in estimating and ranking CO_2 storage resources in the Smeaheia CO_2 storage area. However, improvements are required for the workflow to improve as an optimal seismically guided CO_2 storage resource estimator and for Smeaheia to be fully understood. Below are some main thoughts highlighted:

First of all, including the containment confidence aspect would strengthen this thesis' traffic-light approach. Understanding more thoroughly the spatial variability of the sealing capacities for Heather C and Draupne Fm, can thus either strengthen the confidence of the suitable green-light defined areas in the traffic-light maps (ch.5.6), or filter out evaluated areas not suitable for CO_2 injection.

Secondly, improvement of the CO_2 injectivity evaluation would further make this thesis work more robust. The kh-estimate approach might be too simplistic, excluding pressure in the calculations. The CO_2 injectivity index equation would, together with higher containment confidence, improve this thesis approach for estimating CO_2 storage resources of the Smeaheia area.

Further considering the general workflow, better statistical approaches is suggested to take this thesis methodology further. The seismic inversion process can be done more accurately to increase the robustness of this thesis' workflow.

Utilization of more data by including more wells and include 2D and 3D seismic data would give better understanding of the Smeaheia aquifer.

We need a more thorough understanding in order to finally conclude Smeaheia as the next optimal CO_2 storage area in the Norwegian North Sea. For instance, whether there is a possibility of migration of CO_2 near the alpha prospect (Statoil 2016). Another example is understanding the in-situ PVT conditions. These are only a few of the issues that need to be covered.

Bibliography

Angeleri, GP and R Carpi (1982). 'Porosity prediction from seismic data'. In: *Geophysical prospecting* 30.5, pp. 580–607.

Anthonsen, KL, P Aagaard, PES Bergmo, SR Gislason, AE Lothe, GM Mortensen and SÓ Snæbjörnsdóttir (2014). 'Characterisation and selection of the most prospective CO2 storage sites in the Nordic region'. In: *Energy Procedia* 63, pp. 4884–4896.

Arts, Rob, Ivar Brevik, Ola Eiken, Roger Sollie, Emmanuel Causse and B Van Der Meer (2000). *Geophysical methods for monitoring marine aquifer CO2 storage–Sleipner experiences*.

Avseth, Per, Tapan Mukerji and Gary Mavko (2005). 'Statistical rock physics: Combining rock physics, information theory, and statistics to reduce uncertainty'. In: *Quantitative Seismic Interpretation: Applying Rock Physics Tools to Reduce Interpretation Risk*. Cambridge University Press, pp. 111–167. DOI: 10.1017/CBO9780511600074.004.

Bachu, Stefan (2003). 'Screening and ranking of sedimentary basins for sequestration of CO2 in geological media in response to climate change'. In: *Environmental Geology* 44.3, pp. 277–289.

Bachu, Stefan (2015). 'Review of CO2 storage efficiency in deep saline aquifers'. In: *International Journal of Greenhouse Gas Control* 40, pp. 188–202.

Bachu, Stefan, Didier Bonijoly, John Bradshaw, Robert Burruss, Sam Holloway, Niels Peter Christensen and Odd Magne Mathiassen (2007). 'CO2 storage capacity estimation: Methodology and gaps'. In: *International journal of greenhouse gas control* 1.4, pp. 430–443.

Baklid, Alan, Ragnhild Korbol and Geir Owren (1996). 'Sleipner Vest CO2 disposal, CO2 injection into a shallow underground aquifer'. In: *SPE Annual Technical Conference and Exhibition*. OnePetro.

Banks, David (2012). *An introduction to thermogeology: ground source heating and cooling*. John Wiley & Sons.

Batzle, Michael and Zhijing Wang (1992). 'Seismic properties of pore fluids'. In: *Geophysics* 57.11, pp. 1396–1408.

Bentham, Michelle, Tom Mallows, Jonathan Lowndes and Andrew Green (2014). 'CO2 STORage evaluation database (CO2 Stored). The UK's online storage atlas'. In: *Energy Procedia* 63, pp. 5103–5113.

Biot, Maurice A (1956). 'Theory of propagation of elastic waves in a fluid-saturated porous solid. II. Higher frequency range'. In: *The Journal of the acoustical Society of america* 28.2, pp. 179–191.

Bøe, Reidulv, Christian Magnus, Per Terje Osmundsen and Bjoern Ivar Rindstad (2002). 'CO2 point sources and subsurface storage capacities for CO2 in aquifers in Norway'. In: *NGU report* 2002132.

Bosch, Miguel, Tapan Mukerji and Ezequiel F Gonzalez (2010). 'Seismic inversion for reservoir properties combining statistical rock physics and geostatistics: A review'. In: *Geophysics* 75.5, 75A165–75A176.

Bosch, Miguel, Tapan Mukerji and Ezequiel F Gonzalez (2014). 'Seismic, rock physics, spatial models, and their integration in reservoir geophysics'. In: *Encyclopedia of exploration geophysics*. Society of Exploration Geophysicists, pp. M1–1.

Bradshaw, John, Stefan Bachu, Didier Bonijoly, Robert Burruss, Sam Holloway, Niels Peter Christensen and Odd Magne Mathiassen (2007). 'CO2 storage capacity estimation: issues and development of standards'. In: *International journal of greenhouse gas control* 1.1, pp. 62–68.

Brennan, Sean T, Robert C Burruss, Matthew D Merrill, Philip A Freeman and Leslie F Ruppert (2010). 'A probabilistic assessment methodology for the evaluation of geologic carbon dioxide storage'. In: *US Geological Survey Open-File Report* 1127.2010, p. 31.

Brown, Alistair R (2011). *Interpretation of three-dimensional seismic data*. Society of Exploration Geophysicists and American Association of Petroleum ...

Carcione, José M, Stefano Picotti, Davide Gei and Giuliana Rossi (2006). 'Physics and seismic modeling for monitoring CO2 storage'. In: *Pure and Applied Geophysics* 163.1, pp. 175–207.

Carman, Philip Crosbie (1961). *L'écoulement des gaz à travers les milieux poreux*. Institut national des sciences et techniques nucléaires.

Chadwick, Andy, Rob Arts, Christian Bernstone, Franz May, Sylvain Thibeau and Peter Zweigel (2008). *Best practice for the storage of CO2 in saline aquifers-observations and guidelines from the SACS and CO2STORE projects*. Vol. 14. British Geological Survey.

Chadwick, Andy, Gareth Williams, Nicolas Delepine, Vincent Clochard, Karine Labat, Susan Sturton, Maike-L Buddensiek, Menno Dillen, Michael Nickel, Anne Louise Lima et al. (2010). 'Quantitative analysis of time-lapse seismic monitoring data at the Sleipner CO 2 storage operation'. In: *The Leading Edge* 29.2, pp. 170–177.

Christensen, NP and S Holloway (2003). 'Geological storage of CO2 from combustion of fossil fuel. Summary report of the GESTCO project. Geological Survey of Denmark and Greenland'. In: *British Geological Survey*.

Ciotta, Mariana, Drielli Peyerl, Ligia Barrozo, Lucy Sant Anna, Edmilson Moutinho dos Santos, Célio Bermann, Carlos Grohmann, Evandro Mateus Moretto and Colombo Tassinari (2020). 'An overview of carbon capture and storage atlases around the world'. In: *Environmental Geosciences* 27.1, pp. 1–8.

CO2 Storage Data Consortium (Jan. 2020). *CO2 DataShare portal*. Ed. by co2datashare.org. URL: https://co2datashare.org/about.

Den Norske Stats Oljeselskap AS (1984). *APPRAISAL Well Report 31/6-6*. URL: https://factpages.npd.no/nb-no/wellbore/pageview/exploration/all/127.

Doyen, Philippe M (1988). 'Porosity from seismic data: A geostatistical approach'. In: *Geophysics* 53.10, pp. 1263–1275.

Dupuy, Bastien, Anouar Romdhane, Peder Eliasson, Etor Querendez, Hong Yan, Verónica A Torres and Amir Ghaderi (2017). 'Quantitative seismic characterization of CO2 at the Sleipner storage site, North Sea'. In: *Interpretation* 5.4, SS23–SS42.

Dupuy, Bastien, Verónica Torres, Anouar Romdhane and Amir Ghaderi (2018). 'Norwegian large-scale CO2 storage project (Smeaheia): baseline geophysical models'. In: *14th Greenhouse Gas Control Technologies Conference Melbourne*, pp. 21–26.

Dvorkin, Jack and Salman Alkhater (2004). 'Pore fluid and porosity mapping from seismic'. In: *first break* 22.2.

Dvorkin, Jack, Gary Mavko and Boris Gurevich (2007). 'Fluid substitution in shaley sediment using effective porosity'. In: *Geophysics* 72.3, O1–O8.

Dvorkin, Jack and Amos Nur (1996). 'Elasticity of high-porosity sandstones: Theory for two North Sea data sets'. In: *Geophysics* 61.5, pp. 1363–1370.

Eiken, Ola, I Brevik, R Arts, E Lindeberg and K Fagervik (2000). 'Seismic monitoring of CO2 injected into a marine acquifer'. In: *SEG Technical Program Expanded Abstracts 2000*. Society of Exploration Geophysicists, pp. 1623–1626.

Eiken, Ola, Philip Ringrose, Christian Hermanrud, Bamshad Nazarian, Tore A Torp and Lars Høier (2011). 'Lessons learned from 14 years of CCS operations: Sleipner, In Salah and Snøhvit'. In: *Energy procedia* 4, pp. 5541–5548.

Ellis, Darwin V and Julian M Singer (2007). *Well logging for earth scientists*. Vol. 692. Springer.

Engelenburg, BCW van and K Blok (1991). 'Prospects for the Disposal of Carbon Dioxide in Aquifers. Dept. of Science'. In: *Technology and Society, University of Utrecht*.

Equinor (Apr. 2022). *Equinor awarded the Smeaheia and Polaris CO2 licenses*. Ed. by equinor.com. [Online; posted 05-April-2022]. URL: https://www.equinor.com/en/news/20220405-awarded-smeaheia-polaris-co2-licenses.html.

Fawad, Manzar, MD Jamilur Rahman and Nazmul Haque Mondol (2021). 'Seismic reservoir characterization of potential CO2 storage reservoir sandstones in Smeaheia area, Northern North Sea'. In: *Journal of Petroleum Science and Engineering* 205, p. 108812.

Funnell, R, P King, S Edbrooke, K Bland and B Field (2008). 'Opportunities for underground geological storage of CO2 in New Zealand-Report CCS-08/1–Waikato and onshore Taranaki overview'. In: *GNS Science Report* 53, p. 70.

Gammer, D, A Green, S Holloway and G Smith (2011). 'The Energy Technologies Institute's UK CO2 storage appraisal project (UKSAP)'. In: *SPE Offshore Europe Oil and Gas Conference and Exhibition*. OnePetro.

Gassmann, Fritz (1951). 'Elastic waves through a packing of spheres'. In: *Geophysics* 16.4, pp. 673–685.

Gassnova (2022). *CO2 transport and storage: Northern Lights project*. Ed. by ccsnorway.com. [Online; accessed 08-April-2022]. URL: https://ccsnorway.com/transport-storage-northern-lights/.

GCCSI (2020). *Global status of CCS 2020*. Tech. rep. Global CCS Institute.

GCCSI (2021a). *Global status of CCS 2021*. Tech. rep. Global CCS Institute.

GCCSI (2021b). 'Technology readiness and costs of CCS'. In: *Global CCS Institute, Brussels, Belgium*.

GCCSI (Apr. 2022). *CO2RE*. Ed. by Global CCS Institute. [Online; posted 08-April-2022]. URL: https://co2re.co/.

GHG, IEA (2009). *Development of Storage Coefficients for CO2 Storage in Deep Saline Formations; 2009/13*.

Glover, Paul WJ (2000). 'Petrophysics'. In: *University of Aberdeen, UK*.

Glover, Paul WJ (2001). 'Formation Evaluation'. In: *MSc Course Notes*.

GN1101 Dataset (2011). *Seismic 3D surveys - CO2 datashare*. URL: https://co2datashare.org/dataset/smeaheia-dataset/resource/705d84fe-3054-4ab4-951b-c045782078fb.

Goodman, Angela, Alexandra Hakala, Grant Bromhal, Dawn Deel, Traci Rodosta, Scott Frailey, Mitchell Small, Doug Allen, Vyacheslav Romanov, Jim Fazio et al. (2011). 'US DOE methodology for the development of geologic storage potential for carbon dioxide at the national and regional scale'. In: *International Journal of Greenhouse Gas Control* 5.4, pp. 952–965.

Goodman, Angela, Sean Sanguinito and Jonathan S Levine (2016). 'Prospective CO2 saline resource estimation methodology: Refinement of existing US-DOE-NETL methods based on data availability'. In: *International Journal of Greenhouse Gas Control* 54, pp. 242–249.

Greenberg, ML and JP Castagna (1992). 'Shear-wave velocity estimation in porous rocks: theoretical formulation, preliminary verification and applications1'. In: *Geophysical prospecting* 40.2, pp. 195–209.

Guidish, Thomas and Marc De Buyl (1987). 'Well calibration of seismically derived petrophysical parameters: A sensitivity analysis'. In: *SEG Technical Program Expanded Abstracts 1987*. Society of Exploration Geophysicists, pp. 386–390.

Halland, IT Gjeldvik, WT Johansen, C Magnus, IM Meling, S Pedersen, F Riis, T Solbakk and I Tappel (2011). 'CO2 Storage Atlas Norwegian North Sea'. In: *Norwegian Petroleum Directorate, PO Box* 600.

Halland, Mujezinovic and Riis (2014). 'CO2 Storage Atlas: Norwegian Continental Shelf, Norwegian Petroleum Directorate, PO Box 600, NO-4003 Stavanger, Norway, 2014'. In: *URL http://www. npd. no/en/Publications/Reports/Compiled-CO2-atlas*.

Halland and Riis (2018). 'Characterization and Classification of CO2 storage sites on the Norwegian Continental Shelf'. In: *14th Greenhouse Gas Control Technologies Conference Melbourne*, pp. 21–26.

Hampson, D and B Russell (1999). 'STRATA theory'. In: *Hampson-Russell Software Services*.

Hjelm, Lars, Karen Lyng Anthonsen, Knud Dideriksen, Carsten Møller Nielsen, Lars Henrik Nielsen and Anders Mathiesen (2020). *Capture, Storage and Use of CO2 (CCUS)*. Tech. rep.

Holgate, Nicholas E, Christopher A-L Jackson, Gary J Hampson and Tom Dreyer (2013). 'Sedimentology and sequence stratigraphy of the middle–upper jurassic krossfjord and fensfjord formations, Troll Field, northern North Sea'. In: *Petroleum Geoscience* 19.3, pp. 237–258.

Holt, T, J-I Jensen and E Lindeberg (1995). 'Underground storage of CO2 in aquifers and oil reservoirs'. In: *Energy Conversion and Management* 36.6-9, pp. 535–538.

IEA (2021). *Net Zero by 2050: A Roadmap for the Global Energy Sector*. URL: `https://www.iea.org/reports/net-zero-by-2050`.

IPCC (2005). 'Carbon Dioxide Capture and Storage'. In: *Cambridge University Press*.

IPCC (2018). *Global warming of 1.5° C: an IPCC special report on the impacts of global warming of 1.5° C above pre-industrial levels and related global greenhouse gas emission pathways, in the context of strengthening the global response to the threat of climate change, sustainable development, and efforts to eradicate poverty*. Intergovernmental Panel on Climate Change.

IPCC (2022a). *Climate Change 2022: Impacts, Adaptation, and Vulnerability. Contribution of Working Group II to the Sixth Assessment Report of the Intergovernmental Panel on Climate Change*. Ed. by D.C. Roberts H.-O. Pörtner, E.S. Poloczanska M. Tignor, A. Alegría K. Mintenbeck, S. Langsdorf M. Craig, V. Möller S. Löschke and B. Rama (eds.) A. Okem. Cambridge University Press, Cambridge, UK and New York, NY, USA.

IPCC (2022b). *Summary for Policymakers. In: Climate Change 2022: Mitigation of Climate Change. Contribution of Working Group III to the Sixth Assessment Report of the Intergovernmental Panel on Climate Change*. Ed. by P.R. Shukla, R. Slade J. Skea, R. van Diemen A. Al Khourdajie, M. Pathak D. McCollum, P. Vyas S. Some, M. Belkacemi R. Fradera, G. Lisboa A. Hasija and J. Malley S. Luz. Cambridge University Press, Cambridge, UK and New York, NY, USA.

Kaufman, Roland and Sarah E. Gasda (2018). 'Large-scale CO2 storage in Smeaheia'. In: *FME SUCCESS Synthesis report Volume 8*.

La Vigne, Jack, Mike Herron and Russ Hertzog (1994). 'Density-neutron interpretation in shaly sands'. In: *SPWLA 35th Annual Logging Symposium*. OnePetro.

Lauritsen, H, S Kassold, R Meneguolo and A Furre (2018). 'Assessing potential influence of nearby hydrocarbon production on CO2 storage at Smeaheia'. In: *Fifth CO2 Geological Storage Workshop*. Vol. 2018. 1. European Association of Geoscientists & Engineers, pp. 1–5.

Lindeberg, Erik (1997). 'Escape of CO2 from aquifers'. In: *Energy conversion and management* 38, S235–S240.

Lindeberg, Erik, Peter Zweigel, Per Bergmo, Amir Ghaderi and Ane Lothe (2001). 'Prediction of CO2 distribution pattern improved by geology and reservoir simulation and verified by time lapse seismic'. In: *Greenhouse gas control technologies* 372, p. 377.

Lindseth, Roy O (1979). 'Synthetic sonic logs—A process for stratigraphic interpretation'. In: *Geophysics* 44.1, pp. 3–26.

Liner, Christopher L (1999). 'Treatise of Petroleum Geology/Handbook of Petroleum Geology: Exploring for Oil and Gas Traps. Chapter 12: Interpreting Seismic Data'. In.

Lloyd, Christopher, Mads Huuse, Bonita J Barrett and Andrew MW Newton (2021). 'A Workflow for Regional Exploration of Co2 Storage Sites in Saline'. In: *TCCS–11. CO2 Capture, Transport and Storage. Trondheim 22nd–23rd June 2021. Short Papers from the 11th International Trondheim CCS Conference*. SINTEF Academic Press.

Lothe, AE and P Zweigel (1999). *Saline Aquifer CO2 Storage (SACS). Informal annual report 1999 of SINTEF Petroleum Research's results in work area 1 'Reservoir Geology'*. Tech. rep. SINTEF Petroleum Research report 23.4300. 00/03/99, 54 p. Restricted.

Lothe, Ane, Per Eirik Bergmo and Alv-Arne Grimstad (2019). 'Storage resources for future European CCS deployment; A roadmap for a Horda CO2 storage hub, offshore Norway'. In.

Lothe, Ane E, Per Eirik Strand Bergmo, Benjamin Emmel and Peder Eliasson (2018). 'Effects of uncertainties in fault interpretations on pressure depletion and CO2 storage injection at Horda Platform, offshore Norway'. In: *14th Greenhouse Gas Control Technologies Conference Melbourne*, pp. 21–26.

Lumley, David (2010). '4D seismic monitoring of CO 2 sequestration'. In: *The Leading Edge* 29.2, pp. 150–155.

Lumley, David (2019). 'The Role of Geophysics in Carbon Capture'. In: *Geophysics and Geosequestration*, p. 12.

Martin, MA and CJ Lowrey (1997). *Sedimentology and petrography of the Upper Jurassic cored interval from well N32/4-1*. URL: https://co2datashare.org/dataset/smeaheia-dataset/resource/8e606949-dd4f-41d9-8ba3-a80a9983b588.

Maureau, GTFR and DH Van Wijhe (1979). 'The prediction of porosity in the Permian (Zechstein 2) carbonate of eastern Netherlands using seismic data'. In: *Geophysics* 44.9, pp. 1502–1517.

Mavko, Gary, Tapan Mukerji and Jack Dvorkin (2020). *The rock physics handbook*. Cambridge university press.

McDonald, Andy (2021a). *Creating Scatterplots (Crossplots) of Well Log Data*. https://github.com/andymcdgeo/Andys_YouTube_Notebooks/blob/main/03%20-%20Log%20Data%20Visualisation%20-%20Scatterplots-Crossplots.ipynb.

McDonald, Andy (2021b). *Petrophysics-Python-Series - Working With LASIO*. https://github.com/andymcdgeo/Petrophysics-Python-Series/blob/master/07%20-%20Working%20With%20LASIO.ipynb.

Ministry of Petroleum and Energy (Sept. 2021). *Announcement of areas related to CO2 storage*. Ed. by government.no. [Online; posted 10-September-2021]. URL: https://www.regjeringen.no/en/historical-archive/solbergs-government/Ministries/oed/press-releases/2021/announcement-of-areas-related-to-co2-storage/id2871068/.

Ministry of Petroleum and Energy (Apr. 2022). *Two licenses under the carbon storage regulations awarded on the NCS*. Ed. by government.no. [Online; posted 06-April-2022]. URL: https://www.regjeringen.no/en/aktuelt/two-licenses-under-the-carbon-storage-regulations-awarded-on-the-ncs/id2907318/.

Miri, R and H Hellevang (2018). 'Critical Factors for Considering CO2 Injectivity in Saline Aquifers'. In: *Bergen, Norway: FME SUCCESS*.

Mishra, Srikanta, Mark Kelley, Evan Zeller, Nick Slee, Neeraj Gupta, Indrajit Bhattacharya and Mike Hammond (2013). 'Maximizing the value of pressure monitoring data from CO2 sequestration projects'. In: *Energy Procedia* 37, pp. 4155–4165.

Næss, Gjermund (2021). 'Seismic time- lapse response from CO2 injection in two North Sea reservoirs'. Unpublished specialization project report.

Nordbotten, Jan Martin, Michael A Celia and Stefan Bachu (2005). 'Injection and storage of CO2 in deep saline aquifers: Analytical solution for CO2 plume evolution during injection'. In: *Transport in Porous media* 58.3, pp. 339–360.

Norsk Hydro Produksjon AS (2004). *WILDCAT Well Report 31/6-3*. URL: https://factpages.npd.no/nb-no/wellbore/pageview/exploration/all/35.

Okwen, Roland T, Mark T Stewart and Jeffrey A Cunningham (2010). 'Analytical solution for estimating storage efficiency of geologic sequestration of CO2'. In: *International Journal of Greenhouse Gas Control* 4.1, pp. 102–107.

Oljedirektoratet (2022). *KROSSFJORD FM*. URL: https://factpages.npd.no/nb-no/strat/pageview/litho/formations/87 (visited on 08/04/2022).

Petroleum, Norwegian Ministry of and Energy (2020). 'Longship - Carbon capture and storage'. In: *Meld.St. 33 (2019-2020) Report to the Storting (white paper)*. URL: https://www.regjeringen.no/en/dokumenter/meld.-st.-33-20192020/id2765361/.

Philips Petroleum Company (1997). *Final Well Report 32/4-1*. URL: https://factpages.npd.no/nb-no/wellbore/pageview/exploration/all/2918.

Rasmussen, KB and KG Maver (1996). 'Direct inversion for porosity of post stack seismic data'. In: *European 3-D Reservoir Modelling Conference*. OnePetro.

Richards, Paul G and Keiiti Aki (1980). *Quantitative seismology: theory and methods*. Vol. 842. Freeman San Francisco, CA.

Riis, F, N Pedersen, MA Birkeland et al. (2017). 'Troll Area, Norwegian North Sea: Case Study of CO2 Storage Sites in an Aquifer Under Depletion. Presentation at AAPG'. In: *SEG International Conference and Exhibition, London, England*.

Riis and Halland (2014). 'CO2 Storage Atlas of the Norwegian Continental Shelf: Methods Used to Evaluate Capacity and Maturity of the CO2 Storage Potential.' In: *Energy Procedia* 63, pp. 5258–5265.

Ringrose, Philip (2020). *How to store CO2 underground: Insights from early-mover CCS Projects*. Springer.

Ross, Espen Erichsen, Gemma Kearney Kari Lise Rørvik and Kirsten Haaberg (2013). 'Troll kystnær subsurface evaluation report'. In: URL: https://co2datashare.org/view/license/26af9426-203f-4993-9d41-2e1bf191ceaf.

Russell, B and D Hampson (1991). 'Comparison of poststack seismic inversion methods'. In: *SEG Technical Program Expanded Abstracts 1991*. Society of Exploration Geophysicists, pp. 876–878.

Simm, Rob and Mike Bacon (2014). *Seismic Amplitude: An interpreter's handbook*. Cambridge University Press.

SMEAHEIA DATASET LICENSE (2022). Equinor, Gassnova. URL: https://co2datashare.org/view/license/26af9426-203f-4993-9d41-2e1bf191ceaf.

Span, Roland and Wolfgang Wagner (1996). 'A new equation of state for carbon dioxide covering the fluid region from the triple-point temperature to 1100 K at pressures up to 800 MPa'. In: *Journal of physical and chemical reference data* 25.6, pp. 1509–1596.

Statoil (2016). 'Selected extracts from Statoil internal report on Subsurface Evaluation of Smeaheia as part of 2016 Feasibility study on CO2 storage in the Norwegian Continental shelf'. In: No. OED 15/1785. URL: https://co2datashare.org/view/license/26af9426-203f-4993-9d41-2e1bf191ceaf.

Statoil AS (1984). *Routine Core Analysis, Well 31/6-6*. 20084400004. URL: https://factpages.npd.no/pbl/wellbore_documents/127_04_31_6_6_Routine_core_analyses.pdf.

Sundal, Anja, Helge Hellevang, Rohaldin Miri, Henning Dypvik, Johan Petter Nystuen and Per Aagaard (2014). 'Variations in mineralization potential for CO2 related to sedimentary facies and burial depth–a comparative study from the North Sea'. In: *Energy Procedia* 63, pp. 5063–5070.

Talisman Energy (2008). *Trow 32/2-1 END OF WELL REPORT*. URL: https://co2datashare.org/dataset/smeaheia-dataset/resource/8e606949-dd4f-41d9-8ba3-a80a9983b588.

Timoshenko, SP and JN Goodier (1934). *Theory of Elasticity (1970 printing)*.

UN (Dec. 2015). 'Paris Agreement'. In: URL: https://treaties.un.org/pages/ViewDetails.aspx?src=TREATY&mtdsg_no=XXVII-7-d&chapter=27&clang=_en.

Valle, LM, C Grima, R Rodriguez and C Llopis (2020). 'Effect of scCO2-brine mixture on injectivity and storage capacity in rock samples of naturally fractured carbonate formations'. In: *Journal of Natural Gas Science and Engineering* 81, p. 103452.

Valluri, Manoj, Srikanta Mishra and Priya Ravi Ganesh (2021). 'Injectivity index: a powerful tool for characterizing CO2 storage reservoirs—a technical note'. In: *Greenhouse Gases: Science and Technology* 11.2, pp. 251–265.

Van der Meer, LGH (1992). 'Investigations regarding the storage of carbon dioxide in aquifers in the Netherlands'. In: *Energy Conversion and management* 33.5-8, pp. 611–618.

Vangkilde-Pedersen, Thomas, Karen Lyng Anthonsen, Nikki Smith, Karen Kirk, Bert van der Meer, Yann Le Gallo, Dan Bossie-Codreanu, Adam Wojcicki, Yves-Michel Le Nindre, Chris Hendriks et al. (2009). 'Assessing European capacity for geological storage of carbon dioxide–the EU GeoCapacity project'. In: *Energy Procedia* 1.1, pp. 2663–2670.

Veeken, PCH, Da Silva and M (2004). 'Seismic inversion methods and some of their constraints'. In: *First break* 22.6.

Wang, Yang, Keni Zhang and Nengyou Wu (2013). 'Numerical investigation of the storage efficiency factor for CO2 geological sequestration in saline formations'. In: *Energy Procedia* 37, pp. 5267–5274.

Wang, Yanghua (2015). 'Frequencies of the Ricker wavelet'. In: *Geophysics* 80.2, A31–A37.

Wang, Zhijing (2001). 'Fundamentals of seismic rock physics'. In: *Geophysics* 66.2, pp. 398–412.

Wu, Tao and Robert R Berg (2003). 'Relationship of reservoir properties for shaly sandstones based on effective porosity'. In: *Petrophysics-The SPWLA Journal of Formation Evaluation and Reservoir Description* 44.05.

Zhang, Jincai (2011). 'Pore pressure prediction from well logs: Methods, modifications, and new approaches'. In: *Earth-Science Reviews* 108.1-2, pp. 50–63.

Zweigel, P, M Hamborg, R Arts, A Lothe, Ø Sylta and A Tømmerås (2000). 'Prediction of migration of CO2 injected into an underground depository: reservoir geology and migration modelling in the Sleipner case (North Sea)'. In: *5th International Conference on Greenhouse Gas Control Technologies, Cairns (Australia)*.

Appendix A

Well data

Wells	**32/4-1**	**32/2-1**
$\rho_{matrix}(g/cm^3)$	2.65	2.65
$\rho_{clay}(g/cm^3)$	2.7	2.7
$\rho_{fluid}(g/cm^3)$	1.07	1.07
GR min (gAPI)	65	55
GR max (gAPI)	140	105

Table A.1: Key parameters for the petrophysical calculations of Sognefjord Fm, Fensfjord Fm and Krossfjord Fm.

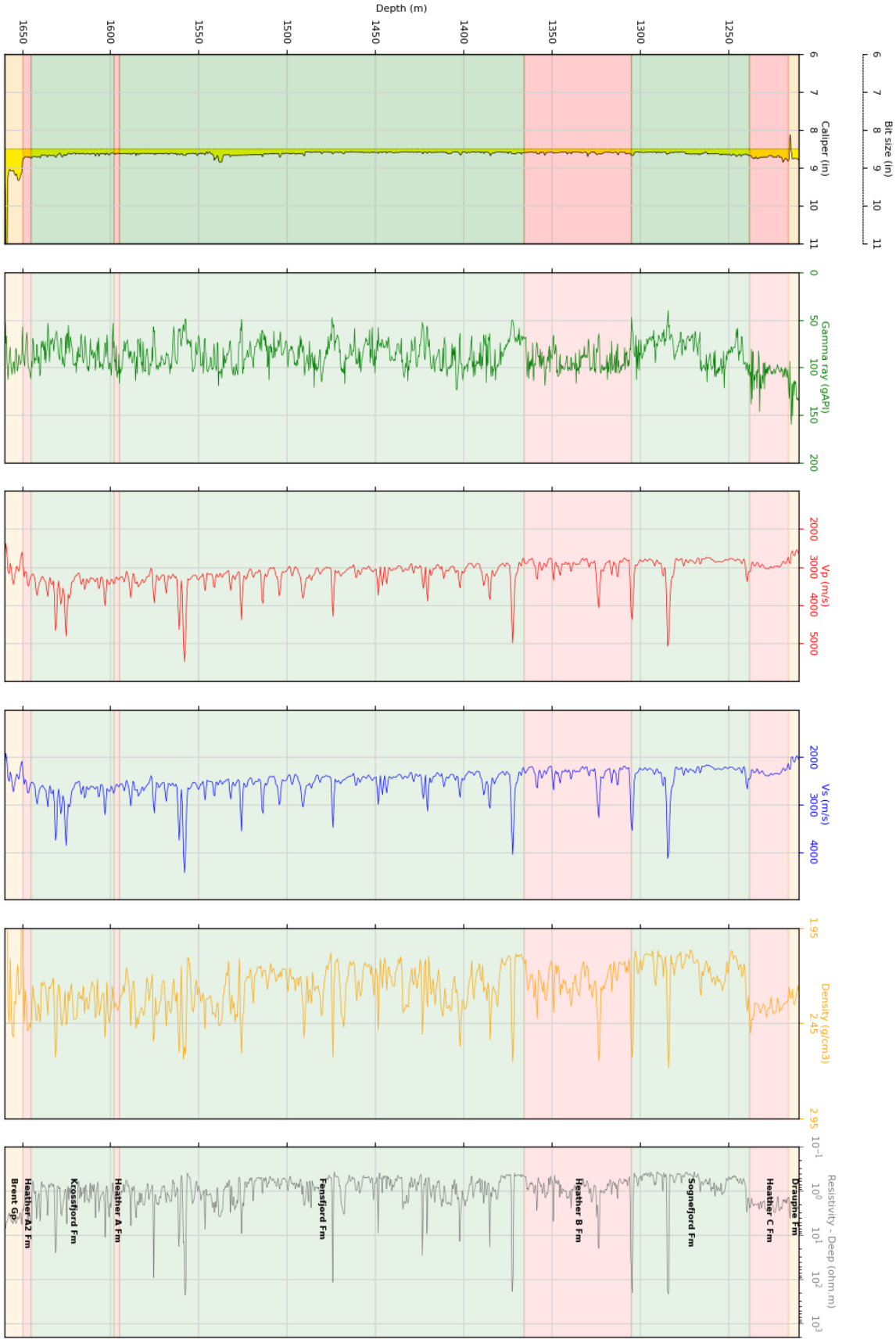

Figure A.1: Well panel for well 32/4-1.

Figure A.2: Calculated well panel for well 32/4-1.

Figure A.3: Well panel for well 32/2-1.

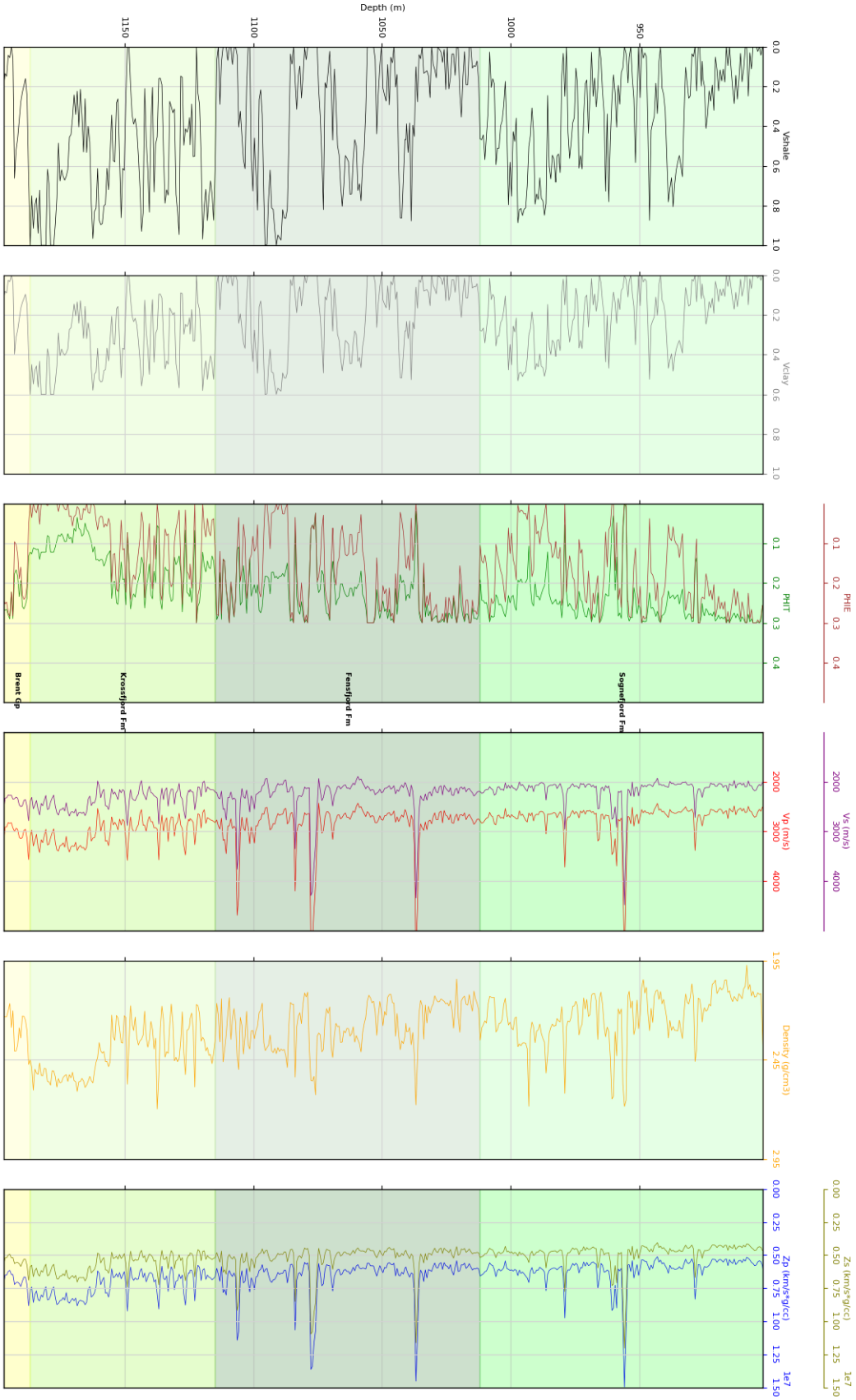

Figure A.4: Calculated well panel for well 32/2-1.

Appendix B

Cross-plots

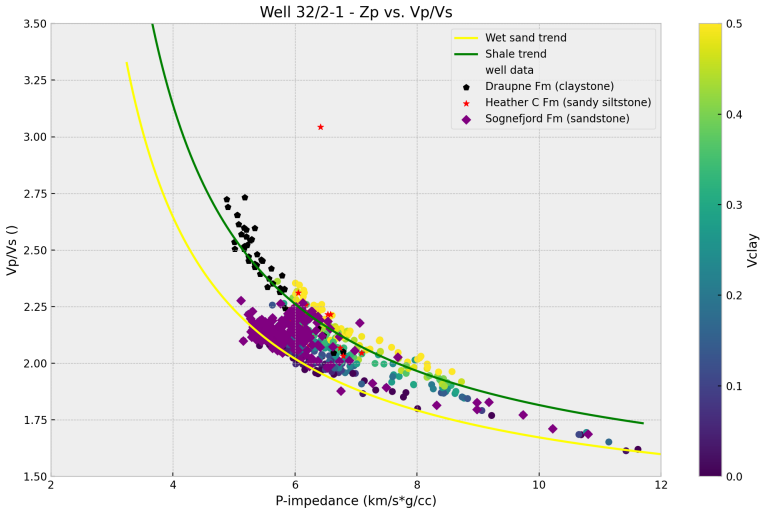

Figure B.1: Vp/Vs is plotted against P-impedance, with the wet sand and shale trend lines.

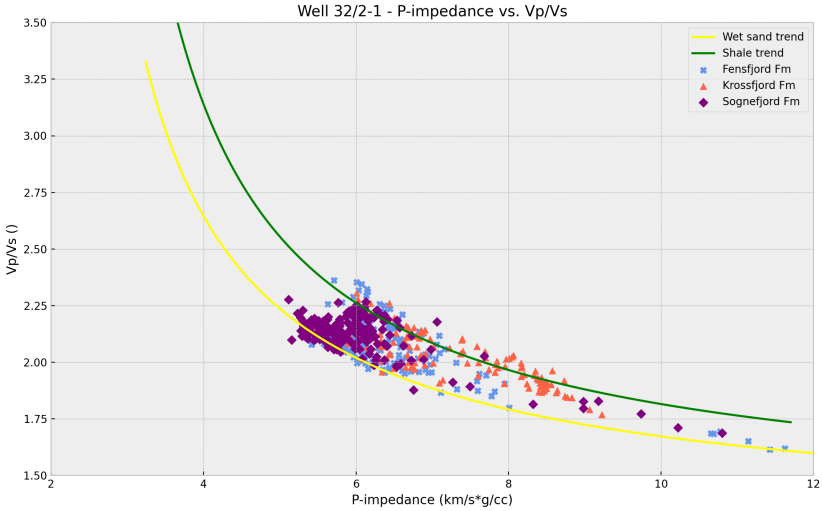

Figure B.2: Vp/Vs is plotted against P-impedance, with the wet sand and shale trend lines, for the formations.

Appendix C

Porosity maps

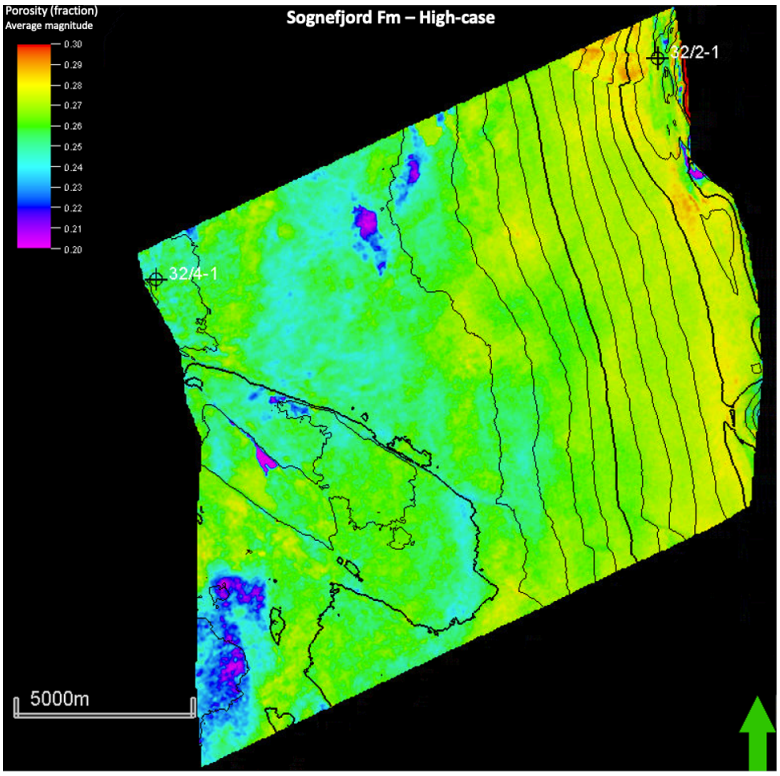

Figure C.1: Map view of the average magnitude value of the porosity for Sognefjord Fm high-case interval within the inverted high estimated porosity volume.

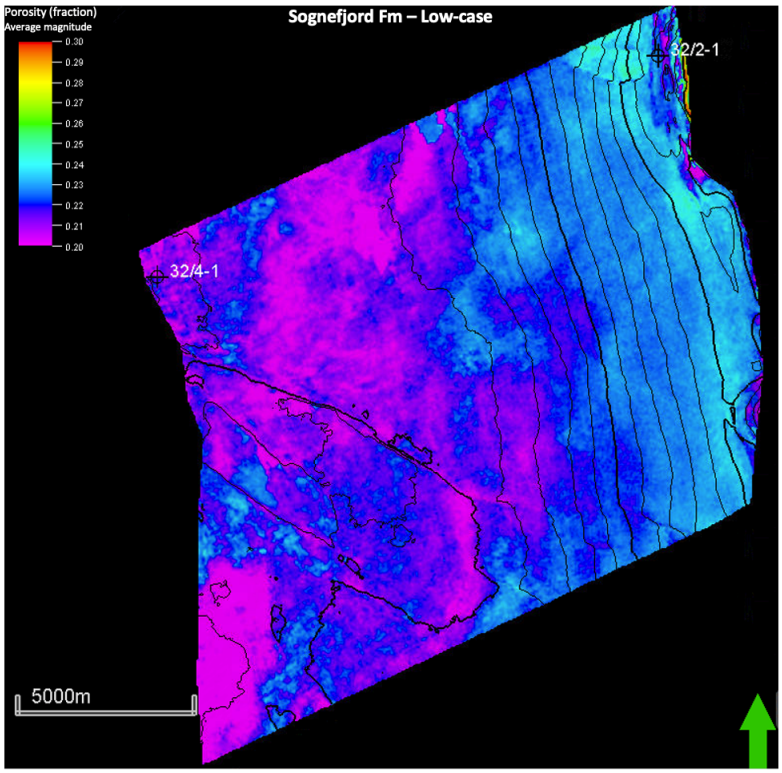

Figure C.2: Map view of the average magnitude value of the porosity for Sognefjord Fm low-case interval within the inverted low estimated porosity volume.

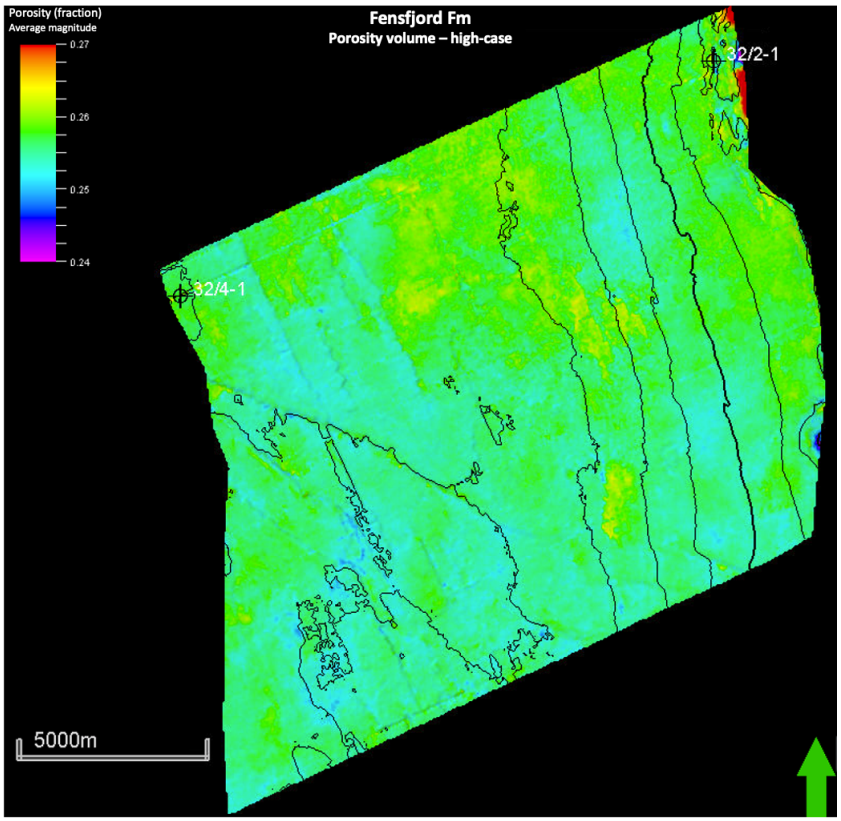

Figure C.3: Map view of the average magnitude value of the porosity for Fensfjord Fm high-case interval within the inverted porosity volume.

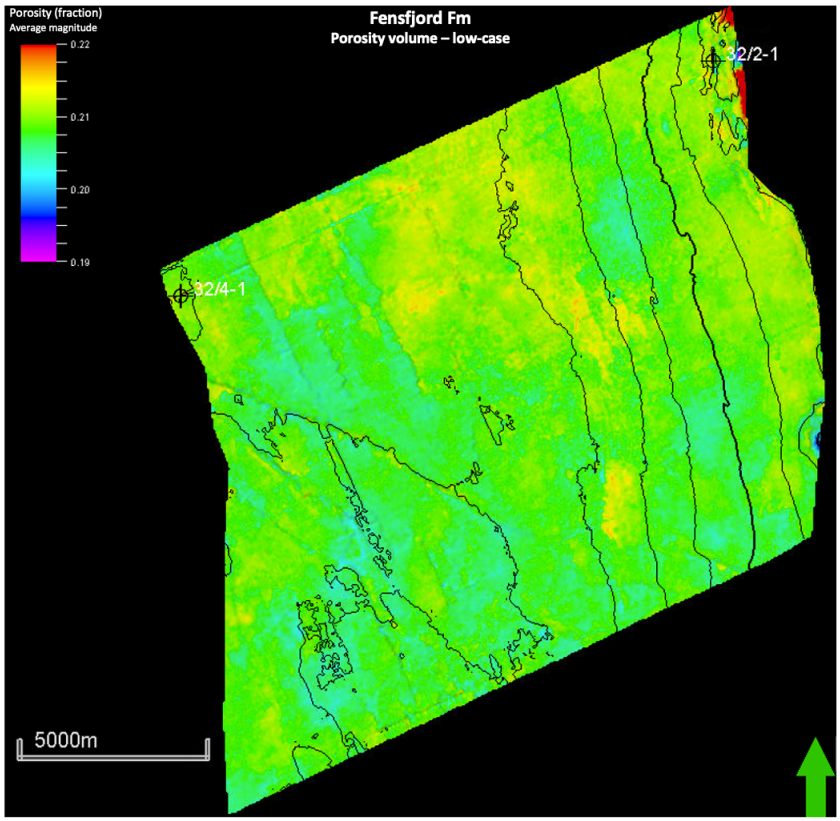

Figure C.4: Map view of the average magnitude value of the porosity for Fensfjord Fm low-case interval within the inverted porosity volume.

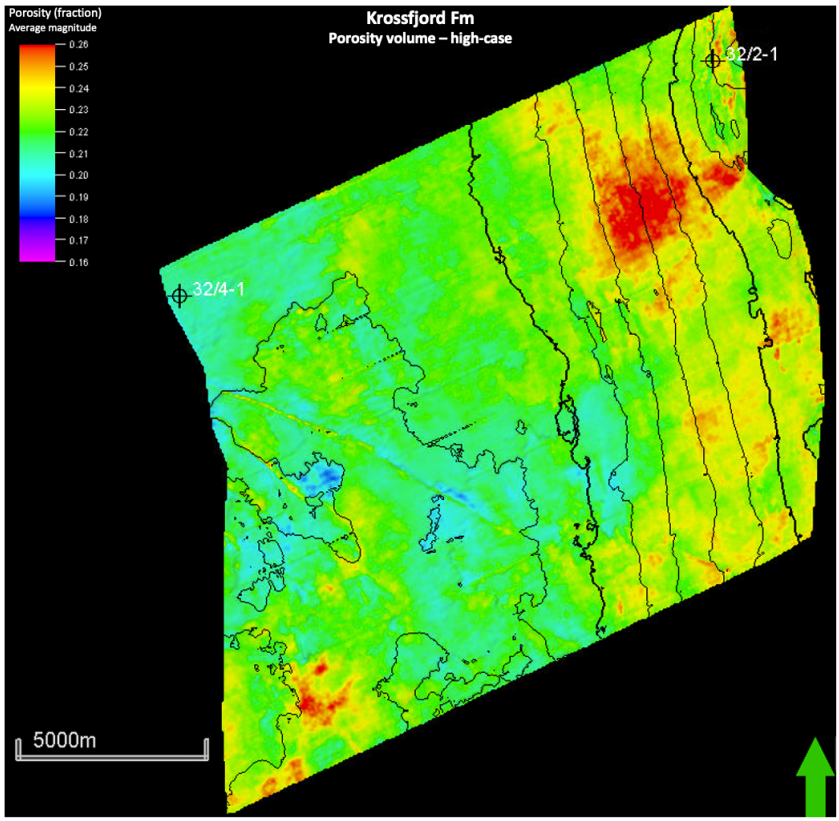

Figure C.5: Map view of the average magnitude value of the porosity for Krossfjord Fm high-case interval within the inverted porosity volume.

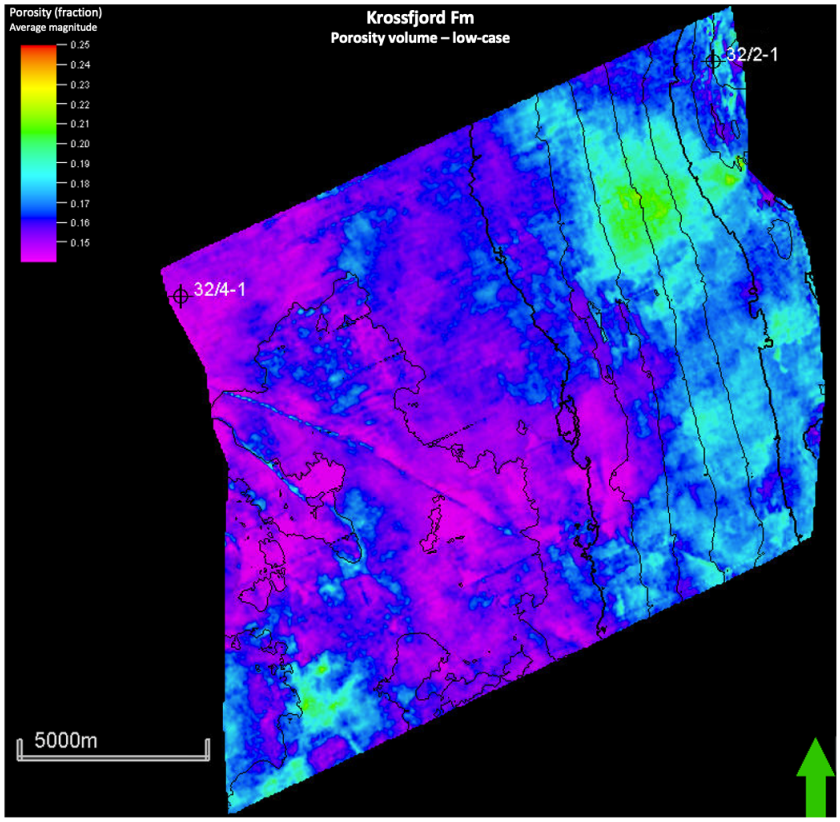

Figure C.6: Map view of the average magnitude value of the porosity for Krossfjord Fm low-case interval within the inverted porosity volume.

Appendix D

Permeability maps

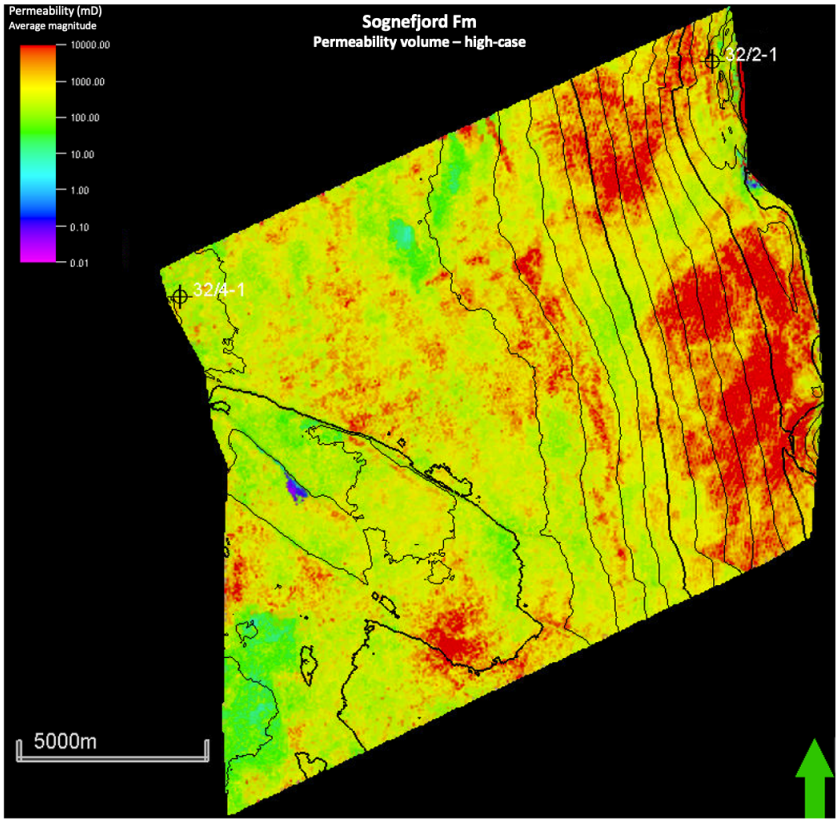

Figure D.1: Map view of the average magnitude value of the permeability for Sognefjord Fm high-case interval within the inverted permeability volume.

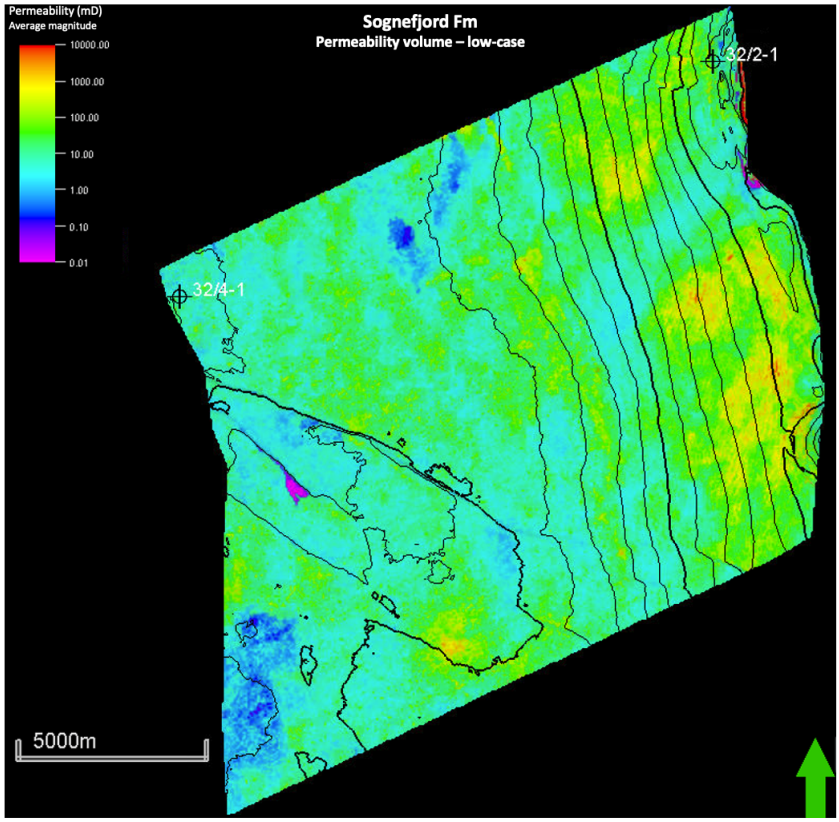

Figure D.2: Map view of the average magnitude value of the permeability for Sognefjord Fm low-case interval within the inverted permeability volume.

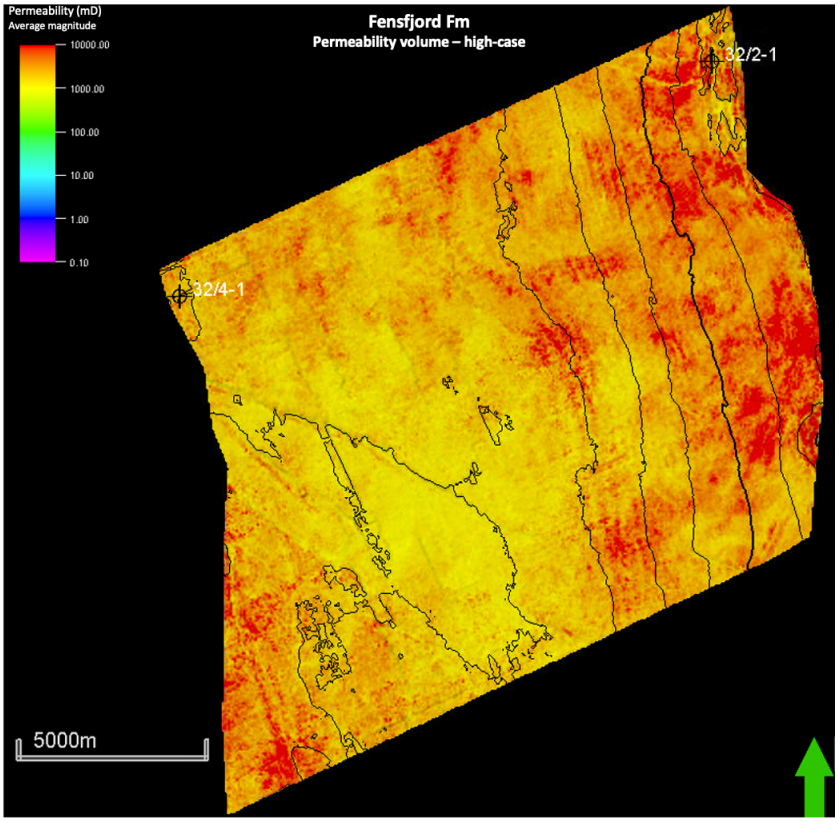

Figure D.3: Map view of the average magnitude value of the permeability for Fensfjord Fm high-case interval within the inverted permeability volume.

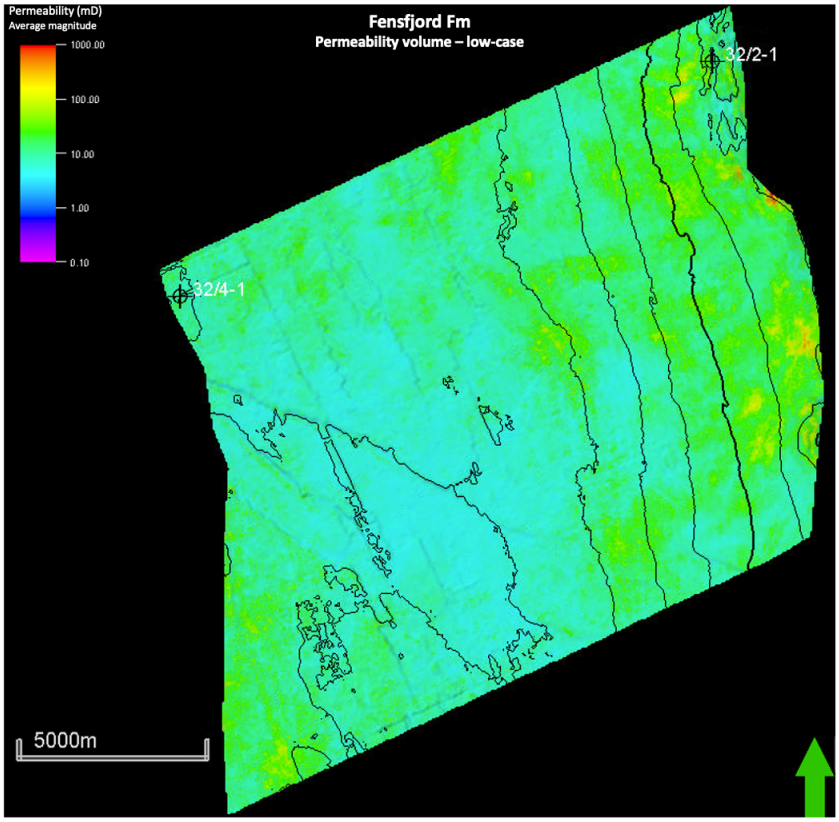

Figure D.4: Map view of the average magnitude value of the permeability for Fensfjord Fm low-case interval within the inverted permeability volume.

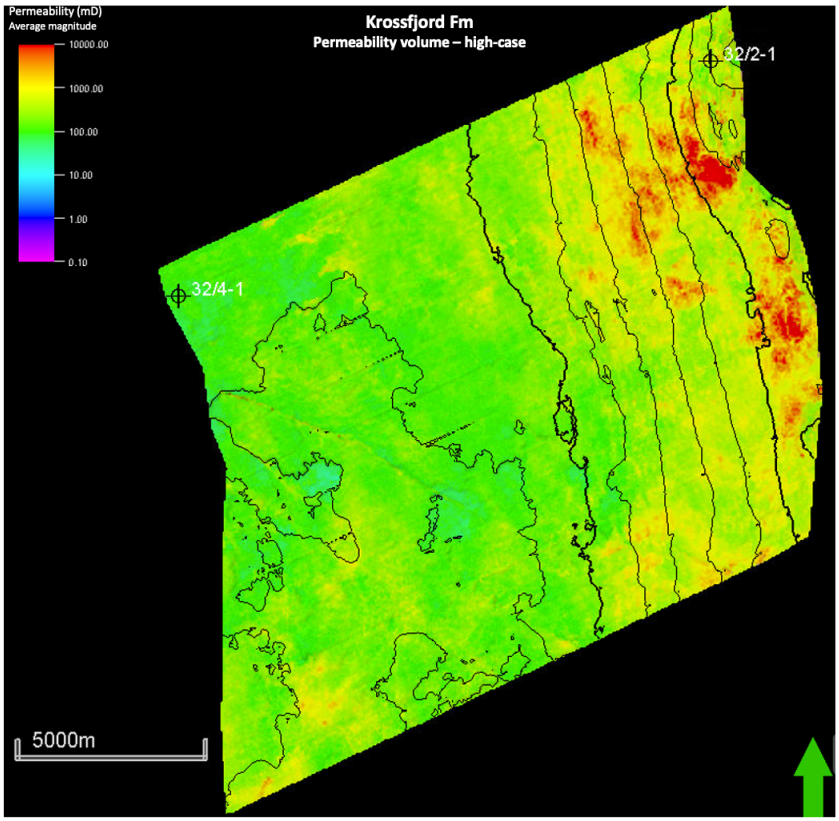

Figure D.5: Map view of the average magnitude value of the permeability for Krossfjord Fm high-case interval within the inverted permeability volume.

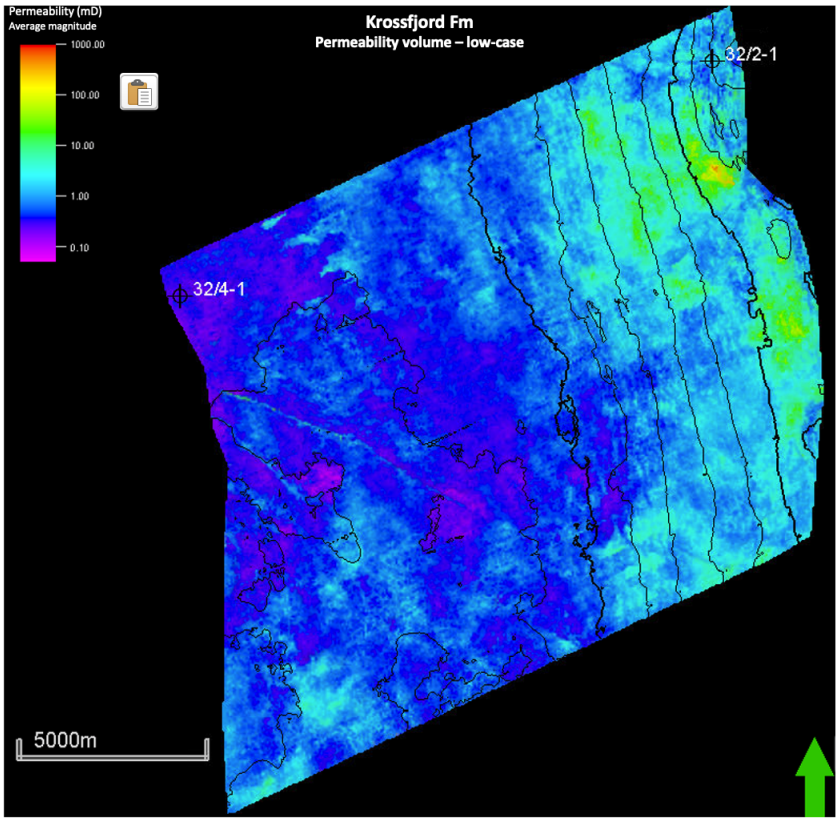

Figure D.6: Map view of the average magnitude value of the permeability for Krossfjord Fm low-case interval within the inverted permeability volume.

Appendix E

Code

E.1 Generation of well panels

The following script generates the well panels. McDonald (2021b) is used. The script for generation of well panel for well 32/4-1, fig. A.2, is listed in E.1 as a code example:

```
import pandas as pd
import matplotlib.pyplot as plt
import lasio
from decimate import decimate_logs
from scipy.interpolate import interp1d

las = lasio.read("32 4-1")
well = las.df()

font = {'size'   : 8}
plt.rc('font', **font)

well['PHID'] = (2.65-well['DEN'])/(2.65-1.07)
well['NEU'] = 2*well['PHIT'] - well['PHID']
well['VCLAY1'] = (well['NEU']-well['PHID']-(-0.025))/(0.42)
well['VSH'] = (well['GR']-65)/(140-65)
well['VCLAY2'] = well['VSH']*0.60

well['PHIE'] = (2.65-well['DEN'])/(2.65-1.07) - well['VCLAY2']*((2.65-2.7)
    /(2.65-1.07))
well['PHI_avg'] = (well['NEU']+well['PHID'])/2

#df_target1=well.loc[1238:1305].reset_index()
#x=df_target1.Vsand_D
#print(x.describe())
#y=df_target2.Vsand_HeatherC
#print(y.describe())

well['Vsonic1'] = well['HAC']/0.3048
```

```
well['Vp'] = 1e6/well['Vsonic1'] #(unit: m/s)
well['DEN2'] = well['DEN']*1000 #unit convert to kg/m3
well['Zp'] = well['Vp']*well['DEN2'] #(unit: (km/s*g/cc))
#Vs calculations from Greenberg-Castagna:
well['Vsand'] = 1-well['VSH']
well['Vs_sand'] = 0.80416*well['Vp'] - 0.85588
well['Vs_shale'] = 0.76969*well['Vp'] - 0.86735
well['Vs_arith'] = well['Vsand']*well['Vs_sand'] + well['VSH']*well['Vs_shale']
well['Vs_harm'] = 1/(well['Vsand']/well['Vs_sand'] + well['VSH']/well['Vs_shale'])
well['Vs'] = 0.5*(well['Vs_arith'] + well['Vs_harm'])
well['Zs'] = well['Vs']*well['DEN2'] #(unit: (km/s*g/cc))
#well['PHIE'] = well['PHIT'] - well['VSH']*((2.7-2.35)/(2.7-1.06))
well['P_ratio'] = 0.5*((well['Vp']/well['Vs'])*(well['Vp']/well['Vs'])-2)/((well['
    Vp']/well['Vs'])*(well['Vp']/well['Vs'])-1)

well_nan = well.notnull() * 1

# Create a dictionary of formations with a top and bottom depth
formations_dict = {"Draupne Fm": [1213, 1216],
              "Heather C Fm": [1216, 1238],
              "Sognefjord Fm": [1238, 1305],
              "Heather B Fm": [1305, 1366],
              "Fensfjord Fm": [1366, 1595],
              "Heather A Fm": [1595, 1598],
              "Krossfjord Fm": [1598, 1645],
              "Heather A2 Fm": [1645, 1650],
              "Brent Gp": [1650, 1660]}

formation_midpoints = []
for key, value in formations_dict.items():
    #Calculate mid point of the formation
    formation_midpoints.append(value[0] + (value[1]-value[0])/2)

formation_midpoints

# Select the same number of colours as there are formations
zone_colours = ["orange", "red", "green", "red", "green", "red", "green", "red", "
    orange"]

fig, ax = plt.subplots(figsize=(15,10))

#Set up the plot axes
ax1 = plt.subplot2grid((1,6), (0,0), rowspan=1, colspan = 1)
ax2 = plt.subplot2grid((1,6), (0,1), rowspan=1, colspan = 1, sharey = ax1)
ax3 = plt.subplot2grid((1,6), (0,2), rowspan=1, colspan = 1, sharey = ax1)
ax4 = ax3.twiny()
ax5 = plt.subplot2grid((1,6), (0,3), rowspan=1, colspan = 1, sharey = ax1)
ax6 = ax5.twiny()
ax7 = plt.subplot2grid((1,6), (0,4), rowspan=1, colspan = 1, sharey = ax1)
ax8 = plt.subplot2grid((1,6), (0,5), rowspan=1, colspan = 1, sharey = ax1)
ax9 = ax8.twiny()

# As our curve scales will be detached from the top of the track,
# this code adds the top border back in without dealing with splines
```

```
ax10 = ax1.twiny()
ax10.xaxis.set_visible(False)
ax11 = ax2.twiny()
ax11.xaxis.set_visible(False)
ax12 = ax3.twiny()
ax12.xaxis.set_visible(False)
ax13 = ax4.twiny()
ax13.xaxis.set_visible(False)
ax14 = ax5.twiny()
ax14.xaxis.set_visible(False)
ax15 = ax6.twiny()
ax15.xaxis.set_visible(False)
ax16 = ax7.twiny()
ax16.xaxis.set_visible(False)
ax17 = ax8.twiny()
ax17.xaxis.set_visible(False)
ax18 = ax9.twiny()
ax18.xaxis.set_visible(False)

# Vshale track
array_VSH = well['VSH'].to_numpy()
smooth_df = decimate_logs(array_VSH,4)
smooth_index = well.index[::4]
#ax1.plot(well['VSH'], well.index, color = "black", linewidth = 0.5)
ax1.plot(smooth_df, smooth_index, color = "black", linewidth = 0.5)
ax1.set_xlabel("Vshale")
ax1.set_xlim(0, 1)
ax1.set_ylabel("Depth (m)")
ax1.xaxis.label.set_color("black")
ax1.tick_params(axis='x', colors="black")
ax1.spines["top"].set_edgecolor("black")

# Vclay track
array_Vclay = well['VCLAY2'].to_numpy()
smooth_df = decimate_logs(array_Vclay,4)
smooth_index = well.index[::4]
ax2.plot(smooth_df, smooth_index, color = "gray", linewidth = 0.5)
#ax2.plot(well["VCLAY2"], well.index, color = "gray", linewidth = 0.5)
ax2.set_xlabel("Vclay")
ax2.set_xlim(0, 1)
#ax2.set_ylabel("Depth (m)")
ax2.xaxis.label.set_color("gray")
ax2.tick_params(axis='x', colors="gray")
ax2.spines["top"].set_edgecolor("gray")

# Total porosity track
array_phit = well['PHIT'].to_numpy()
smooth_df = decimate_logs(array_phit,10)
smooth_index = well.index[::10]
ax3.plot(smooth_df, smooth_index, color = "green", linewidth = 0.5)
#ax3.plot(well["PHIT"], well.index, color = "black", linewidth = 0.5)
ax3.set_xlabel("PHIT")
ax3.set_xlim(0.1, 0.5)
ax3.xaxis.label.set_color("green")
```

```
ax3.tick_params(axis='x', colors="green")
ax3.spines["top"].set_edgecolor("green")
#ax3.set_xticks([2000, 3000, 4000])

# Effective porosity track
array_phie = well['PHIE'].to_numpy()
smooth_df = decimate_logs(array_phie,10)
smooth_index = well.index[::10]
ax4.plot(smooth_df, smooth_index, color = "brown", linewidth = 0.5)
#ax4.plot(well["PHIE"], well.index, color = "black", linewidth = 0.5)
ax4.set_xlabel("PHIE")
ax4.set_xlim(0.1, 0.5)
ax4.xaxis.label.set_color("brown")
ax4.tick_params(axis='x', colors="brown")
ax4.spines["top"].set_position(("axes", 1.08))
ax4.spines["top"].set_visible(True)
ax4.spines["top"].set_edgecolor("brown")
#ax4.spines["top"].set_linestyle("dotted")
#ax4.set_xticks([2000, 3000, 4000])

# Vp track
array_vp = well['Vp'].to_numpy()
smooth_df = decimate_logs(array_vp,8)
smooth_index = well.index[::8]
ax5.plot(smooth_df, smooth_index, color = "red", linewidth = 0.5)
#ax5.plot(well["Vp"], well.index, color = "red", linewidth = 0.5)
ax5.set_xlabel("Vp (m/s)")
ax5.set_xlim(1000, 5000)
ax5.xaxis.label.set_color("red")
ax5.tick_params(axis='x', colors="red")
ax5.spines["top"].set_edgecolor("red")
ax5.set_xticks([2000, 3000, 4000])

# Vs track
array_vs = well['Vs'].to_numpy()
smooth_df = decimate_logs(array_vs,8)
smooth_index = well.index[::8]
ax6.plot(smooth_df, smooth_index, color = "purple", linewidth = 0.5)
#ax6.plot(well["Vs"], well.index, color = "purple", linewidth = 0.5)
ax6.set_xlabel("Vs (m/s)")
ax6.set_xlim(1000, 5000)
ax6.xaxis.label.set_color("purple")
ax6.tick_params(axis='x', colors="purple")
ax6.spines["top"].set_position(("axes", 1.08))
ax6.spines["top"].set_visible(True)
ax6.spines["top"].set_edgecolor("purple")
#ax6.spines["top"].set_linestyle("dotted")
ax6.set_xticks([2000, 3000, 4000])

# Density track
array_den = well['DEN'].to_numpy()
smooth_df = decimate_logs(array_den,8)
smooth_index = well.index[::8]
ax7.plot(smooth_df, smooth_index, color = "orange", linewidth = 0.5)
```

```
#ax7.plot(well["DEN"], well.index, color = "orange", linewidth = 0.5)
ax7.set_xlabel("Density (g/cm3)")
ax7.set_xlim(1.95, 2.95)
ax7.xaxis.label.set_color("orange")
ax7.tick_params(axis='x', colors="orange")
ax7.spines["top"].set_edgecolor("orange")
ax7.set_xticks([1.95, 2.45, 2.95])

# Zp track
array_zp = well['Zp'].to_numpy()
smooth_df = decimate_logs(array_zp,8)
smooth_index = well.index[::8]
ax8.plot(smooth_df, smooth_index, color = "blue", linewidth = 0.5)
#ax8.plot(well["Zp"], well.index, color = "blue", linewidth = 0.5)
ax8.set_xlabel("Zp (km/s*g/cc)")
ax8.set_xlim(0, 1.5*10000000)
ax8.xaxis.label.set_color("blue")
ax8.tick_params(axis='x', colors="blue")
ax8.spines["top"].set_edgecolor("blue")
#ax8.set_xticks([2000, 3000, 4000])

# Zs track
array_zs = well['Zs'].to_numpy()
smooth_df = decimate_logs(array_zs,8)
smooth_index = well.index[::8]
ax9.plot(smooth_df, smooth_index, color = "olive", linewidth = 0.5)
#ax9.plot(well["Zs"], well.index, color = "olive", linewidth = 0.5)
ax9.set_xlabel("Zs (km/s*g/cc)")
ax9.set_xlim(0, 1.5*10000000)
ax9.xaxis.label.set_color("olive")
ax9.tick_params(axis='x', colors="olive")
ax9.spines["top"].set_position(("axes", 1.08))
ax9.spines["top"].set_visible(True)
ax9.spines["top"].set_edgecolor("olive")
#ax9.spines["top"].set_linestyle("dotted")
#ax9.set_xticks([2000, 3000, 4000])

# Common functions for setting up the plot can be extracted into
# a for loop. This saves repeating code.
for ax in [ax1, ax2, ax3, ax4, ax5, ax6, ax7, ax8, ax9]:
    ax.set_ylim(1660, 1213)
    ax.grid(which='major', color='lightgrey', linestyle='-')
    ax.xaxis.set_ticks_position("top")
    ax.xaxis.set_label_position("top")
    #ax.spines["top"].set_position(("axes", 1.02))
    #ax.set_yticks([1216,1236,1256,1276,1296,1316,1336,1356])

       # loop through the formations dictionary and zone colours
    for depth, colour in zip(formations_dict.values(), zone_colours):
        # use the depths and colours to shade across the subplots
        ax.axhspan(depth[0], depth[1], color=colour, alpha=0.1)

for ax in [ax2, ax3, ax4, ax5, ax6, ax7, ax8, ax9]:
    plt.setp(ax.get_yticklabels(), visible = False)
```

```

for label, formation_mid in zip(formations_dict.keys(),
                                formation_midpoints):
        ax8.text(0.5, formation_mid, label, rotation=0,
                verticalalignment='center', horizontalalignment='right', fontweight
    ='bold',
                fontsize='small')

plt.tight_layout()
fig.subplots_adjust(wspace = 0.15)

plt.show()
```

E.2 Cross-plotting

The script in E.2 generates the cross plotting figures. McDonald (2021a) is used.

```

import matplotlib.pyplot as plt
import lasio
import numpy as np

las = lasio.read("32 4-1")
df = las.df()
df.describe()
well_nan = df.notnull() * 1
df['Vsonic1'] = df['HAC']/0.3048
df['Vsonic2'] = 1e6/df['Vsonic1'] #(unit: m/s)
df['AI'] = df['Vsonic2']*df['DEN'] #(unit:(m/s*g/cc))
df['PHID'] = (2.65-df['DEN'])/(2.65-1.07)
df_target_34=df.loc[1238:1305].reset_index() #targetting Sognefjord Fm.
phit_32_4=df_target_34.PHID
ai_32_4=df_target_34.AI
plt.style.use('bmh')
plt.scatter(ai_32_4,phit_32_4,color='#1f77b4', alpha=0.4, label='well 32/4-1')
line = np.linspace(5000,14000)
plt.xlabel('Acoustic Impedance (kg/(s*m^2))', fontsize=12)
plt.ylabel('Total porosity', fontsize=12)
plt.title('Well 32/4-1 - Sognefjord Fm, P-impedance vs. PhiT', fontsize=14)

las = lasio.read("32 2-1")
df = las.df()
df.describe()
np.any(np.isnan(df))
np.all(np.isfinite(df))
df.replace([np.inf, -np.inf], np.nan, inplace=True)
df['Vsonic1'] = df['DT']/0.3048
df['Vsonic2'] = 1e6/df['Vsonic1'] #(unit: m/s)
df['AI_32'] = df['Vsonic2']*df['RHOB'] #(unit: kg/)m2*s))
df['PHID2'] = (2.65-df['RHOB'])/(2.65-1.07)
df['PHI_avg2'] = (df['NEU']+df['PHID2'])/2
df_target2=df.loc[902:1012].reset_index() #targetting Sognefjord Fm.
phit_32_2 = df_target2.PHI_avg2
```

```
ai_32_2 = df_target2.AI_32
plt.style.use('bmh')
plt.scatter(ai_32_2,phit_32_2,color='#17becf', alpha=0.4, label='well 32/2-1')
plt.xlabel('Acoustic Impedance (kg/(s*m^2))', fontsize=12)
plt.ylabel('Total porosity', fontsize=12)
plt.title('Well 32/2-1 - Sognefjord Fm', fontsize=14)

las = lasio.read("31_6_6_composite.las")
df = las.df()
df.describe()
df['Vsonic1'] = df['HAC']/0.3048
df['Vsonic2'] = 1e6/df['Vsonic1'] #(unit: m/s)
df['AI2'] = df['Vsonic2']*df['HDEN']
df['PHID3'] = (2.65-df['HDEN'])/(2.65-1.07)
df['PHI_avg3'] = (df['HCNC']+df['PHID3'])/2
df_target=df.loc[1561:1706].reset_index() #targetting Sognefjord Fm. 9m first are
    gas filled.
a3=df_target.PHI_avg3
b3=df_target.AI2
plt.scatter(b3,a3,color='#ff7f0e', alpha=0.4, label='well 31/6-6')


las = lasio.read("31_6_3_composite.las")
df = las.df()
df.describe()
df['Vsonic1'] = df['HAC']/0.3048
df['Vsonic2'] = 1e6/df['Vsonic1'] #(unit: m/s)
df['AI2'] = df['Vsonic2']*df['HDEN']
df['PHID4'] = (2.65-df['HDEN'])/(2.65-1.07)
df['PHI_avg4'] = (df['HCN']+df['PHID4'])/2
df_target=df.loc[1511:1669].reset_index() #targetting Sognefjord Fm.
y=df_target.PHI_avg4
x=df_target.AI2
plt.scatter(x,y,color='#2ca02c', alpha=0.4, label='well 31/6-3')
plt.ylabel('Total porosity (fraction)', fontsize=12)
plt.xlabel('P-impedance ((m/s)*(g/cc))', fontsize=12)
plt.title('Sognefjord Fm. - P-impedance vs. total porosity', fontsize=14)

x = np.arange(5000,16000)
y = 0.61974-6.44357*pow(10,-5)*x+1.94626*pow(10,-9)*pow(x,2)
y_plus = 0.61974+0.0287627-6.44357*pow(10,-5)*x+1.94626*pow(10,-9)*pow(x,2)
y_minus = 0.61974-0.0287627-6.44357*pow(10,-5)*x+1.94626*pow(10,-9)*pow(x,2)
y2 = 0.889073-0.000114801*x+3.81262*pow(10,-9)*pow(x,2)
y_plus2 = 0.889073+0.0363687-0.000114801*x+3.81262*pow(10,-9)*pow(x,2)
y_minus2 = 0.889073-0.0363687-0.000114801*x+3.81262*pow(10,-9)*pow(x,2)

plt.plot(x,y,color='black',label='Best fit, Corr. = 0.8',linewidth=1)
plt.plot(x,y_plus,'--', color='red',label='Error lines',linewidth=0.7)
plt.plot(x,y_minus,'--',color='red',linewidth=0.7)
plt.ylim(0, 0.4)

# Sets up the legend
plt.legend()

```

```
# Creates the figure
plt.show()
```

Gjermund Blauenfeldt Næss

Seismically guided CO2 storage resource estimation

NTNU
Norwegian University of
Science and Technology